

**NON-RIGID POINT SET
REGISTRATION WITH
APPLICATION TO HUMAN
MASTICATORY MUSCLE
DEFORMATION**

YANG YANG

(M.Eng.(Hons.)), WASEDA

**A THESIS SUBMITTED
FOR THE DEGREE OF DOCTOR OF PHILOSOPHY**

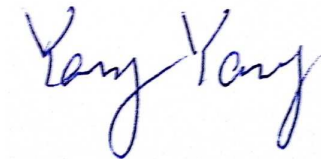
**NUS GRADUATE SCHOOL FOR INTEGRATIVE
SCIENCES AND ENGINEERING
NATIONAL UNIVERSITY OF SINGAPORE**

2013

Declaration

I hereby declare that the thesis is my original work and it has been written by me in its entirety. I have duly acknowledged all the sources of information which have been used in the thesis.

This thesis has also not been submitted for any degree in any university previously.

A handwritten signature in blue ink that reads "Yang Yang". The signature is written in a cursive style with a horizontal line under the second "Yang".

Yang Yang
09 October 2013

This Thesis is dedicated to

My Parents,

*who gave my life and taught me kindness and diligence,
for your love and sacrifices.*

My Late Grandfather,

*who supported and encouraged me,
for your love.*

My 13 Years of Life Abroad,

that taught me how to survive and left many fond and precious memories.

Acknowledgements

I would like to thank NUS Graduate School for Integrative Sciences and Engineering (NGS) for having given me the opportunity to come to work in National University of Singapore and provided the financial support during my PhD studies.

I extend warm thanks to my main-supervisor and co-supervisor, Associate Professor Kelvin Foong and Associate Professor Ong Sim Heng for their guidance and encouragement over all these years. The work presented in this thesis could not possibly be done without their inspirational ideas, valuable insights and consistent enthusiasm.

I would also like to thank Professor Takada Kenji for his continuous support and collaboration on my research. I thank Assistant Professor Yan Shui Cheng and Dr. Ng Hsiao Piau for being my PhD thesis advisory committee (TAC) members and their valuable criticism.

Finally, I would most like to thank my family who always supported and encouraged me throughout my PhD. They are the best part of my life.

Abstract

Non-rigid point set registration plays a key role in many computer vision, machine learning, medical imaging and pattern recognition applications. The goal of non-rigid point set registration is to assign correspondences between two point sets and (or) to recover the transformation that maps one point set to the other. In this thesis, we mainly focus on the development of a new non-rigid point set registration method and its applications in the studies of human masticatory system.

We first present a robust global and local mixture distance (GLMD) based non-rigid point set registration method which consists of an alternating two-step: correspondence estimation and transformation updating. We define two novel distance features for measuring global and local structural differences between two point sets, respectively. The two distances are then combined to form a GLMD based cost matrix which provides a flexible way to estimate correspondences by minimizing global or local structural differences using a linear assignment solution. To improve the correspondence estimation and enhance the interaction between the two-step, a novel annealing scheme is designed to gradually change the cost minimization from local to

global and the transformation from rigid to non-rigid during registration. We tested the performance of the proposed method in shape contour registrations and feature point matchings in sequence images and real images. We also compared the performance of the proposed method with six state-of-the-art methods where our method shows the best alignments in most scenarios.

The proposed GLMD based non-rigid point set registration method is then applied to exploring two practical problems in human masticatory system: (i) masticatory muscle functional activity investigation, and (ii) biomechanical relationship between masticatory muscle activities and mandibular movements. We proposed a new framework to assess human masticatory muscle deformation using magnetic resonance (MR) images. The framework is mainly based on the proposed non-rigid point set registration method. Through the assessment of human masticatory muscle deformation, the framework provides an effective way to assess and visualize human masticatory muscle functional activity, and explain the biomechanical relationship between masticatory muscle activities and mandibular movements.

Contents

Contents	vi
List of Figures	xii
List of Tables	xv
1 Introduction	1
1.1 Non-rigid Point Set Registration: Definition and Classification . . .	1
1.2 Review of Non-rigid Point Set Registration Methods	3
1.3 Limitations of Current Methods	5
1.4 Applications in Medical Image Registration	6
1.5 Focus of the Thesis	6
1.6 Scope of the Thesis	7
1.7 Thesis Contributions	8
2 A Robust Global and Local Mixture Distance based Non-rigid Point Set Registration Method	10
2.1 Global, Local and Mixture Distances	11
2.1.1 Global Distance	11

2.1.2	Local Distance	12
2.1.3	Mixture Distance	13
2.2	Main Process	14
2.2.1	Correspondence Estimation	14
2.2.2	Transformation Updating	15
2.2.2.1	Thin Plate Spline	16
2.2.2.2	Gaussian Radial Basis Function	18
2.2.3	A Novel Annealing Scheme	19
2.3	Our Algorithm and Parameter Setting	20
3	Experimental Results	22
3.1	Experiments on Shape Contour Registration	23
3.1.1	Performance on Four Popular Point Sets	23
3.1.2	Performance on a Wide Range of Geometrical Shapes	30
3.1.3	Performance on Partial Matching	35
3.1.4	Performance with Variable Numbers of Neighboring Points	36
3.2	Experiments on Sequence Images	40
3.3	Experiments on Real Images	41
3.4	Computational Complexity	42
3.4.1	Convergence Range	43
3.4.2	Performance of Jonker-Volgenant Algorithm	46
3.4.3	Total Computational Time	47
3.5	Registration Examples by GLMDGRBF	47
3.6	Conclusion	49

4	Related Work and Comparison	52
4.1	Related Work	52
4.2	Empirical Comparison between GLMD based Methods and Current Methods	56
4.3	TPS vs. GRBF	59
4.4	Experimental Comparison between GLMDTPS and GLMDGRBF	60
5	A New Framework for Assessing Human Masticatory Muscle Deformation	62
5.1	Human Masticatory Muscle	63
5.2	Review of Different Approaches for Studying Human Masticatory Muscle	64
5.2.1	Anatomical Study	64
5.2.2	EMG Activity Recording	65
5.2.3	Measurement of Muscle Size Change	67
5.2.4	Biomechanical Modeling	68
5.3	Limitations of Current Studies	69
5.4	A New Focus: Muscle Deformation	70
5.5	A New Framework	72
5.5.1	Muscle Deformation Capture	72
5.5.2	Muscle Model Quantization	75
5.5.3	Muscle Deformation Assessment	78
5.5.4	Muscle Deformation Visualization	79
6	Application I: Masticatory Muscle Functional Activity Investigation	81

6.1	Masseter Muscle	82
6.1.1	Research Background	82
6.1.2	3D Reconstruction of Masseter Muscle	83
6.1.3	Validation of Registration Results	84
6.1.4	Muscle Deformation Fields	86
6.1.5	Discussion and Conclusion	88
6.1.5.1	Muscle Architecture	88
6.1.5.2	Muscle Function	91
6.2	Lateral Pterygoid Muscle	94
6.2.1	Research Background	94
6.2.2	3D Reconstruction of Lateral Pterygoid Muscle	95
6.2.3	Validation of Registration Results	96
6.2.4	Muscle Deformation Fields	97
6.2.5	Discussion and Conclusion	99
6.2.5.1	Muscle Functional Activity	99
6.2.5.2	Functional Roles in Mastication	99
6.2.5.3	Functional Roles in Temporomandibular Joint Func- tion	100
7	Application II: Biomechanical Relationship between Muscle Ac- tivities and Mandibular Movements	102
7.1	Research Background	102
7.2	Image Data Acquisition	103
7.3	Estimation of Masticatory Muscle Tensions	104
7.3.1	3D Reconstruction of Masticatory Muscles	104

7.3.2	Muscle Model Quantization	104
7.3.3	Recovering Region Correspondences	105
7.3.4	Muscle Tension Estimation	105
7.3.5	Measurement of Subject-specific Mandibular Movement . .	107
7.4	Experimental Results	107
7.4.1	3D Reconstruction of masticatory muscles	107
7.4.2	Validation of Registration Results	108
7.4.3	Relationship between Mandibular Movement and Mastica- tory Muscle Tensions	110
7.5	Discussion and Conclusion	112
8	Conclusion and Future Work	113
8.1	Conclusion	113
8.1.1	Non-rigid Point Set Registration	113
8.1.2	Applications in Human Masticatory System	114
8.2	Limitations and Future Work	115
8.2.1	Non-rigid Point Set Registration	115
8.2.2	Applications in Human Masticatory System	117
Appendix A:	Useful Tools	120
.1	GLMD Demo Package	120
.2	3D Thin Plate Spline Transformation	120
.3	Jonker-Volgenant Algorithm Matlab Code	122
.4	ITK-SNAP	122
.5	Osirix	123
.6	iso2mesh	123

References

124

List of Figures

1.1	Non-rigid point set registration problem	2
2.1	Local similarity measurement	12
3.1	TPS-RPM and CPD testing point sets	24
3.2	Deformation experiment design	24
3.3	Comparison of our results (*) against CPD (∇), TPS-RPM (\square) and GMMREG (\circ) on the four point sets	26
3.4	Registration examples on Fish1	28
3.5	Registration examples on Chinese Character	29
3.6	Registration examples on Fish2	30
3.7	Registration examples on Face3D	31
3.8	Additional point sets	32
3.9	Mean performances of the four methods on the seven point sets	32
3.10	Registration examples on the seven point sets	34
3.11	Performances with missing points	35
3.12	Matching examples in missing point experiment	36
3.13	Mean performances with respect to the different numbers of neigh- boring points	37

LIST OF FIGURES

3.14	Experimental results on Bird2	38
3.15	Matching examples in a high sampling rate experiment	39
3.16	Performances with optimized K in the noise, outlier and rotation experiments.	40
3.17	Wide baseline matching example on the CMU House	42
3.18	Matching examples on cars and motorbikes.	43
3.19	Registration performances with different iterations	44
3.20	Relationships between performances and different annealing parameter settings.	45
3.21	Comparison of GLMDGRBF (*) against CPD (∇), TPS-RPM (\square) and GMMREG (\circ) on the four point sets	48
4.1	Comparison between GLMDTPS (*) and GLMDGRBF (\star) on the four point sets	61
5.1	Human masticatory muscles [1]	63
5.2	A new framework for assessing human masticatory muscle deformation	73
5.3	Muscle deformation capture	74
5.4	The experimental comparison between the Lloyd algorithm and Algorithm 3	77
5.5	Muscle model quantization	77
5.6	Muscle deformation visualization in a maximum intercuspatation case	80
6.1	3D reconstruction of masseter muscles	84
6.2	Muscle deformation fields	87

LIST OF FIGURES

6.3	Internal architecture of masseter muscle	89
6.4	Internal architecture of masseter compartments	90
6.5	A simple palpation test	92
6.6	3D reconstruction of lateral pterygoid muscles	96
6.7	Muscle deformation fields	98
6.8	Temporomandibular joint movement	101
7.1	Measurement of subject-specific mandibular movement	107
7.2	3D reconstruction of masticatory muscles	108
7.3	Biomechanical relationship between mandibular movement and mas- ticatory muscle activities	111

List of Tables

3.1	Scored non-rigid matching results and mean scores on the seven point sets	33
3.2	Matching rates on the CMU house for all possible image pairs . .	41
3.3	Matching rates on cars and motorbikes	42
3.4	Performance of Jonker-Volgenant algorithm	46
3.5	Computational times	47
4.1	Methodological differences between our methods and the current methods	53
4.2	Applicability in different dimensional problems	56
6.1	Validation of registration results	86
6.2	Validation of the proposed method	97
7.1	Priority for force index of the jaw-closing and jaw-opening muscles	106
7.2	Number of sample points	109
7.3	Validation results under different numbers of sample points. . . .	109

Chapter 1

Introduction

In this thesis, we are mainly interested in the development of a new non-rigid point set registration method and its applications to the problems of medical image registration. Before launching into the details of our proposed method, we first describe the fundamental concepts in the domain of non-rigid point set registration, and give a comprehensive review of current non-rigid point set registration methods. We then introduce some representative applications of non-rigid point set registration in the assessment of soft tissue deformation. At the end of this chapter, we briefly discuss the main focus, scope and contributions of this thesis.

1.1 Non-rigid Point Set Registration: Definition and Classification

Non-rigid point set registration plays a key role in many computer vision, machine learning, medical imaging and pattern recognition applications, such as object

retrieval, generating cartoon animation, recovering dynamic motions of human organs and muscles, and template registration for hand-written characters.

A classic non-rigid point set registration problem is defined as: given two sets of points (the source point set and the target point set which is deformed from the former), we seek to recover the correspondence between the two point sets, or (and) build a non-rigid transformation that can best map the source point set onto the target point set. An example on 2D face registration is shown in Fig. 1.1. Moreover, the non-rigid point registration problems are often accompanied with unknown deformation, rotation and the presence of noise, outliers and missing points. Thus, a good non-rigid point set registration method needs to address all these issues while it should be able to provide a fast solution.

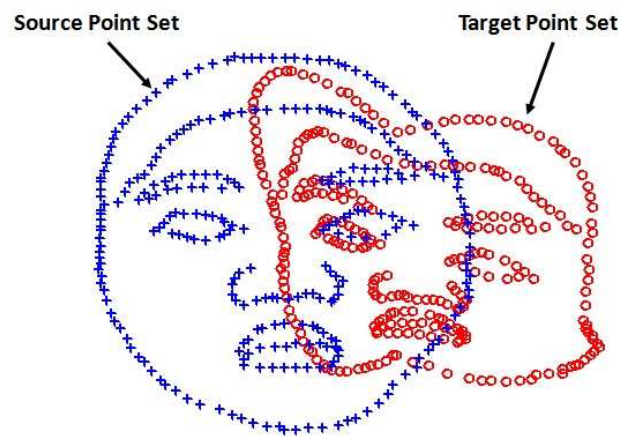


Figure 1.1: Non-rigid point set registration problem. The target point set (red) is deformed from the source point set (blue).

There are typically two unknown variables in non-rigid point set registration problems: the correspondences and the transformation. According to the methodological differences of current non-rigid point set registration methods, there are two major types of classification:

i. Iterative vs Non-iterative methods.

ii. Learning vs No learning methods.

Since we mainly focus on developing an iterative non-rigid point set registration method in this work, we introduce and discuss the current methods along the first classification (i) in the next section.

1.2 Review of Non-rigid Point Set Registration Methods

In non-iterative methods, correspondences between two point sets are recovered under a single estimation (i.e., a single iteration) using high level structures such as lines [2], curves [3], surfaces [4], shape context descriptors [5, 6] and graph relations [7, 8]. The shape context descriptors [5, 6] and graphs [7, 8] are two of the most popular features for non-iterative methods. The methods [5, 6, 9, 10, 11, 12] based on such features seek to minimize the point distribution or graph relation differences between two point sets for finding correspondences. Recently, learning graph based methods [10, 12] were introduced and the results show that parameter learning is vital for improving the registration accuracy. However, the applicabilities of point distribution and graph based methods are limited when neighboring points are close to each other [13] and have similar edge connections [14], respectively. Moreover, it is also difficult to achieve a good match under a single estimation for relatively large nonrigid distortions.

Iterative methods typically comprise an alternating two-step process: correspondence estimation and transformation updating. Compared with non-iterative

methods, the key idea of iterative methods is to gradually adjust the initial geometrical structure and location of the source point set so that it becomes more similar to the target point set, and then correspondence estimation becomes easier. The iterative closest point (ICP) method is the most famous and simplest method in this class. It was first proposed by [15] for solving a rigid point set matching problem, and then modified by [16] for the non-rigid problems. The ICP is guaranteed to converge to a local minimum. However, it does not guarantee one-to-one correspondences and its performance is very sensitive to outliers. The TPS-RPM method [16] is one of the most notable methods in this area. It employs softassign [17, 18] and deterministic annealing [19, 20] to estimate correspondences and control thin plate spline (TPS) [21] transformation updating, respectively. Recently Myronenko et al. [22] introduced a coherent points drift algorithm which is a maximum likelihood estimation with a motion coherence constraint [23] for preserving the topological structure of the point sets. Later, Myronenko and Song [24] (CPD) extended the former algorithm for both rigid and non-rigid registration, and provided a fast registration using a fast Gauss transform [25] and low-rank matrix approximation [26]. More recently, Jian and Vemuri [14] (GMMREG) introduced a Gaussian mixture model approach for both rigid and non-rigid registration. They consider the registration problem as one of aligning two Gaussian mixture models, and the transformation is updated by minimizing the L2 distance [27] between the two models.

1.3 Limitations of Current Methods

The CPD and GMMREG methods are two of the best performing non-rigid point set registration methods. Both CPD and GMMREG follow the alternating two-step process as in ICP and TPS-RPM, and further improve the transformation updating using the motion coherent and L2 distance minimization constraints, respectively. However, there are three major issues in the current methods as follows:

- The CPD and GMMREG still employ a similar Gaussian probability density to assign a fuzzy correspondence which leads to a 'fuzzy location updating' for the warping template. The 'fuzzy location updating' may cause the registration process to spend relatively more iterations during registration, and may not be always valid to update the locations of the warping template. That may be a major reason why the CPD and GMMREG focus on developing the constraints for transformation updating.
- Forcing the points to move coherently in CPD may produce a relatively large error when one point is mismatched, and may also be undesirable when source points need to be moved in different directions to match their target points.
- The Euclidean distance between two point sets in GMMREG is not always minimized by minimizing the L2 distance between two Gaussian mixture models.

1.4 Applications in Medical Image Registration

Assessing soft tissue deformation is one of the most important applications in medical image registration. By using non-rigid point set registration techniques, some recent studies have successfully investigated the human and animal soft tissue deformations through recovering region correspondences between the soft tissue before and after deformation. Examples of such studies are human brain mapping [16, 28], assessing cardiac [29, 30], stomach [31] and lung deformations [32], and recognizing facial expression [33].

In these studies, the main process of assessing a soft tissue deformation is to first employ point feature representation (the point cloud) to modeling soft tissue morphologies before and after deformation, and then recover the region correspondences between the two point cloud models using non-rigid point set registration techniques. Finally, the recovered corresponding relations (the paired corresponding points) is used to represent the deformation field of the target soft tissue.

Therefore, designing an appropriate protocol to capture soft tissue deformations by medical imaging and developing (or choosing) an appropriate non-rigid point set registration method play the key roles in such studies.

1.5 Focus of the Thesis

We mainly focus on developing a new non-rigid point set registration method which can address the aforementioned three issues in the current methods, and its applications in two practical problems of studying human masticatory system.

More specifically, in this work,

1. We focus on designing novel distance features for non-rigid point set registration problems.
2. We develop a new method for non-rigid point set registration problem that addresses several problems in current methods: (a) fuzzy location updating (in the TPS-RPM, CPD and GMMREG), (b) forcing points to move coherently (in the CPD), and (c) minimizing Euclidean distance (in the GMMREG).
3. We employ the new method to explore two practical problems in the studies of human masticatory system: (a) masticatory muscle functional activity investigation, and (b) biomechanical relationship between masticatory muscle activities and mandibular movements.

1.6 Scope of the Thesis

The scope of this thesis is as follows:

1. We present a robust global and local mixture distance based non-rigid point set registration method in Chapter 2.
2. We compare the performance of our method with six state-of-the-art methods in Chapter 3.
3. We theoretically and empirically discuss the advantages and disadvantages between our method and the current methods in Chapter 4.

-
4. We present a new framework which is mainly based on the proposed non-rigid point set registration method for the assessment of human masticatory muscle deformation in Chapter 5.
 5. We demonstrate an application I: Masticatory Muscle Functional Activity Investigation in Chapter 6.
 6. We demonstrate an application II: Biomechanical Relationship between Muscle Activities and Mandibular Movements in Chapter 7.
 7. We conclude with a discussion on the limitations of our work and future work in Chapter 8.

1.7 Thesis Contributions

The significant contributions of this thesis include the following:

- We propose three novel distance features: global, local and mixture distances.
- We propose a new approach "Global feature + $\alpha \times$ Local feature" that employs multiple features for estimating correspondence in non-rigid point set registration problems.
- We develop a new non-rigid point set registration method which addresses the issues in the current methods (see Chapter 3 and 4), and outperforms state-of-the-art methods.
- We investigate the deformations of masticatory muscles during jaw opening and closing using MR images. The assessed muscle deformations are used

to explain the muscle functional roles during jaw movements (in Chapter 6).

- We explain the biomechanical relationship between the mandibular movement and the functional activities of masticatory muscles under a maximum intercuspation case by measuring the mandibular movement from MR images and assessing the deformations of masticatory muscles (in Chapter 7).

Chapter 2

A Robust Global and Local Mixture Distance based Non-rigid Point Set Registration Method

In this chapter, we present a robust global and local mixture distance (GLMD) based non-rigid point set registration method which consists of an alternating two-step: correspondence estimation and transformation updating. We first define a global distance and a local distance for measuring the global and local differences between two point sets, respectively. The two distances are then combined to form a GLMD based cost matrix which provides a flexible way to estimate correspondence between two point sets by minimizing the local or global difference using a linear assignment solution. To improve the correspondence estimation using both local and global features and enhance the interaction between the two

steps, a novel annealing scheme is designed to gradually change the GLMD based cost matrix minimization from the local to global distance and the non-rigid spatial transformation from a more rigid to a more non-rigid during registration. Since the proposed method may easily combine the correspondence estimation with different transformations such as TPS transformation and Gaussian radial basis function (GRBF), we describe two combinations: GLMD based correspondence estimation + TPS transformation (called "GLMDTPS") and GLMD based correspondence estimation + GRBF transformation (called "GLMDGRBF") in this chapter.

2.1 Global, Local and Mixture Distances

2.1.1 Global Distance

Global distance is used to measure squared Euclidean distances from one point set to another, and defined as

$$\mathbf{G}_{a_i b_i} = G(\mathbf{a}_i, \mathbf{b}_j) = \|\mathbf{a}_i - \mathbf{b}_j\|^2 \quad (2.1)$$

where \mathbf{G}_{ab} matrix describes the global structural difference between point set \mathbf{a} and point set \mathbf{b} . If we consider \mathbf{G}_{ab} as a global cost matrix and minimize it by a linear assignment solution, we will obtain the corresponding relation between \mathbf{a} and \mathbf{b} , which is based on the minimization of global structural difference between the two point sets.

2.1.2 Local Distance

Local distance is designed to measure local differences (or similarities) from one point sets to another. The basic idea is shown in Fig. 2.1. For example, in

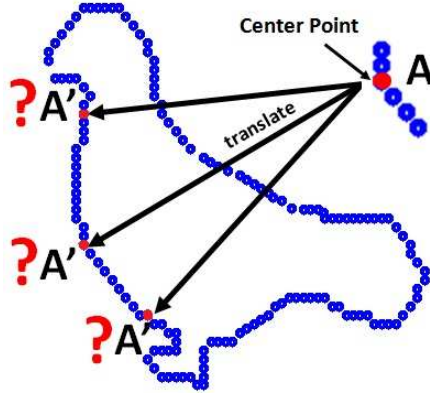


Figure 2.1: Local similarity measurement. Each red point and its closest points (the five blue points) construct a small segment in the point set, such as A and A' shown here.

order to find a corresponding segment A' for A , we first translate the five closest points of the center point (the red point in Fig. 2.1) in A to each A' according to a displacement vector from the center point in A to the center point in A' . Then, we sum the distances between the two sets of closest points. Finally, the corresponding segment of A is determined by a segment having the shortest summed distance. The local distance is formulated as

$$\mathbf{L}_{a_i b_j} = L(\mathbf{a}_i, \mathbf{b}_j) = \sum_{k=1}^K \| T(\mathbf{N}(\mathbf{a}_i)_k, \mathbf{b}_j) - \mathbf{N}(\mathbf{b}_j)_k \|^2 \quad (2.2)$$

where \mathbf{L}_{ab} is a local distance matrix from point set \mathbf{a} to point set \mathbf{b} , and K is the number of neighboring points. $\mathbf{N}(\mathbf{a}_i)_k$ and $\mathbf{N}(\mathbf{b}_j)_k$ are the k^{th} closest point

for the points \mathbf{a}_i and \mathbf{b}_j , respectively. T is the translation function defined by

$$T(\mathbf{N}(\mathbf{a}_i)_k, \mathbf{b}_j) = \mathbf{N}(\mathbf{a}_i)_k + (\mathbf{b}_j - \mathbf{a}_i) \quad (2.3)$$

The local distance $L(\mathbf{a}_i, \mathbf{b}_j)$ is mainly determined by the number of neighboring points K which plays an important role in measuring local similarity, preserving the topological structure of the point sets as well as dealing with noise, outliers, rotation and missing points. Here, if we consider \mathbf{L}_{ab} as a local cost matrix and minimize it by a linear assignment technique, we will obtain the corresponding relation between \mathbf{a} and \mathbf{b} , which is based on the minimization of local structural differences between the two point sets.

2.1.3 Mixture Distance

The mixture distance consists of the global and local cost matrices (i.e., the global and local distance matrices). It is defined as

$$\mathbf{C}_{ab} = \mathbf{G}_{ab} + \alpha \cdot \mathbf{L}_{ab} \quad (2.4)$$

where \mathbf{C}_{ab} is a GLMD based cost matrix. α is a weighting parameter that controls the balance between the global and local costs in \mathbf{C}_{ab} . For example, when α is very large, minimizing \mathbf{C}_{ab} is equal to minimizing the local distance cost \mathbf{L}_{ab} . The process tends to minimize the global distance cost \mathbf{G}_{ab} when α becomes small. The designed mixture distance \mathbf{C}_{ab} provides a flexible way to estimate the correspondence by minimizing the local or global structural difference between two point sets.

2.2 Main Process

Suppose we have two point sets $\{\mathbf{x}_i, i = 1, 2, \dots, X\}$ and $\{\mathbf{y}_j, j = 1, 2, \dots, Y\}$ in R^2 or in R^3 for the source point set \mathbf{x} and the target point set \mathbf{y} , respectively. The process of this method is first (i) to use a warping template \mathbf{x}^w (the initial $\mathbf{x}^w = \mathbf{x}$) to estimate corresponding points \mathbf{y}^c (the points in \mathbf{y}) for \mathbf{x} at each iteration, and then (ii) to update the locations of \mathbf{x}^w using the recovered correspondence between \mathbf{x} and \mathbf{y}^c . The steps (i) and (ii) are iterated such that the warping template \mathbf{x}^w can gradually and continuously approach the target point set \mathbf{y} , and finally match the exact corresponding points in \mathbf{y} .

2.2.1 Correspondence Estimation

The list of corresponding points \mathbf{y}^c at each iteration is estimated by minimizing the total cost function

$$C_{\text{total}}(\mathbf{M}) = \sum_i^X \sum_j^Y \mathbf{M}_{ij} \mathbf{C}_{x^w y_j} \quad (2.5)$$

where the solution \mathbf{M} is a binary correspondence matrix (from \mathbf{x}^w to \mathbf{y}) and still satisfies $\sum_j^Y \mathbf{M}_{ij} = 1$ for $i \in 1, \dots, X$ with $\mathbf{M}_{ij} \in \{0, 1\}$. $\mathbf{C}_{x^w y}$ is the GLMD based cost matrix (described in Section 2.1.3) from \mathbf{x}^w to \mathbf{y} . $\mathbf{C}_{x^w y}$ contains the weighting parameter α that is controlled by an annealing scheme for changing the minimization from the local distance to the global distance. For each point \mathbf{x}_i^w and \mathbf{y}_j , the sets of neighboring points $\mathbf{N}(\mathbf{x}_i^w)$ and $\mathbf{N}(\mathbf{y}_j)$ used in the local distance $\mathbf{L}_{x^w y}$ are determined by the Euclidean distance relationships in the source point set \mathbf{x} and the target point set \mathbf{y} , respectively. Since a local distance $L(\mathbf{x}_i^w, \mathbf{y}_j)$

is measured from two small segments and the determined neighboring relations $\mathbf{N}(\mathbf{x}_i^w)$ and $\mathbf{N}(\mathbf{y}_i)$ are fixed during the warpings of \mathbf{x}^w , minimizing the local distance preserves the topological structures of the point set \mathbf{x}^w .

To find the correspondence matrix \mathbf{M} where the total cost $\mathbf{C}_{\text{total}}$ has the minimum value, we solve the total cost function as a linear assignment problem using the Jonker-Volgenant Algorithm [34] which provides the shortest augmenting path and has worst-cost time $O(N^3)$. The original Jonker-Volgenant algorithm was developed for integer cost and only works on the square cost. To overcome the two limitations, the calculated GLMD based cost $\mathbf{C}_{x^w y}$ is rounded by $\lfloor \mathbf{C}_{x^w y} \times R \rfloor$ where R is a large resolution and set to 10^6 (since we rescale the coordinates of all points within (0,1) before registration) in this work. If the size of point set \mathbf{x} is less than point set \mathbf{y} (\mathbf{y} includes outliers or \mathbf{x} misses points), the non-square cost $\mathbf{C}_{x^w y}$ will be converted into a square cost problem by assigning dummy entries [35] that do not affect the total cost. $\mathbf{C}_{x^w y}$ can then be solved in the usual way and still give the best solution. The solved \mathbf{M} guarantees one-to-one correspondence (from \mathbf{x}^w to \mathbf{y}). The new correspondence \mathbf{y}^c for the \mathbf{x} is then updated by

$$\mathbf{y}^c = \mathbf{M} \cdot \mathbf{y} \tag{2.6}$$

2.2.2 Transformation Updating

Since the aforementioned correspondence estimation can easily combine with different non-rigid transformations, we present the two implementations of using TPS and GRBF, respectively, in this section.

2.2.2.1 Thin Plate Spline

After updated \mathbf{y}^c , the spatial transformation is refined by the current correspondence \mathbf{y}^c and the source point set \mathbf{x} . In this work, we map \mathbf{x} to \mathbf{y}^c by TPS transformation

$$f(\mathbf{x}, \mathbf{d}, \mathbf{w}) = \mathbf{x} \cdot \mathbf{d} + \phi(\mathbf{x}) \cdot \mathbf{w} \quad (2.7)$$

where \mathbf{d} is a affine coefficient matrix and \mathbf{w} is a non-rigid warping coefficient matrix. $\phi(\mathbf{x})$ is the TPS kernel function defined by $\phi(\mathbf{x}) = \|\mathbf{x} - \mathbf{x}_c\|^2 \log \|\mathbf{x} - \mathbf{x}_c\|$ and $\phi(\mathbf{x}) = \|\mathbf{x} - \mathbf{x}_c\|$ for the 2D and 3D cases, respectively. \mathbf{x}_c is a set of control points chosen from \mathbf{x} .

To map \mathbf{x} to its correspondence \mathbf{y}^c with the proper \mathbf{d} and \mathbf{w} , the minimizing TPS energy is defined as

$$E_{\text{TPS}}(f) = \sum_{i=1}^X \|\mathbf{y}^c - f(\mathbf{x})\|^2 + \lambda \int \int [(\frac{\partial^2 f}{\partial x^2})^2 + 2(\frac{\partial^2 f}{\partial x \partial y})^2 + (\frac{\partial^2 f}{\partial y^2})^2] dx dy \quad (2.8)$$

By substituting the solution for (2.7) into (2.8), the TPS energy function becomes

$$E_{\text{TPS}}(\mathbf{d}, \mathbf{w}) = \|\mathbf{y}^c - \mathbf{x}\mathbf{d} - \mathbf{\Phi}\mathbf{w}\|^2 + \lambda \text{trace}(\mathbf{w}^T \mathbf{\Phi}\mathbf{w}) \quad (2.9)$$

where the regularization parameter λ penalizes the non-rigid warping coefficient \mathbf{w} , and is controlled by the same annealing scheme used to the aforementioned weighting parameter α in (2.4). $\mathbf{\Phi}$ is the kernel matrix from the kernel function $\phi(\mathbf{x})$.

To find the least-squares solutions for the \mathbf{d} and \mathbf{w} , the *QR* decomposition

[36] is used to separate the affine and non-rigid warping space by

$$\mathbf{x} = QR = [\mathbf{Q}_1 | \mathbf{Q}_2] \begin{pmatrix} \mathbf{R}_1 \\ 0 \end{pmatrix} \quad (2.10)$$

where \mathbf{Q}_1 is an $N \times D$ matrix, \mathbf{Q}_2 is $N \times (N - D)$, \mathbf{R}_1 is $D \times D$, and \mathbf{Q}_1 and \mathbf{Q}_2 both have orthogonal columns. Thus (2.9) becomes

$$E_{\text{TPS}}(\boldsymbol{\gamma}, \mathbf{d}) = \|\mathbf{Q}_2^T \mathbf{y}^c - \mathbf{Q}_2^T \boldsymbol{\Phi} \mathbf{Q}_2 \boldsymbol{\gamma}\|^2 + \|\mathbf{Q}_1^T \mathbf{y}^c - \mathbf{R}_1 \mathbf{d} - \mathbf{Q}_1^T \boldsymbol{\Phi} \mathbf{Q}_2 \boldsymbol{\gamma}\|^2 + \lambda \boldsymbol{\gamma}^T \mathbf{Q}_2^T \boldsymbol{\Phi} \mathbf{Q}_2 \boldsymbol{\gamma} \quad (2.11)$$

where $\mathbf{w} = \mathbf{Q}_2 \boldsymbol{\gamma}$ and $\boldsymbol{\gamma}$ is $(N - D - 1) \times (D + 1)$. The least-squares solution for (2.11) can be first minimized with respect to $\boldsymbol{\gamma}$ and then with respect to \mathbf{d} . The final solutions for \mathbf{w} and \mathbf{d} are

$$\hat{\mathbf{w}} = \mathbf{Q}_2 \boldsymbol{\gamma} = \mathbf{Q}_2 (\mathbf{Q}_2^T \boldsymbol{\Phi} \mathbf{Q}_2 + \lambda \mathbf{I}_{N-D-1})^{-1} \mathbf{Q}_2^T \mathbf{y}^c \quad (2.12)$$

$$\hat{\mathbf{d}} = \mathbf{R}^{-1} (\mathbf{Q}_1^T \mathbf{y}^c - \boldsymbol{\Phi} \mathbf{w}) \quad (2.13)$$

The new location of the warping template \mathbf{x}^w is updated by

$$\mathbf{x}^w = \mathbf{x} \cdot \mathbf{d} + \boldsymbol{\Phi} \cdot \mathbf{w} \quad (2.14)$$

2.2.2.2 Gaussian Radial Basis Function

We can also map \mathbf{x} to \mathbf{y}^c by GRBF transformation

$$f_{\text{GRBF}}(\mathbf{x}) = \sum_{i=1}^X \mathbf{w}_i \phi(\|\mathbf{x} - \mathbf{c}_i\|) \quad (2.15)$$

The Gaussian kernel function is defined by $\phi(\mathbf{r}) = \exp(-\mathbf{r}^2/\sigma^2)$ and $\phi(\mathbf{r}) = \mathbf{r}$ for the 2D and 3D case, respectively. \mathbf{w} is the warping coefficient matrix. To map \mathbf{x} to its correspondence \mathbf{y}^c with the proper \mathbf{w} , the minimizing GRBF energy is defined as

$$E_{\text{GRBF}}(\mathbf{w}) = \|\mathbf{y}^c - \mathbf{\Phi}\mathbf{w}\|^2 + \lambda \cdot \text{trace}(\mathbf{w}^T \mathbf{\Phi}\mathbf{w}) \quad (2.16)$$

where the regularization parameter λ controlled by the same annealing scheme penalizes the warping coefficient \mathbf{w} , and $\mathbf{\Phi}$ is the kernel matrix from the kernel function $\phi(\mathbf{r})$. The warping coefficient \mathbf{w} is computed by

$$\hat{\mathbf{w}} = (\mathbf{\Phi}^T \mathbf{\Phi} + \lambda \mathbf{\Phi})^{-1} \mathbf{\Phi}^T \mathbf{y}^c \quad (2.17)$$

This new location of \mathbf{x}^w is then updated by

$$\mathbf{x}^w = \mathbf{\Phi} \cdot \mathbf{w} \quad (2.18)$$

After updated the location of \mathbf{x}^w , we return to the first step (2.2.1) for continuing the registration process until the final temperature T_{final} of the annealing scheme is reached.

2.2.3 A Novel Annealing Scheme

Deterministic annealing [19] [20] is a useful heuristic for avoiding local minima for a variety of optimization problems. A annealing scheme starts with a high temperature T_{init} , and ends at a specified T_{final} . The main reasons of using a annealing scheme in this work are: (i) to reduce the weighting parameter α in (2.4) to change the cost minimization from local to global, and (ii) to reduce the regularization parameter λ (in 2.12 for TPS or 2.17 for GRBF transformation) to adjust the spatial transformation from a more rigid to a more non-rigid.

For example, at the start of registration, a large initial α causes the correspondence matrix to focus on searching local similarities between \mathbf{x}^w and \mathbf{y} . Minimizing the local distance preserves the topological structure of the warping template \mathbf{x}^w and deals with noise, outliers, rotation and missing points. It also improves the correspondence estimation, while the improved recovered correspondence makes the spatial transformation better behaved. Furthermore, with a large λ , the transformation performs a more rigid and also preserves the topological structure of \mathbf{x}^w , prevents mismatches and rejects noise and outliers. As the temperature T decreases, α and λ become small. The registration process tends to minimize the global distance between \mathbf{x}^w and \mathbf{y} , while the transformation performs a more non-rigid to make \mathbf{x}^w approach \mathbf{y} as close as possible.

To summarize, the annealing scheme improves the flexibility and accuracy of the correspondence estimation using both local and global distance features and also enhances the interaction between the correspondence estimation and transformation updating during the registration.

2.3 Our Algorithm and Parameter Setting

The pseudo codes of GLMDTPS and GLMDGRBF are shown in Algorithm 1 and 2, respectively.

Algorithm 1 GLMDTPS

Input: Point sets \mathbf{x} and \mathbf{y}

To initialize parameters T_{init} , T_{final} , r , λ_{init} and α_{init}

To set K and determine $\mathbf{N}(x_i^w)_k$ and $\mathbf{N}(y_j)_k$ for \mathbf{x}^w and \mathbf{y}

Begin I: Annealing scheme

Step1: Estimating the current correspondences \mathbf{y}^c by (2.5) and (2.6).

Step2: Updating the TPS transformation by (2.12) and (2.13).

Update the location of \mathbf{x}^w by (2.14).

Update the parameter α and λ by decreasing T .

End I: Until $T \leq T_{final}$ is reached.

Output: Warped source point set \mathbf{x}^w

Algorithm 2 GLMDGRBF

Input: Point sets \mathbf{x} and \mathbf{y}

To initialize parameters T_{init} , T_{final} , r , λ_{init} α_{init}

To set K and determined $\mathbf{N}(x_i^w)_k$ and $\mathbf{N}(y_j)_k$ for \mathbf{x}^w and \mathbf{y}

Begin I: Annealing scheme

Step1: Estimating the current correspondences \mathbf{y}^c by (2.5) and (2.6).

Step2: Updating the GRBF transformation by (2.17).

Update the location of \mathbf{x}^w by (2.18).

Update the parameter α and λ by decreasing T .

End I: Until $T \leq T_{final}$ is reached.

Output: Warped source point set \mathbf{x}^w

At first, the annealing parameter T is set to start with high temperature T_{init} , and end with a low temperature T_{final} , where T is gradually reduced by a linear annealing schedule $T = T \cdot r$ where r is the annealing rate. Meanwhile the parameter α and λ are also reduced by $\alpha = \alpha_{init} \cdot T$ and $\lambda = \lambda_{init} \cdot T$, respectively. There are four groups of free parameters in GLMDTPS and GLMDGRBF: the annealing parameters T_{init} , T_{final} and r , the weighting parameter α , the regular-

ization parameter λ , and the number of closest points K . Both GLMDTPS and GLMDGRBF have the same parameter setting as follows

- **Annealing parameters:** T_{init} , T_{final} and r are set to ensure there are sufficient iterations for the registration process. Based on an initial trial-and-error experiment using a Fish1 point set (see Section 3.1.1), T_{init} is set to 1/10 of the largest squared distance between x and y , T_{final} is chosen to be equal to 1/8 of the mean squared distance between the neighboring points in x , and r is usually set to 0.7.
- **Weighting parameter:** The value of α_{init} is large to make the correspondence estimation focus on minimizing local differences at the start of registration. The initial value of α_{init} is set to the squared number of the neighboring points K^2 .
- **Regularization parameter:** The value of λ_{init} is large to make the TPS focus on performing more rigid transformations at the start of registration. The initial value of λ_{init} is set to the length of point set x .
- **The number of neighboring points:** The value of K is based on the minimum number of points used for distinguishing local structures. For example, to distinguish between a corner (includes two neighboring points) and a cross (includes four neighboring points), at least four neighboring points are required. K is set to 5 for both 2D and 3D as default. It can also be optimized for a particular case since adjusting the number of neighboring points can better distinguish local structures for improving the correspondence estimation and dealing with noise, outliers and rotation (see Section 3.1.4).

Chapter 3

Experimental Results

We implemented the main process of our method (both GLMDTPS and GLMD-GRBF) in Matlab, and the Jonker-Volgenant algorithm in C++ as a Matlab mex function. Since TPS and GRBF transformations give very similar performances in 2D and 3D cases, we selected GLMDTPS as our representative to mainly test the performance of the proposed method in the following three series of experiments,

- Shape contour registration
- Feature point matching in sequence images
- Feature point matching in real images

while we compared the performance of GLMDTPS against the following three types of state-of-the-art methods:

- Iterative methods: TPS-RPM [16], CPD [24] and GMMREG [14].
- No learning graph based methods: FGM [11].

-
- Learning graph based methods: Caetano et al. [10] and Leordeanu et al. [12].

In addition, we also evaluated the computational complexity of our method, and discussed how the computational cost can be reduced. At the end of this chapter, some registration examples by GLMDGRBF and the conclusion are given.

3.1 Experiments on Shape Contour Registration

In the first series of experiments, we evaluate the performances of our method on different shape contour registration problems. Compared with the labeled feature point sets in sequence images and real images (such as CMU sequence and Pascal 2007 challenge in section 3.2 and 3.3), shape contour point sets are typically sampled by a relatively high sampling rate and the registration is more difficult on distinguishing local similarities since contour points are very close to each other and have similar local features.

3.1.1 Performance on Four Popular Point Sets

There is no standard shape contour database that has been commonly used for experimental comparison by the current non-rigid point set registration methods. We first select the four most popular point sets from the TPS-RPM and CPD works (as shown in Fig. 3.1).

Experiment design: To generate series of "moderate" and "rich" target point sets from the selected point sets, we design the experiments as follows

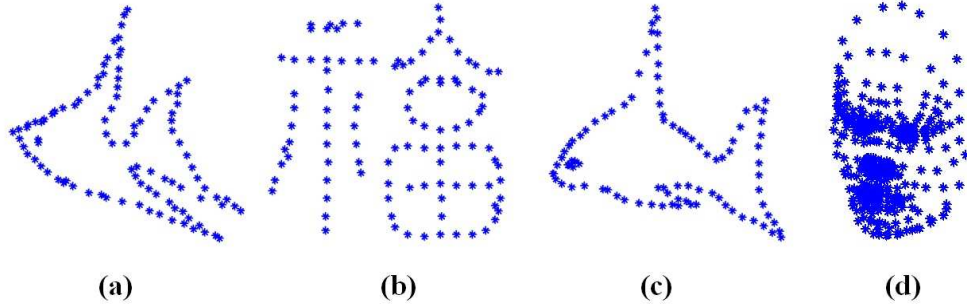


Figure 3.1: TPS-RPM and CPD testing point sets: (a) Fish1 (98 points), (b) Chinese Character (105 points), (c) Fish2 (91 points) and (d) Face3D (392 points). (a) and (b) are obtained from Chui and Rangarajan [16]. (c) and (d) are obtained from Myronenko and Song [24]

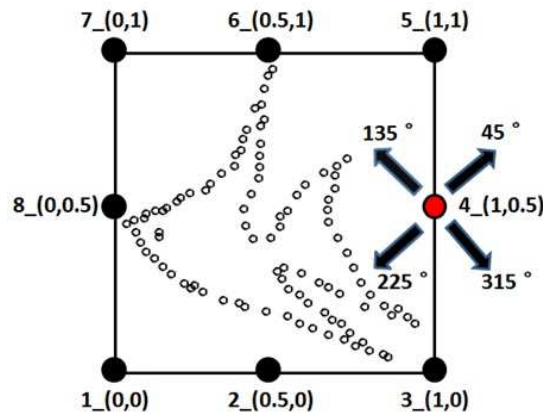


Figure 3.2: Deformation experiment design

- (a) Deformation: eight control points on the boundary of each source point set (six control points on the left, right, anterior, posterior, superior and inferior of the boundary for 3D) are set as shown in Fig. 3.2. Each control point is set with four free moving directions (nine directions for 3D) and 0.2 moving distance. The order and the moving directions of control points are randomly determined. TPS transformation is employed to warp source point sets using the defined control points, and the order of the warped source points is then randomly rearranged. The degree of deformation is defined as the number of

moved control points since the higher level of point perturbations produces the higher deformation.

- (b) Noise: five noise levels are used and defined as Gaussian white noise with a zero mean and standard deviation from 0.01 to 0.05.
- (c) Outlier: five outlier to data ratios are used and defined as the number of outliers to the original data ratios ranging from 0.2 to 1.
- (d) Rotation: we focus on the rotation range from -30° to 30° with a 15° interval (the target point sets in 3D case are rotated on the vertical axis) since beyond this range some methods will show an unstable performance. Although the other three methods have not been evaluated in non-rigid rotation experiments, we consider that evaluating performance under moderate rotations is essential since the deformation is often accompanied by a rotation.

For (b) (c) and (d), each source point set are also randomly warped by a medium degree of deformation (the fourth degree for 2D and the third degree for 3D) before being added noise, outliers or rotations.

Performance assessment: To assess the registration performance, we followed the same error measurement and the overall performance assessment in TPS-RPM [16] and CPD [24]: the mean squared distance between the recovered corresponding points and the exact corresponding points, and the mean error. For each point set, one hundred random experiments are repeated for each setting (i.e., each degree of deformation, noise level, outlier ratio and rotation degree) in each experiment.

Comparison results: In order to achieve a direct and fair comparison with the other three methods, we only compared the performance of our method

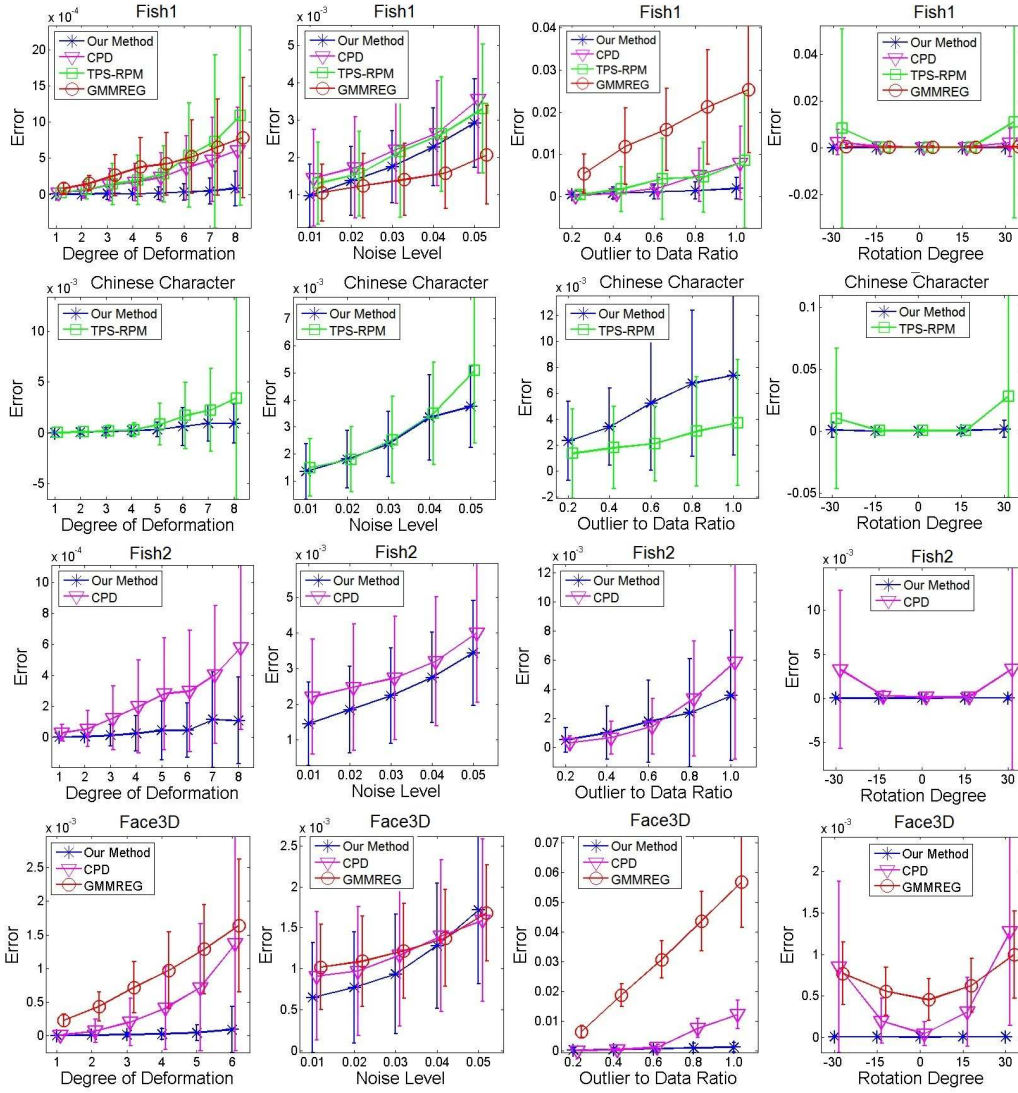


Figure 3.3: Comparison of our results (*) against CPD (∇), TPS-RPM (\square) and GMMREG (\circ) on the four point sets. The error bars indicate the standard deviations of the mean errors in 100 random experiments. From the top row to bottom row are: Fish1, Chinese Character, Fish2 and Face3D, respectively.

against the others under their already tested point sets in this experiment since they only provided the parameter values (in the published papers [14, 16, 24] and the source codes [37, 38, 39]) for those point sets. The parameters of our method are set as described in section 2.3. The comparison results are shown in Fig. 3.3 and discussed as follows:

- **Fish1:** The performance statistics (the mean error and its standard deviation) are shown in the first row of Fig. 3.3. Our method shows accurate alignments in all experiments, and gives the best performances over all degrees of deformation, outlier to data ratios from 0.6 to 1.0, and all degrees of rotation. In the noise experiment, all the four methods give accurate alignments while the GMMREG generally performed better. Registration examples are shown in Fig. 3.4.
- **Chinese Character:** We only present the performances of our method and TPS-RPM in this experiment (the second row of Fig. 3.3) since Chinese Character has not been tested in the CPD and GMMREG papers for non-rigid point set registration (GMMREG only tested it in the rigid registration experiment). Our method shows accurate alignments and gives the best performances over all degrees of deformation, all noise levels and all degrees of rotation. In the outlier experiment, the TPS-RPM performs better. The reason of why our method performed relatively poorly is that the outliers spreading out on the Chinese Character shape can easily change the local structures compared with the other point sets such as Fish1. Registration examples are shown in Fig. 3.5.
- **Fish2:** The performances of our method and CPD are given in the third row

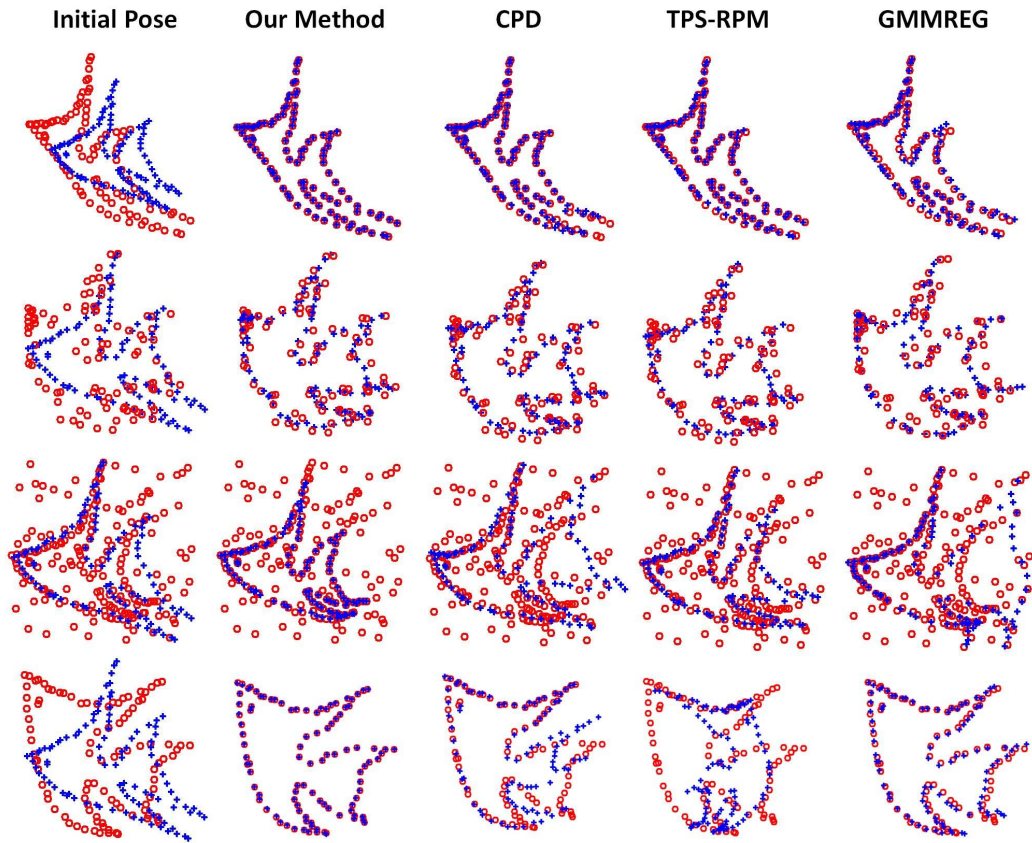


Figure 3.4: Registration examples on Fish1. From the top row to bottom row are examples in the deformation (the 8th degree), noise (0.03), outlier (1.0) and rotation (-30°) experiments

of Fig. 3.3. Our method shows accurate alignments in all experiments, and gives the best performances over all degrees of deformation, all noise levels, large outlier ratios from 0.8 to 1.0, and all degrees of rotation. Registration examples are shown in Fig. 3.6.

- **Face3D:** The performances of our method, the CPD and GMMREG are given in the fourth row of Fig. 3.3. Our method shows accurate alignments in all experiments, and gives the best performances over deformation degrees from the second to the eighth degrees, noise levels from 0.01 to 0.04, outlier

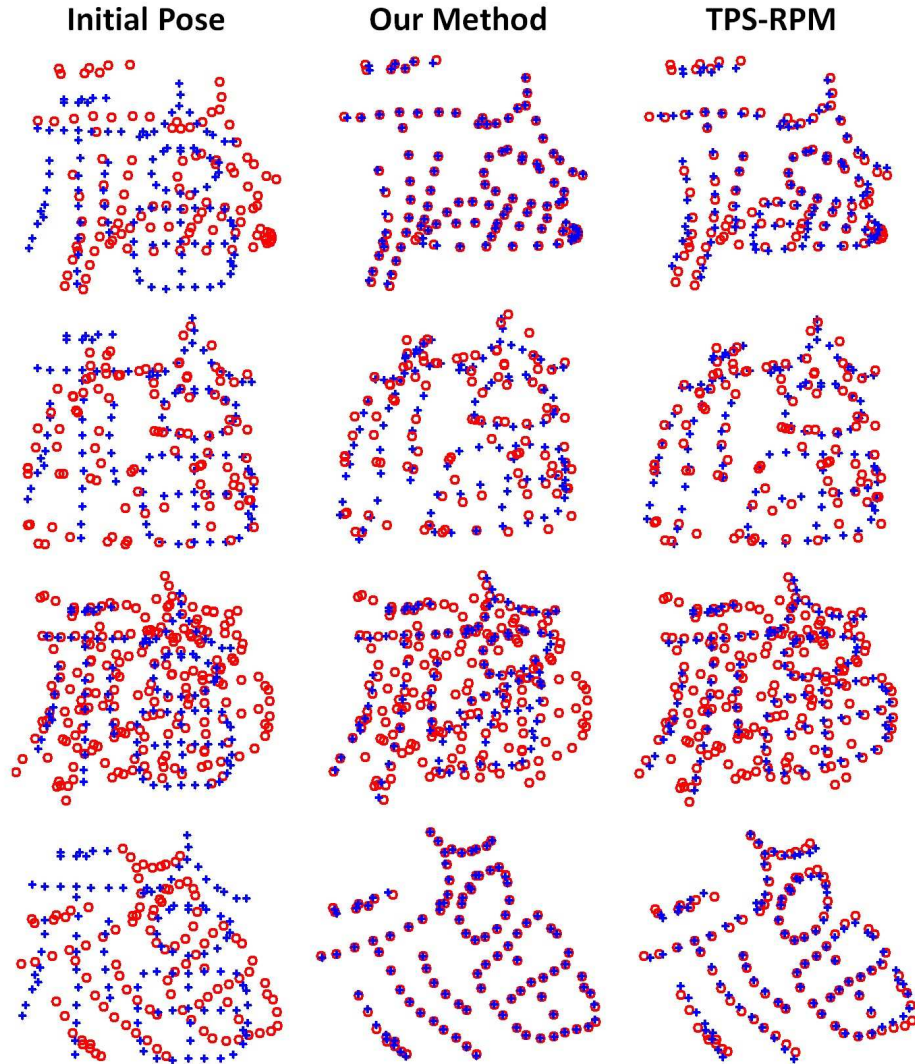


Figure 3.5: Registration examples on Chinese Character. From the top row to bottom row are examples in the deformation (the 8th degree), noise (0.03), outlier (1.0) and rotation (30°) experiments.

ratios from 0.6 to 1.0, and all degrees of rotation. Registration examples are shown in Fig. 3.7.

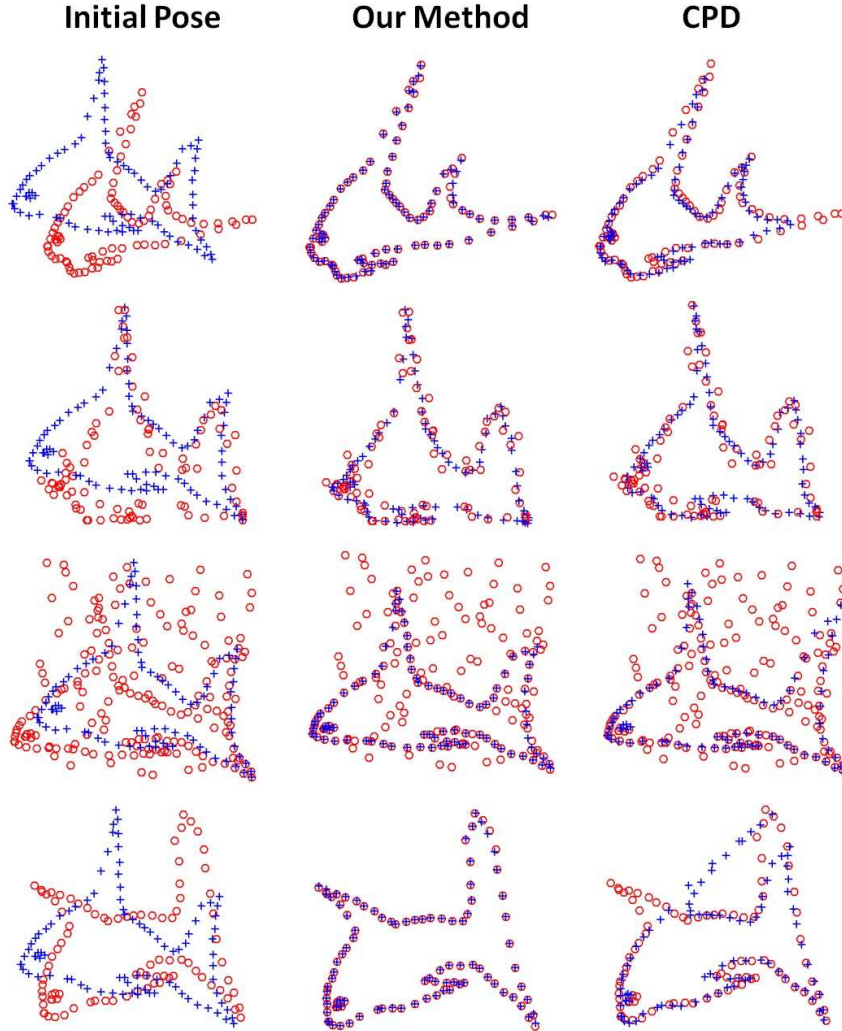


Figure 3.6: Registration examples on Fish2. From the top row to bottom row are examples in the deformation (the 6th degree), noise (0.03), outlier (1.0) and rotation (30°) experiments.

3.1.2 Performance on a Wide Range of Geometrical Shapes

In this experiment, we consider that a good non-rigid point set registration method should be robust to different geometrical shapes and not be sensitive to its parameter setting since we normally deal with a non-rigid point set registration as an unknown problem where we may not be allowed to tweak parameter

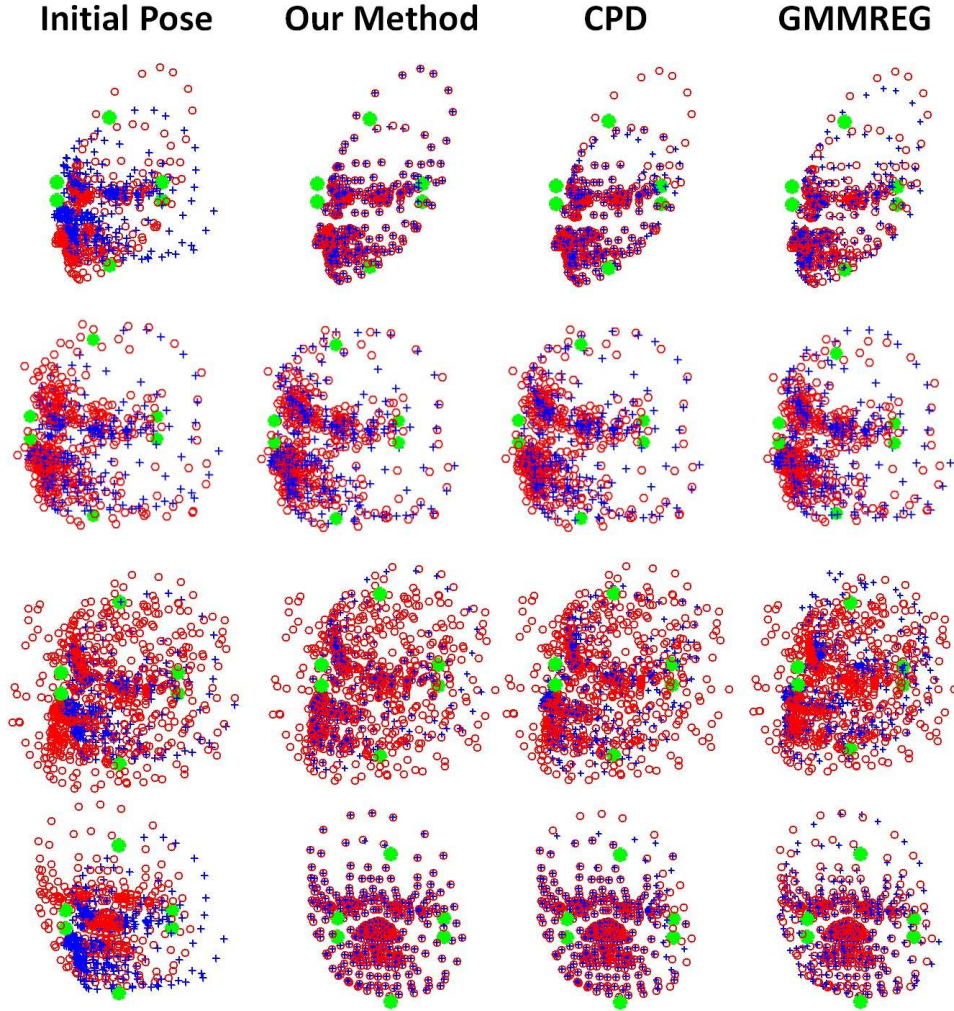


Figure 3.7: Registration examples on Face3D. From the top row to bottom row are examples in the deformation (the 4th degree), noise (0.03), outlier (0.8) and rotation (30°) experiments. The green points are the control points for generating deformations.

values for each case. Thus, we further add another five point sets (shown in Fig. 3.8), and combine them with the Fish1 and Chinese Character to evaluate the performances of the four methods. The parameter setting of each method follows the same setting in the Fish1 experiment.

The mean performances (i.e., the mean error) of the four methods on the

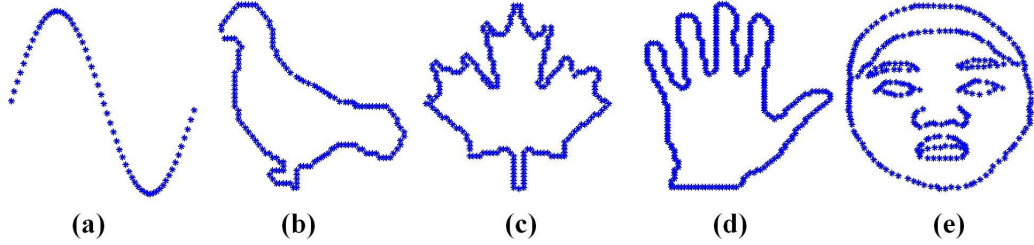


Figure 3.8: Additional point sets. : (a) Line (60 points) [16], (b) Bird1 (146 points), (c) Maple (215 points), (d) Hand (302 points) and (e) Face2D (317 points).

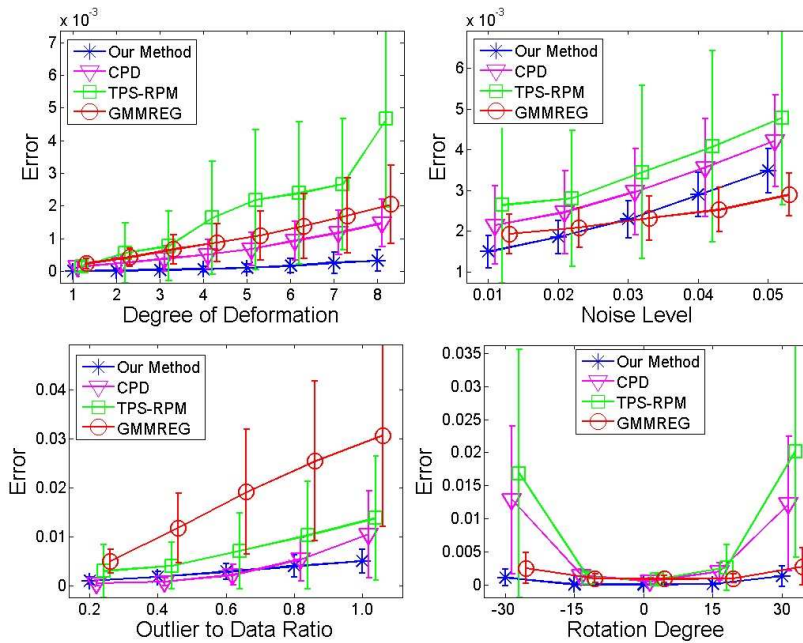


Figure 3.9: Mean performances of the four methods on the seven point sets

seven point sets are shown in Fig. 3.9. Our method shows accurate alignments in all experiments, and gives the best performances over all degrees of deformation, noise levels from 0.01 to 0.03, outlier to data ratios from 0.8 to 1.0 and all degrees of rotation. To quantify the comparison results, we score the performances from the best to the worst in each setting of each point set (e.g., the first degree of deformation in the Line point set experiment) using 4,3,2,1 according to the

calculated errors of the four methods. The summed scores and the mean scores are shown in Table 3.1.

Table 3.1: Scored non-rigid matching results and mean scores on the seven point sets

Methods	D	N
Our Method	28-28-28-28-28-28-28-28(28.0)	25-25-25-21-21(23.4)
CPD	18-19-20-20-20-20-20(19.6)	15-14-14-14-14(14.2)
TPS-RPM	15-14-12-10-10-9-10-9(11.1)	11-11-11-10-9(10.4)
GMMREG	9-9-10-12-12-13-12-13(11.3)	19-20-20-25-26(22.0)
Methods	O	R
Our Method	21-19-22-23-24(21.8)	27-28-28-28-27(27.6)
CPD	26-28-25-23-21(24.6)	11-10-20-11-13(13.0)
TPS-RPM	15-16-16-17-18(16.4)	10-17-12-17-12(13.6)
GMMREG	8-7-7-7-7(7.2)	22-15-10-14-18(15.8)

The D, N, O and R indicate the deformation, noise, outlier and rotation experiments, respectively. The maximum and minimum of summed scores on the seven point sets for each setting are 28 and 7, respectively. If two methods have the same mean error, the two methods will be scored with the same score, and the next rank will be stripped. From left to right, the scores indicate the performances from the first to the eighth degree in the deformation experiments, the performances from 0.01 to 0.05 in the noise experiments, the performances from 0.2 to 1 in the outlier experiments and the performances from -30° to 30° in the rotation experiments.

The results verify that our method is robust to different geometrical shapes and is stable to the initial parameter values. Furthermore our method gives the best overall performances in the deformation, noise and rotation experiments, and the very similar performance to the CPD which performs best in the outlier experiments. Registration examples are shown in Fig. 3.10.

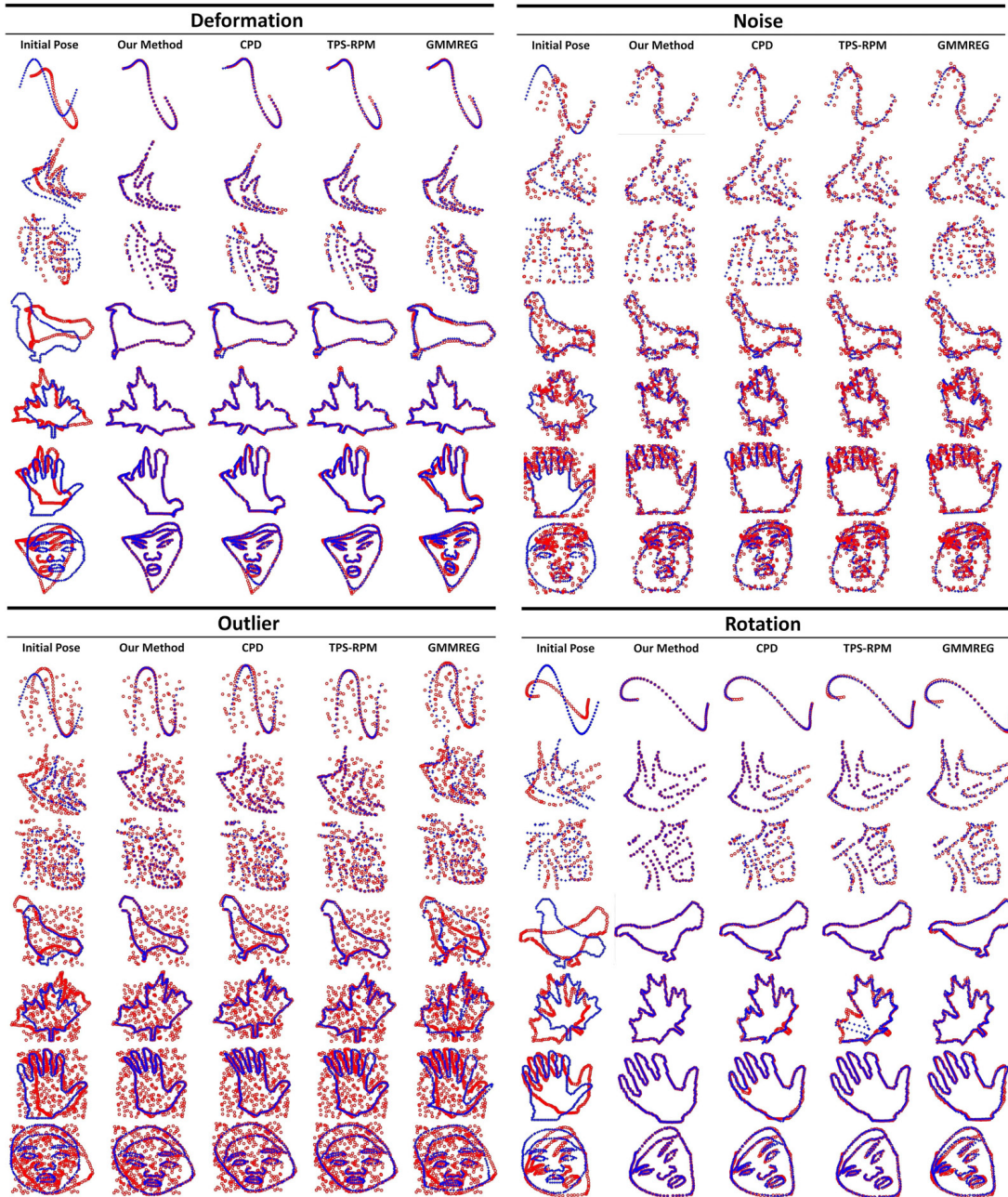


Figure 3.10: Registration examples on the seven point sets. All results shown here are under the settings of the 8th degree of deformation, the 3rd noise level, the outlier to data ratio as 1 and the 30° rotation for the deformation, noise, outlier and rotation experiments, respectively. For the noise, outlier and rotation cases, the target point sets were also warped by the 4th degree of deformation.

3.1.3 Performance on Partial Matching

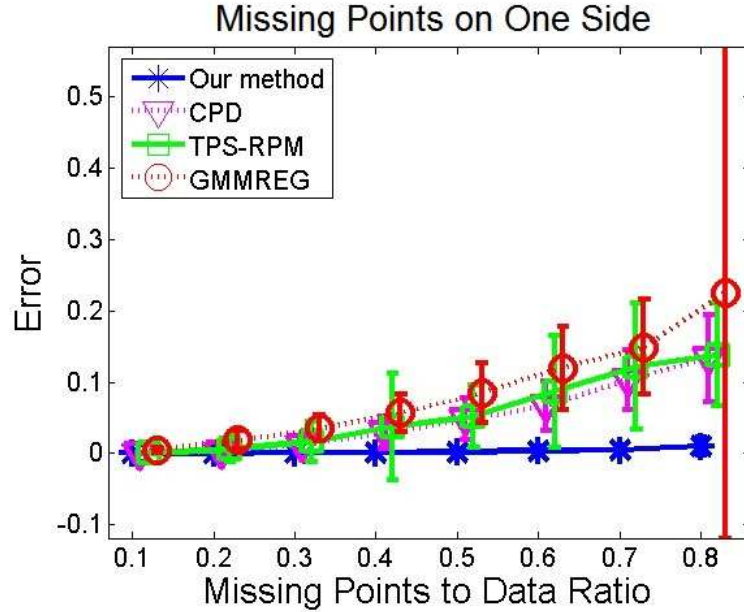


Figure 3.11: Performances with missing points. The parameter settings of our method, TPS-RPM and GMMREG were set as in Section 3.2.1. For CPD, we followed its published setting ($\lambda = 2$, $\beta = 2$ and $w = 0.5$) for the non-rigid missing point case in [24].

There are typically two types of partial matching: missing points on one side and on both sides. Our method is robust to the first case, but may not be able to cope well with missing points on both sides since it forces one-to-one correspondence even if corresponding points (in the target point set) do not exist. The performances of the four methods with missing points on the source point set are shown in Fig. 3.11. The location of missing part was randomly determined, while the target point set was also randomly warped by the fourth degree of deformation. One hundred random experiments were repeated for each missing point ratio setting. Our method gives the best performances over all the ratios, and shows very accurate results (Error < 0.0019) when the ratio is below 0.5.

Registration examples are shown in Fig. 3.12.

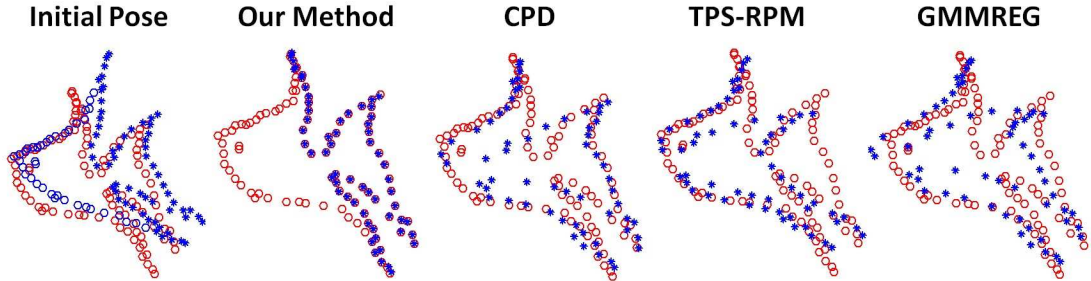


Figure 3.12: Matching examples in missing point experiment. Missing points to data ratio: 0.4. The blue circles in the initial pose indicate the missing parts.

3.1.4 Performance with Variable Numbers of Neighboring Points

The number of neighboring points K plays an important role in measuring local similarity, preserving topological structure and dealing with noise, outliers and rotation during registration. Adjusting the number of neighboring points makes our method better behaved. In this section, we give several examples in improving the performance of our method by adjusting the number of neighboring points.

High sampling rate case: Many studies in medical imaging sought to use more sampling points to align two shape models for observing local differences such as muscle deformation [40, 41, 42, 43], stomach deformation [31], breathing motion [32], brain mapping [28] and animal skeleton [44]. In these cases, a small local segment in a point set is represented by more points. Thus increasing the number of neighboring points will help to improve the local similarity measurement. A point set (Bird2) with 1715 points, which has the similar geometrical shape with Bird1 but with more details in its feet and tail, is used in this ex-

periment. To select a proper K for this point set, we tested the performances with different numbers of neighboring points on the former seven point sets. Fig. 3.13 shows the mean performances of our method with respect to the different numbers of neighboring points on the seven point sets. Our method generally performs well around the additional neighboring points to data ratio with 0.012.

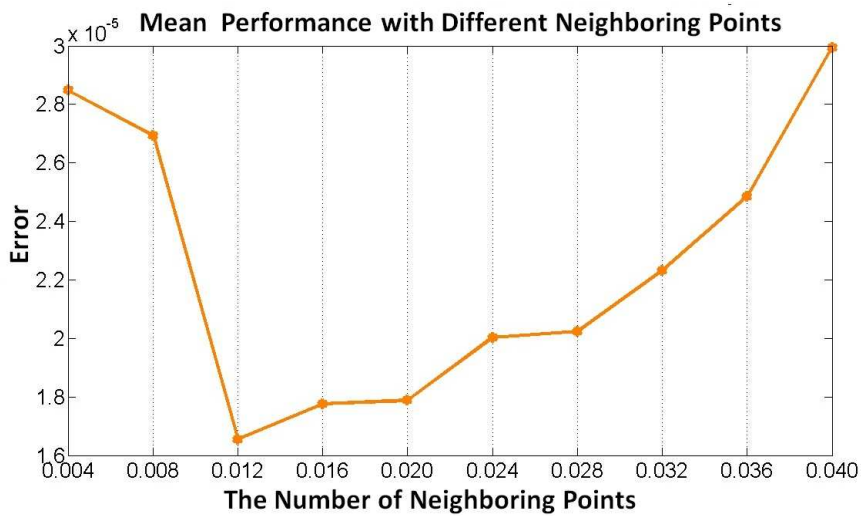


Figure 3.13: Mean performances with respect to the different numbers of neighboring points. x axis indicates the number of additional neighboring points to data (the number of points in each point set) ratio. We start at two neighboring points, and then add the additional neighboring points to test the performances of our method. The actual used number of neighboring points is equal to $2 + \text{data} \times \text{ratio}$.

According to this result, we chose 23 ($\lfloor 2 + 0.012 * 1715 \rfloor$) as a optimized K for Bird2. The performances of the four methods on this point set are given in Fig. 3.14 top, and the comparison results between $K = 5$ and $K = 23$ are shown in Fig. 3.14 bottom. Registration examples are demonstrated in Fig. 3.15. Based on these results, our method with the initial $K = 5$ still gives very accurate results and the best alignments over all degrees of deformation. Furthermore, the accuracy and stability of the performance are obviously improved using the

optimized $K = 23$.

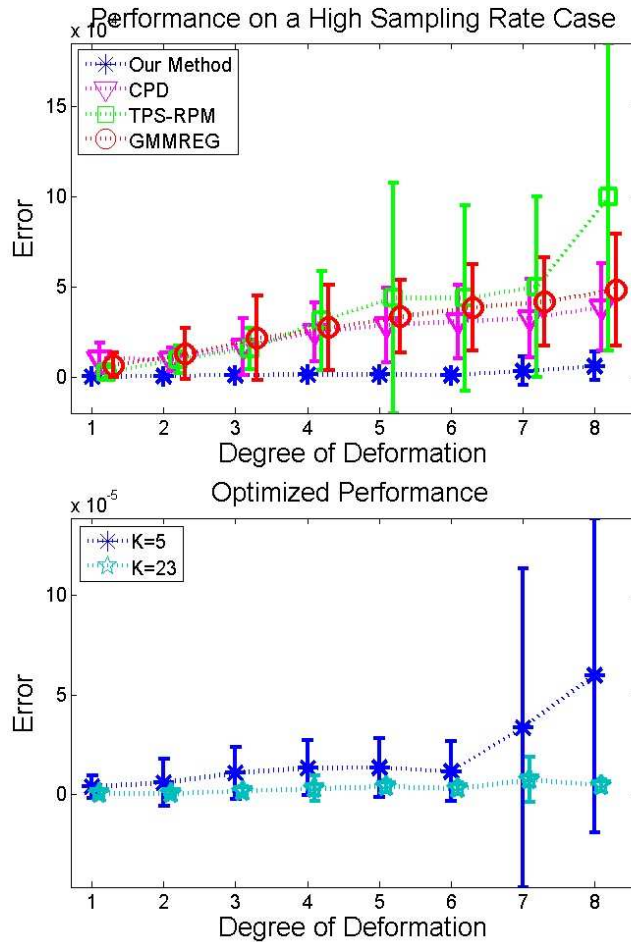


Figure 3.14: Experimental results on Bird2. Top: the performances of the four methods. Bottom: the performances of our method using different numbers of closest points.

Noise, outlier and rotation: Noise is generated by a Gaussian white noise function from the original points such that the points deviate from their original locations and the geometrical shape represented by the deviated points become fuzzy. The registration process in dealing with noise is similar to the fitting of a set of data points with linear least squares. In our method, minimizing the global distance may be considered to be a linear least squares solution. There-

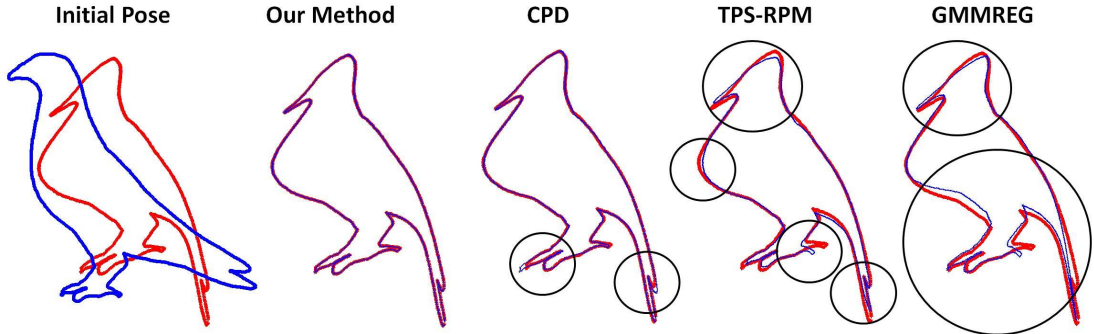


Figure 3.15: Matching examples in a high sampling rate experiment. The deformation was under the 6^{th} degree. The blue and red shapes indicate the source and target point set, respectively. The parameter settings of the four methods were the same as set in the former Fish1 experiment. The mismatches are pointed out by the black circles.

fore, decreasing the number of neighboring points may reduce the influence of minimizing local distances and tend to minimize the global distance more quickly (i.e., minimizing the global distance using more iterations) since the summed local distance has become smaller before reducing α . Moreover, the outliers in non-rigid point set registration problems are considered as points that markedly (or unmarkedly) deviate from the original points. The outliers disrupt the local structures of the original points. Therefore, using a relatively small number of neighboring points may help to distinguish such outliers since a outlier combined with its fewer neighboring points may not construct a meaningful local structure. In addition, reasonably increasing the number of neighboring points may reduce the influence of rotation since a point combined with more neighboring points may construct a bigger local segment.

To demonstrate the performances of our method with optimized K in noise, outlier and rotation experiments, we chose the Chinese Character (where our method performed relatively poorly in the noise and outlier experiments) and

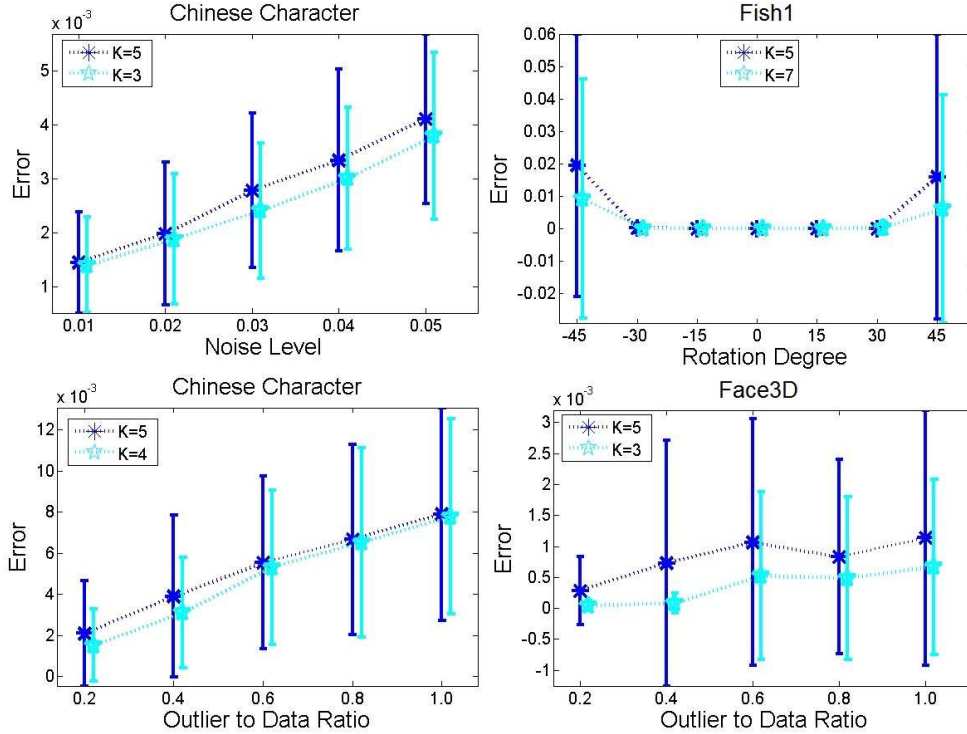


Figure 3.16: Performances with optimized K in the noise, outlier and rotation experiments.

the Face3D for the noise and outlier experiments, and the Fish1 for the rotation experiment. The results are shown in Fig. 3.16. All the performances are improved by adjusting the number of neighboring points K . Based on these results, the number of neighboring points K combines a more flexible control in dealing with deformation, noise, outliers and rotation with accurate performance.

3.2 Experiments on Sequence Images

In the second series of experiments, we evaluate the performance of our method in the feature point matchings under sequence images. Compared with the shape contour point sets, feature point sets in sequence images have relatively fewer

points that sparsely distribute on images. The CMU house is one of the most popular point sets and has been commonly used to test the performances of graph based methods. The house dataset consist of 111 frames and each frame has 30 labeled landmarks. We compared the performance of our method against three state-of-the-art graph based methods: Caetano et al. [10], Leordeanu et al. [12] and FGM [11] under all possible image pairs. The results are shown in Table 3.2. Our method gives the perfect matching results in all possible image pairs, and outperforms the three graph based methods. One representative matching example is shown in Fig. 3.17.

Table 3.2: Matching rates on the CMU house for all possible image pairs. For FGM and Caetano et al., we report upper bounds of their published results. For Leordeanu et al., we report their published results. S and U denote 'supervised' and 'unsupervised', respectively. The numbers in S and U denote the number of training image pairs.

Our method	FGM	Leordeanu et al.	Caetano et al.
K=5		$S(5)$	$U(5)$
			$S(106)$
100%	<100%	99.8%	99.8%
			<96%

3.3 Experiments on Real Images

In the third series of experiments, we test the performances of our method in the dataset from [12]. This dataset consists of 30 pairs of car images and 20 pairs of motorbike images selected from Pascal 2007 Challenge. Each pair contains 30 ~ 60 feature points. We compared the performances of our method against the FGM [11] and Leordeanu et al. [12]. The results are listed in Table 3.3. Our matching rate is higher than their published results. Matching examples are

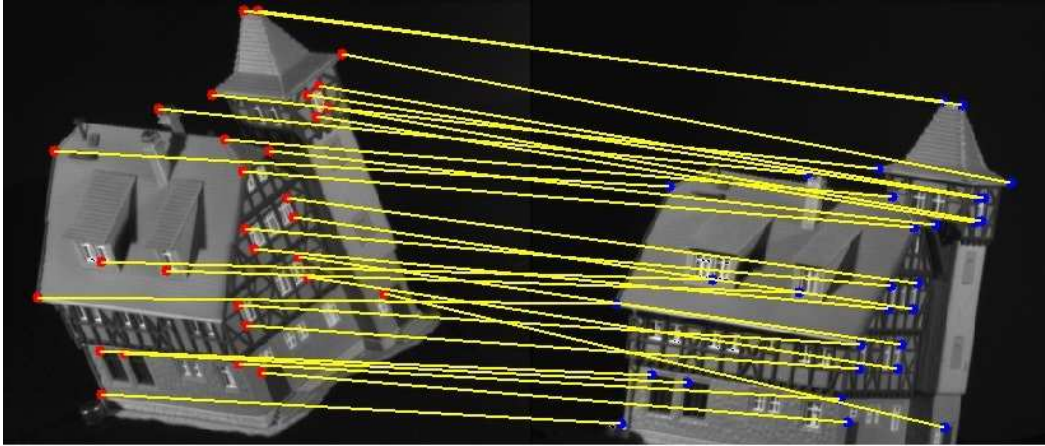


Figure 3.17: Wide baseline matching example on the CMU House: the 1th image matching with the 111th image (30/30 correct matches).

shown in Fig. 3.18.

Table 3.3: Matching rates on cars and motorbikes. For the FGM and Leordeanu et al., we report their published results. L: after learning.

Our method	FGM	Leordeanu et al.
K=5		L
93%	80%	80%

3.4 Computational Complexity

The computational cost in our method is mainly related to two aspects: (a) the annealing parameters T_{init} , T_{final} and r which determine the convergence range and (b) the linear assignment solution which determines the worst-cost time of solving the correspondence matrix.

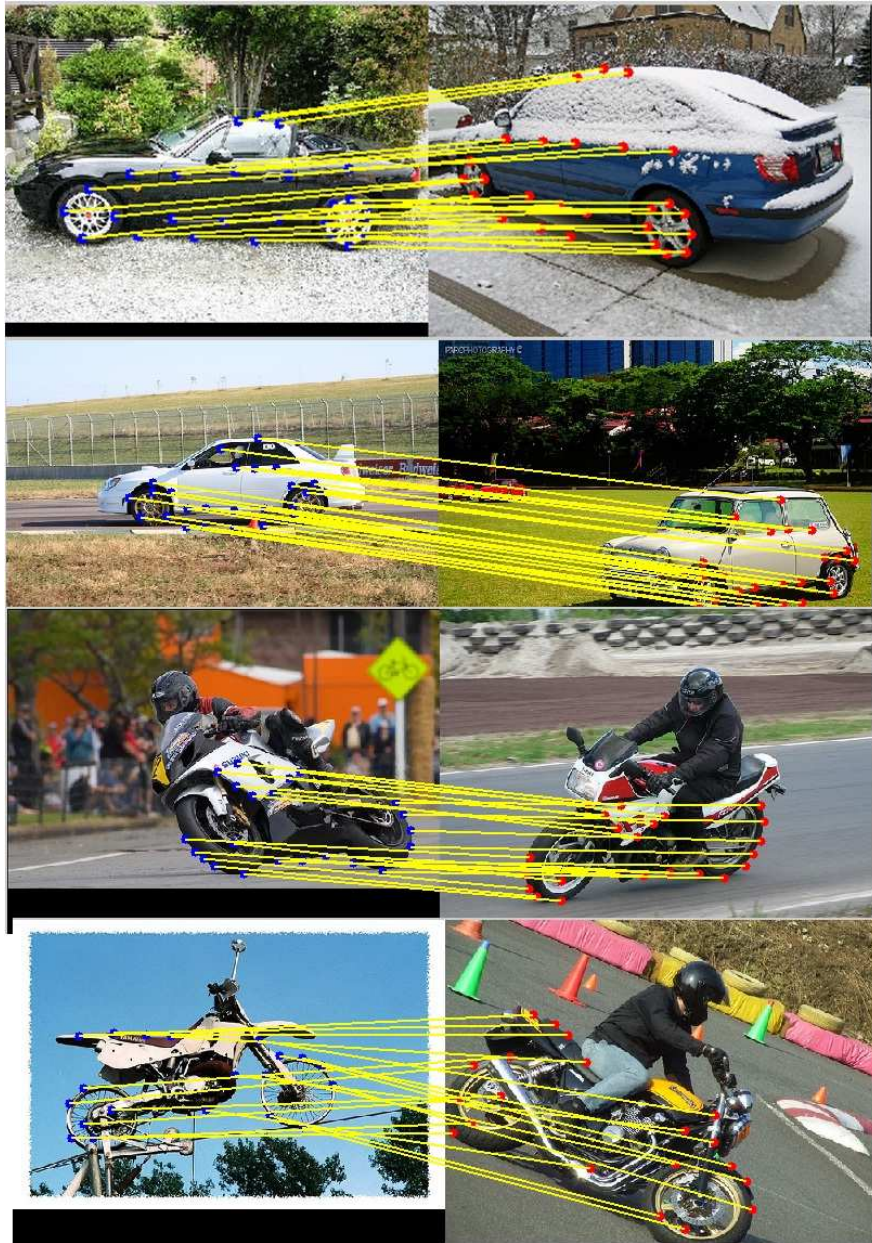


Figure 3.18: Matching examples on cars and motorbikes.

3.4.1 Convergence Range

The convergence range of our method is determined by the deformation degree of target point set since r is fixed as 0.7, and T_{init} and T_{final} are determined by the

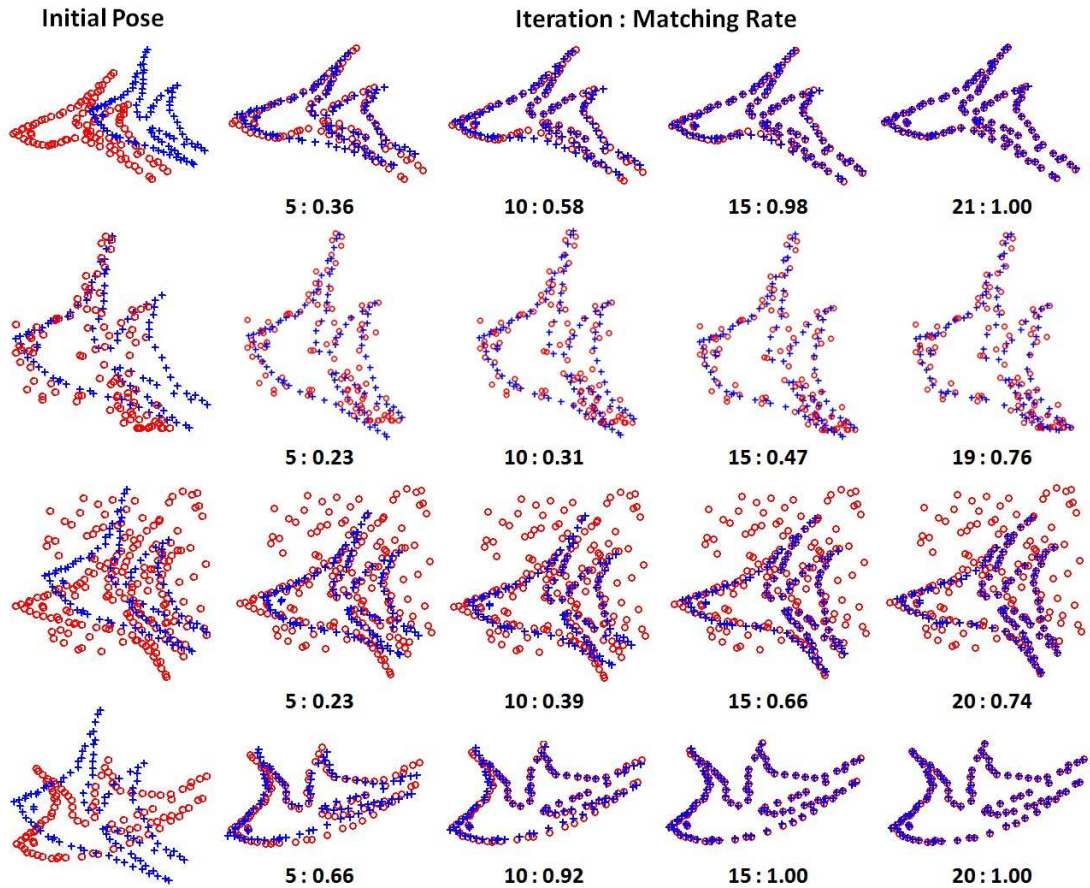


Figure 3.19: Registration performances with different iterations. The target point sets (from top to bottom) for deformation, noise, outlier and rotation experiments are set by the 8th degree of deformation, the 3rd noise level, the outlier to data ratio as 1 and the 30° rotation, respectively. For the noise, outlier and rotation, the target point sets were also warped by the 4th degree of deformation.

squared distance between points (see the annealing parameter setting in section 2.3). In the other three methods, the convergence ranges are determined by the annealing scheme in the TPS-RPM, and the tolerance stopping criterion and the maximum iteration in the CPD and GMMREG. We investigate the convergence ranges of the four methods under the largest deformation of Fish1. The parameter settings for the three methods follow the values used in the former Fish1 experi-

ment. On average, CPD required 33 iterations and TPS-RPM 94 iterations while GMMREG used the maximum iteration (100 iterations) in all experiments since the L2 distance was difficult to reach at the given tolerance stopping criterion as 10^{-10} . Our method took relatively fewer iterations as 21 on average based on our original parameter settings (section 2.3). To demonstrate the convergences of our method in deformation, noise, outlier and rotation experiments, Fig. 3.19 shows the registration performances with different iterations on the Fish1 point sets.

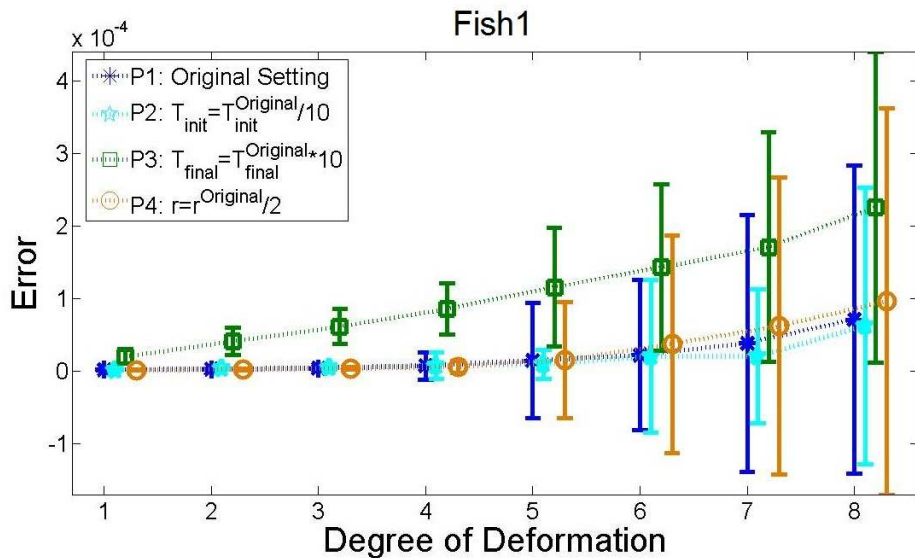


Figure 3.20: Relationships between performances and different annealing parameter settings.

In addition, we also investigated the performances of our method with different annealing parameter settings. Fig. 3.20 shows an example on the Fish1 point set. For each annealing parameter setting, one hundred random experiments were repeated on each deformation degree. According to the results shown in Fig. 3.20, the performance with reducing the T_{init} was slightly improved and the registration iterations were reduced about 33% (from 21 iterations on average to

14 iterations); the performances with increasing the T_{final} were degraded and the registration iterations were reduced about 33% (from 21 to 14); the performances with reducing the annealing rate r were slightly degraded and the registration iterations were reduced about 62% (from 21 to 8). All the experiments still show very high accuracies (i.e., the errors were less than 0.00023 and the standard deviations were within ± 0.00027) even if the annealing parameters were significantly changed. Based on these results, the computational cost in our method can be substantially reduced by adjusting the annealing parameter settings while still maintaining accurate alignment.

3.4.2 Performance of Jonker-Volgenant Algorithm

Table 3.4: Performance of Jonker-Volgenant algorithm. We tested the performance of Jonker-Volgenant algorithm in Matlab (using a Mex file) on a PC with 4 GB of RAM and 2.67 GHz Intel(R) Xeon(R) CPU. The cost matrices were generated by Matlab *rand* function.

Size	200	500	1000	2000	3000
Time Cost (s)	0.002	0.016	0.100	0.316	0.588

To solve the correspondence matrix using a linear assignment solution, the Jonker-Volgenant algorithm [34] which has the worst-cost time $O(N^3)$ has been employed in this work. The time costs on the different sizes of cost matrices are listed in Table 3.4. The Jonker-Volgenant algorithm demonstrates fast solutions that make our method achieve a fast solution for non-rigid point set registration problems.

3.4.3 Total Computational Time

In addition to the convergence range, the total computational time of each method will also depend on the programming language and program optimization. Furthermore, a tradeoff between the computational time and the registration accuracy exists must be adequately considered. Since the CPD and GMMREG methods are mostly implemented in C++ and the four methods gave different accuracies, we do not compare the total computational time of our method against the other methods. Here, we only give the total computational times of our method on several examples in Table 3.5. In our method, only the Jonker-Volgenant algorithm is implemented in C++, the other processes are purely implemented in Matlab.

Table 3.5: Computational times. The total computational times of our method were tested under the largest degree of deformation in Matlab (on the same PC used in Table 5). The parameter setting was based on the original setting described in Section 2.4. Fish1: 98 points; Hand: 302 points; Face3D: 392 points; Bird2: 1715 points.

Point Set	Fish1	Hand	Face3D	Bird2
Time Cost	0.19s	1.13s	1.70s	77.88s

3.5 Registration Examples by GLMDGRBF

In this section, we present the performances of GLMDGRBF in dealing with unknown deformation, noise, outliers and rotation on the former Fish1, Chinese Character, Fish2 and Face3D point sets and also compare against to TPS-RPM [16], CPD [24] and GMMREG [14]. The experiment designs and the error measurement for the deformation, noise, outliers and rotation experiments are the

same as described in section 3.1.1.

The performance statistics (the mean error and its standard deviation) on the four point sets are shown in Fig. 3.21.

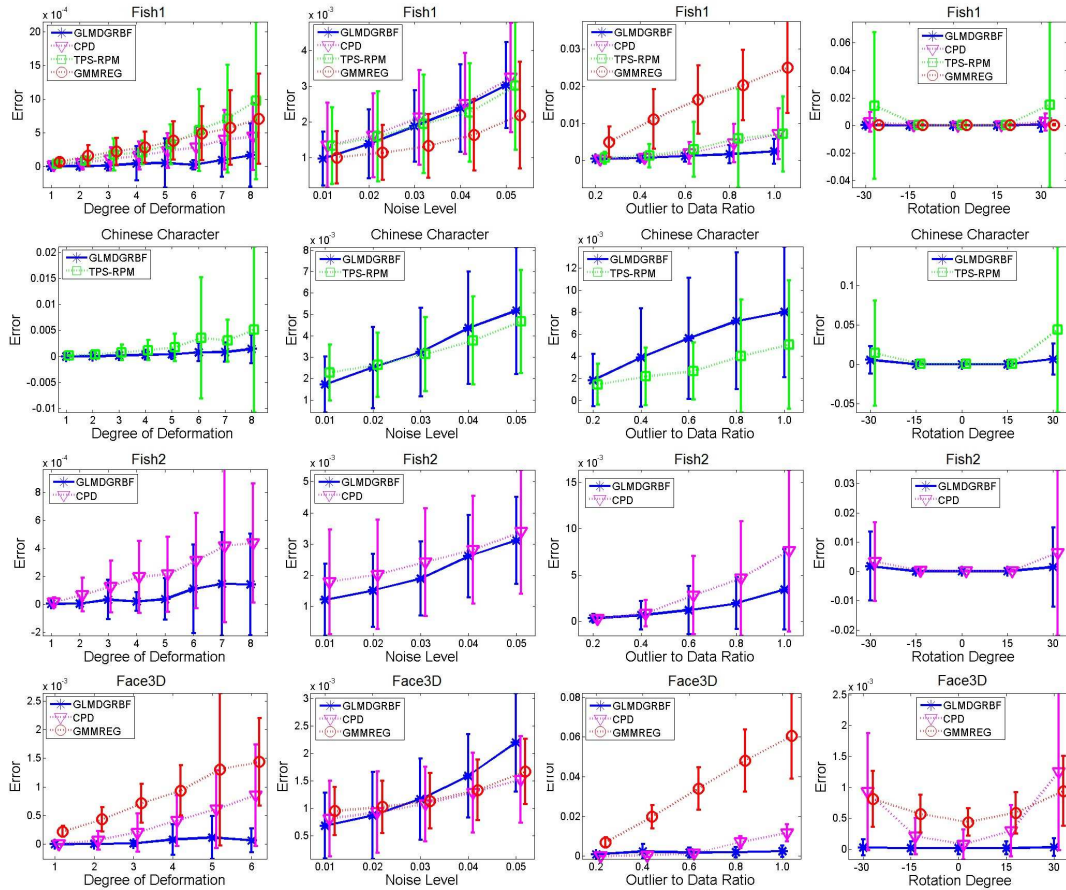


Figure 3.21: Comparison of GLMDGRBF (*) against CPD (∇), TPS-RPM (□) and GMMREG (○) on the four point sets. The error bars indicate the standard deviations of the mean errors in 100 random experiments. From the top row to bottom row are: Fish1, Chinese Character, Fish2 and Face3D, respectively.

In the Fish1 experiments (the first row of Fig. 3.21), GLMDGRBF shows accurate alignments in all experiments, and gives the best performances over all degrees of deformation, outlier to data ratios from 0.4 to 1.0 and degrees of rotation from -30° to 15° . In the noise experiment, all the four methods give

accurate alignments while the GMMREG generally performed better.

In the Chinese Character experiments (the second row of Fig. 3.21), GLMD-GRBF shows accurate alignments and gives the best performances over all degrees of deformation, the noise levels from 0.01 to 0.02 and all degrees of rotation. In the outlier experiment, the TPS-RPM performs better. The reason of why GLMD-GRBF performed relatively poorly is similar with GLMDTPS as discussed in section 3.1.1.

In the Fish2 experiments (the third row of Fig. 3.21), GLMDGRBF shows accurate alignments in all experiments, and gives the best performances over all degrees of deformation, all noise levels, outlier ratios from 0.4 to 1.0, and all degrees of rotation.

In the Face3D point set (the fourth row of Fig. 3.21), GLMDGRBF shows accurate alignments in all experiments, and gives the best performances over deformation degrees from the second to the eighth degrees, noise levels from 0.01 to 0.02, outlier ratios from 0.8 to 1.0 and all degrees of rotation.

To summarize, GLMDGRBF shows the best alignments in most scenarios, in particular, it obviously outperforms the other three in the deformation and rotation experiments.

3.6 Conclusion

We have introduced GLMDTPS and GLMDGRBF that employ a global and local mixture distance based correspondence estimation with TPS and GRBF transformation, respectively. We first defined a global distance and a local distance for measuring the global and local differences between two point sets, respectively.

We then combined the two distances to be a mixture distance based cost matrix to estimate correspondences during the matching. A novel annealing scheme was designed to smoothly control the correspondence estimation and the transformation updating.

Carefully designed experiments were undertaken to demonstrate the robustness and stability of GLMDTPS and GLMDGRBF. Comparing the performances of our methods against the current state-of-the-art methods, both GLMDTPS and GLMDRBF shows the best performances in most scenarios. The significant contributions of the proposed method include the following:

- Minimizing the local distance preserves the topological structure of the point sets. Moreover, the Euclidean distance between two point sets is always minimized by the global distance minimization at the end of registration.
- The designed GLMD based cost matrix provides a flexible way to estimate the correspondences by multiple features.
- Unlike the single feature based correspondence estimation in the current methods, the designed annealing scheme combined with the GLMD based cost matrix improves the flexibility and accuracy of the correspondence estimation using both local and global distance features. Moreover, it also enhances the interaction between the two steps during registration.
- The number of neighboring points K combines greater flexibility in dealing with deformation, noise, outliers and rotation with accurate performance.

In addition, the idea of building the GLMD based cost matrix creates a new

approach "Global feature + $\alpha \times$ Local feature" which allows to employ multi-feature for estimating correspondence. This new framework may lead to more multi-feature based non-rigid point set matching methods in future.

Chapter 4

Related Work and Comparison

In this chapter, we first theoretically describe the methodological differences between the two combinations (GLMDTPS and GLMDGRBF) and the related works, and then empirically discuss the advantages and disadvantages between our methods and the related methods based on a comprehensive review of the experimental comparisons demonstrated in the last chapter. At the end of this chapter, we discuss the differences between the TPS and GRBF transformations, and compare the performances of GLMDTPS and GLMDGRBF in non-rigid point set registration problems.

4.1 Related Work

There are three aforementioned methods TPS-RPM [16], CPD [24] and GMM-REG [14] that are related to GLMDTPS and GLMDGRBF. Table 4.1 lists the methodological differences between the two combinations and the other three methods.

[htb!]

Table 4.1: Methodological differences between our methods and the current methods

Methods	Correspondence Estimation		Transformation Update	
	Using Feature	Correspondence	Constraint	Transformation
GLMDTPS	GLMD	B	TPS Energy1	TPS
GLMDGRBF	GLMD	B	GRBF Energy	GRBF
TPS-RPM	GPD	F	TPS Energy2	TPS
CPD	GPD	F	MCC-NLL	GRBF
GMMREG	GPD	F	Mini-L2	TPS

GPD: Gaussian probability density; GLMD: global and local mixture distance; B: binary; F: fuzzy; GRBF: Gaussian radial basis function; TPS: thin plate spline; MCC-NLL: Motion coherent constraint based negative log-likelihood; Mini-L2: Minimizing L2 distance. Note that in TPS Energy2 a term $\lambda_2 \text{trace}[d - I]^T [d - I]$ is added to (2.9) to penalize the affine transformation.

- Correspondence estimation:** Unlike single feature based correspondence estimations in the current methods, GLMDTPS and GLMDGRBF minimize a multi-feature (i.e., GLMD) based cost matrix by a linear assignment solution which provides a binary correspondence and guarantees one-to-one correspondence. Moreover, the correspondence estimations in the other three methods are determined by a fuzzy correspondence using Gaussian probability density that is mainly related to $\| \mathbf{x}_i^w - \mathbf{y}_i \|^2$ as our defined global distance. Compared with the three methods, the defined local distance feature is more stable and robust (than $\| \mathbf{x}_i^w - \mathbf{y}_i \|^2$) for correspondence estimation at the begin of registration, and helps the warping template more quickly (using fewer iterations) achieve a better posture for the subsequent more non-rigid registration. To avoid mismatches by neighboring points having similar local structures (such as the aforementioned

limitations in point distribution and graph based methods), minimizing the local distance is replaced by minimizing the global structure difference at the end of registration, which always minimizes the Euclidean distance between two point sets (i.e., we solve the issue in the GMMREG method).

- **Transformation updating:** GLMDTPS and GLMDGRBF minimize the standard TPS energy and GRBF energy, respectively. TPS-RPM also employs TPS energy to update the transformation, but it adds a penalty term $\lambda_2 \text{trace}[\mathbf{d} - \mathbf{I}]^T [\mathbf{d} - \mathbf{I}]$ for the affine coefficient \mathbf{d} . GLMDTPS only penalizes the non-rigid warping coefficient w , and since it returns a relatively accurate binary correspondence to the transformation at each iteration, a free affine transformation will be helpful to quickly (using fewer iterations) achieve a better posture (\mathbf{x}^w) for the subsequent more non-rigid matching. In addition, CPD and GMMREG minimize the motion coherent constraint based negative log-likelihood and the L2 distance, respectively, to update the transformation.
- **Fuzzy correspondence Vs. Binary correspondence:** The transformations built by the fuzzy correspondences in the three methods give fuzzy location and geometrical structure updating for the warping template. These may cause the registration process to take relatively more iterations and not be always effective for the warping template updating. In our method, the series of binary correspondences estimated by the defined local distance feature clearly guide the location and geometrical structure updating with rigid transformations at the begin of registration. Consequently the achieved better posture makes the subsequent correspondence estimation

using the global distance feature easier.

- **Topological structure:** Unlike forcing points to move coherently in the CPD, we fix neighboring relations $\mathbf{N}(\mathbf{x}_i^w)$ and $\mathbf{N}(\mathbf{y}_i)$ during the warpings of \mathbf{x}^w . Thus, minimizing the local distance preserves the topological structure of the warping template, while also avoids the position deviations issues such as in the CPD method.
- **Flexibility:** The TPS-RPM and CPD methods consider the outlier rejection as an unsupervised clustering problem, and the GMMREG rejects outliers by its defined Gaussian component which is mainly related to the Mahalanobis distance [45]. In our method, the local distance determines the measurements of local similarities between two point sets, and provides an adjustable parameter K (the number of neighboring points) for flexibly dealing with registrations under different levels of deformation, noise, outliers, rotation and missing points (see section 3.1.4).
- **Interaction between two steps:** The annealing scheme combined with the GLMD based cost matrix improves the flexibility and accuracy of the correspondence estimation using both local and global distance features, and also enhances the interaction between the two steps during registration.

Based on the above methodological differences as well as the interaction between correspondence estimation and transformation updating, we consider the binary correspondence to be more effective than the fuzzy correspondence since a non-rigid transformation built by a fuzzy correspondence leads to 'fuzzy location updating' for the warping template. This may cause the matching process to

take relatively more iterations and may always not be effective in updating the locations of the warping template. That may be a major reason of why CPD and GMMREG focus on developing constraints for their transformation updating.

In addition, the applicability of the above five methods are limited by different dimensions as listed in Table 4.2. Most current non-rigid point set matching methods may be well suited for 2D and 3D cases, but their generalizations to higher dimensions are not always trivial [24], e.g., the TPS parameterization does not exist when the dimension of points is higher than three. Thus, for dealing with higher dimension non-rigid point set matching problems, GRBF transformation is used instead of TPS transformation since it can be easily generalized to N dimensions.

Table 4.2: Applicability in different dimensional problems

Methods	2D	3D	Higher Dimensions (>3)
GLMDTPS	✓	✓	×
GLMDGRBF	✓	✓	✓
TPS-RPM	✓	✓	×
CPD	✓	✓	✓
GMMREG	✓	✓	×

✓: able to handle. ×: unable to handle.

4.2 Empirical Comparison between GLMD based Methods and Current Methods

According to the above discussed methodological differences between our methods and the other three methods, we can now more easily review the experimental

results (Table 3.1 in section 3.1.1) on the seven point sets.

- In the deformation experiments, the best overall performance is obtained by our method (28.0) followed by the mean score calculated in Table. 3.1. The reason for CPD performing better than GMMREG and TPS-RPM is mainly related to the fact that CPD preserves the topological structures by forcing the points to move coherently during the matchings. However CPD does not improve the correspondence searching process which still uses the global distance relationship between two point sets to assign the corresponding probabilities as in TPS-RPM. In GMMREG, although the L2 distance between two Gaussian mixture models is minimized (the idea is similar to the fitting a set of data points with least squares solution), it does not mean that the Euclidean distance between two point sets is always minimized. Thus GMMREG only slightly outperforms TPS-RPM in the deformation experiments. In our method, correspondence estimation is improved using both local and global distance features, while minimizing the local distances and the interaction between correspondence estimation and transformation updating preserve the local structures of the warping templates. As a consequence, our method outperforms the other three methods in the deformation experiments.
- In the noise experiments, our method (23.4) performs better than GMM-REG (22.0), CPD (14.2) and TPS-RPM (10.4). In these experiments, the source point sets were added with Gaussian white noise such that the shapes of the source templates become fuzzy. Thus the matching processes of the four methods are similar to the fitting a set of data points with least squares

solution. In the CPD, forcing the points to move coherently preserves the topological structure, but may produce a relatively large error when one point is mismatched and is undesirable when source points need to be moved in different directions to match their target points. In our method and the GMMREG, minimizing the global distance and L2 distance, respectively, can be considered a least squares solution.

- In the outlier experiments, CPD (24.6) performs better than our method (21.8), TPS-RPM (16.4) and GMMREG (7.2). An additional uniform distribution is added to the Gaussian mixture model to account for outliers in CPD, and an outlier cluster for each point-set is placed at the center of mass to take into account outliers in TPS-RPM. In our method, outliers are rejected by minimizing the local distances (the K is fixed by 5) and the rigid transformations. However outliers in the Gaussian mixture model of the target point set are only distinguished by Mahalanobis distances [45] in GMMREG.
- In the rotation experiments, our method (27.6) performs better than GMMREG (15.8), TPS-RPM (13.6) and CPD (13.0). Our method gives the best result since minimizing the local distance is robust to rotations. Moreover, in GMMREG, matching of geometric shapes is considered as a density based registration such that GMMREG is also robust to rotations. However there is no feature that is robust to rotation in both TPS-RPM and CPD, and thus these two methods give relatively poor performances in the rotation experiments.

4.3 TPS vs. GRBF

Both TPS and GRBF are derived from a standard radial basis function

$$f(\mathbf{x}) = \sum_{i=1}^K \mathbf{w}_i \phi(\|\mathbf{x} - \mathbf{c}_i\|) \quad (4.1)$$

where $\{\mathbf{w}_i\}$ is set of mapping coefficients and $\|\cdot\|$ denotes the Euclidean norm. $\{\mathbf{c}_i\}$ is a list of control points and ϕ is the kernel function with different forms. If we select the kernel function to be $\phi(\mathbf{r}) = \mathbf{r}^2 \log \mathbf{r}$, $f(\mathbf{x})$ becomes the TPS function. Moreover, TPS can always be decomposed into a global affine and a local non-rigid component [36] (see (2.7)). If we choose $\phi(\mathbf{r}) = \exp(-\mathbf{r}^2/\sigma^2)$, it becomes GRBF where the parameter σ controls the width of each kernel function. Compared to GRBF, TPS has a more global nature: "a small perturbation of one of the control points always affects the coefficients to all the other points as well" [16].

In addition to the differences in the forms, TPS and GRBF also contain different smoothness constraints in their minimizing energy functions as described in (2.8) and (2.16), respectively. The smoothness constraints are used to prevent arbitrary mappings between two point sets since there is an infinite number of ways to map one point set to another in non-rigid matching. Moreover, as discussed in Table 4.2, TPS parameterization does not exist when the dimension of points is higher than three, and GRBF may be easily generalized to N dimensions.

4.4 Experimental Comparison between GLMDTPS and GLMDGRBF

In order to compare the performances between GLMDTPS and GLMDGRBF, we selected the former four point sets: Fish1, Chinese Character, Fish2 and Face3D, and evaluated GLMDTPS and GLMDGRBF in dealing with unknown deformation, noise, outliers and rotation on the four point sets. The performance statistics are shown in Fig. 4.1.

Both GLMDTPS and GLMDGRBF show accurate results in all the experiments. In the *Fish1* experiments, GLMDTPS generally gives relatively more stable performances in the four experiments. GLMDGRBF slightly outperforms GLMDTPS in the outlier experiments, but shows relatively unstable performances on the fourth and fifth degrees of deformation, and -30° and 30° of rotations. In the *Chinese Character* experiments, GLMDTPS generally performs better than GLMDGRBF in all cases. In the *Fish2* experiment, GLMDTPS shows relatively stable performances in the deformation and rotation experiments, and both methods give a very similar results in the noise experiment. In the outlier experiments, GLMDGRBF performs better than GLMDTPS. In the *Face3D* experiments, GLMDTPS shows more accurate and stable alignments than GLMDGRBF in all the experiments.

To summarize, GLMDTPS and GLMDGRBF show very similar alignments in both 2D and 3D cases (compared with the alignments given by the other three methods). GLMDTPS performs relatively better, but it may not be able to deal with the non-rigid point set matching problems when the point dimension is more than three.

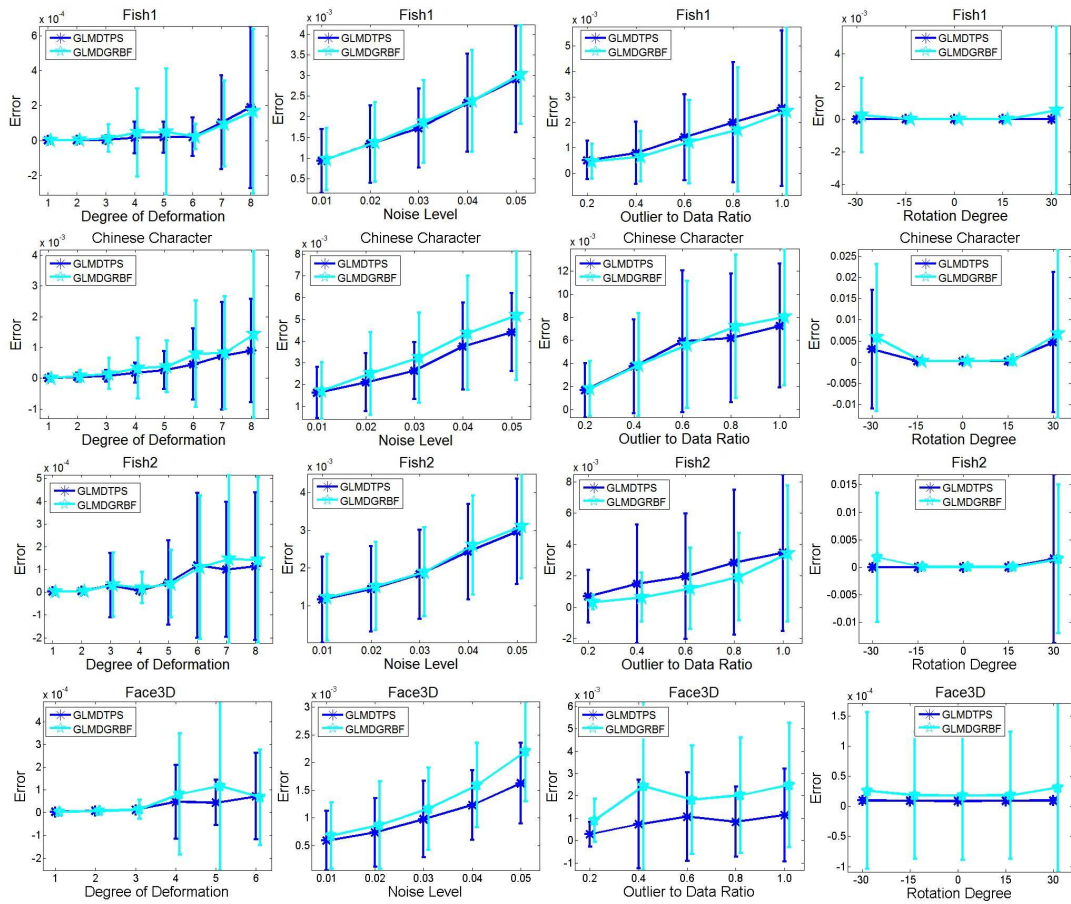


Figure 4.1: Comparison between GLMDTPS (*) and GLMDGRBF (☆) on the four point sets. The error bars indicate the standard deviations of the mean errors in 100 random experiments. From the top row to bottom row: *Fish1*, *Chinese Character*, *Fish2* and *Face3D*, respectively.

Chapter 5

A New Framework for Assessing Human Masticatory Muscle Deformation

In the Chapter 2, 3 and 4, we have introduced a new non-rigid point set registration method. For its applications to practical problems, we chose two unresolved problems in the studies of human masticatory system: (i) masticatory muscle functional activity investigation (in Chapter 6), and (ii) biomechanical relationship between masticatory muscle activities and mandibular movements (in Chapter 7).

For exploring the above two problems, we propose a new framework to assess human masticatory muscle deformation in this chapter. The proposed framework is a useful first-cut approximation approach, and mainly based on the proposed GLMDTPS method.

5.1 Human Masticatory Muscle

There are four major groups of muscles in human masticatory system: the masseter muscle, medial pterygoid muscle, lateral pterygoid muscle and temporal muscle (as shown in Fig. 5.1). These four groups control mandibular movements for mastication and are also involved in speech and facial expressions. To clarify the muscle functional roles and diagnose masticatory system problems, the techniques assessing the muscle function activity and explaining the biomechanical relationship between the masticatory muscle activities and the mandibular movements for specific subjects are very important. However, such techniques are practically very difficult to achieve.

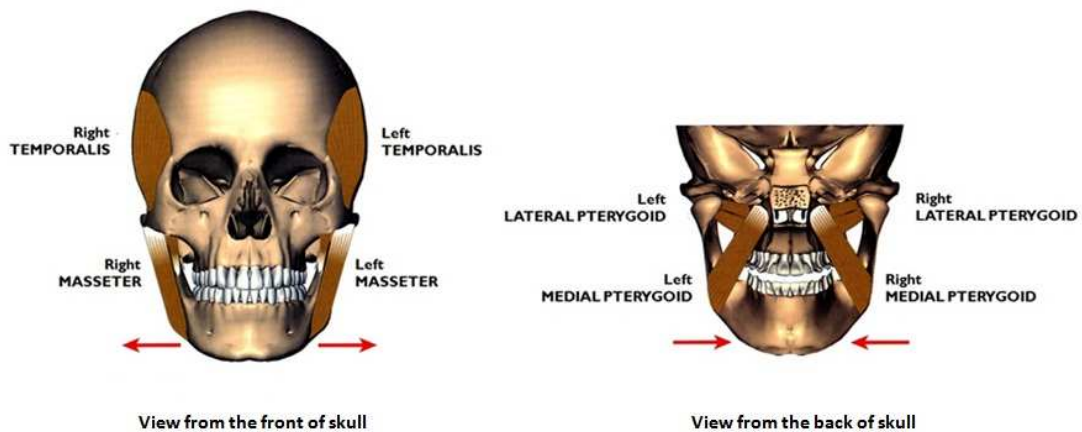


Figure 5.1: Human masticatory muscles [1]

5.2 Review of Different Approaches for Studying Human Masticatory Muscle

Generally, there are four different approaches used in previous studies of masticatory muscles as follows

- i. Anatomical study
- ii. EMG activity recording
- iii. Measurements of muscle size change
- iv. Biomechanical modeling

5.2.1 Anatomical Study

The anatomical study is a fundamental approach to understand human masticatory muscles and is mainly involved in investigating the structural characteristics of these muscles and the positional relationship between the muscles and other anatomical organizations.

The anatomical studies of human masticatory muscle started over 150 years ago [46] and are still ongoing due to the complexities of the muscle structures. In the early studies, Schumacher [47] found that the masseter muscle consists of two major compartments (the superficial and deep) with each compartment having one or more musculoaponeurotic layers. Eisler and Williams et al. [48, 49] suggested that the lateral pterygoid muscle comprises two separate heads: the superior and inferior heads. However, the lateral pterygoid muscle is not clearly separated into two independent muscles based on innervation findings near its

insertion by [50, 51]. In addition, the various muscle bundles were observed in the temporal muscles by [52, 53]. Recently, Gauty et al. [54] defined the architectural organizations of the human masseter muscle, temporal muscle and pterygoid muscles using 169 cadavers, while an combined MRI study confirmed the reality of the defined architectural arrangements. Foucart et al. [55] reported that the lateral pterygoid is composed of 5 to 6 independent functional musculoaponeurotic layers based on nerve distribution findings. More recently, the anatomical studies have been extended to investigate the positional relationship between the masticatory muscles and craniofacial hard tissues [56, 57] as well as between the masticatory muscles and their innervating nerves [58].

Such anatomical studies provide the fundamental knowledge for further exploring the muscle functions and human masticatory system, and also facilitate the studies in the latter three approaches.

5.2.2 EMG Activity Recording

EMG is a technique for recording and evaluating the electrical activity of skeletal muscle when the muscle is neurologically activated. The recorded EMG signals can be analyzed to evaluate the medical abnormalities and activation level of the muscle. Generally there are two types of EMG: the surface EMG and the intramuscular (needle) EMG. The latter is commonly used in the studies of masticatory muscles. To record the functional activities of muscle using the intramuscular EMG, a needle electrode (or multiple needle electrodes) needs to be inserted through the skin into the target muscle. In many studies of masticatory muscles, the needle electrode was placed at various locations or multiple needle

electrodes were simultaneously used to investigate the muscle functional activities in the different regions.

There is a large amount of published EMG studies on masticatory muscles. The main focus of these studies was to record EMG activities under a specified mandibular movement such as jaw opening, closing and chewing, and evaluate the muscle functions or diagnose the medical abnormalities using the recorded EMG activities. McDonald and Hannam [59] showed the activities of the masseter muscle to be sensitive to the location, size, and direction of the contact point during maximal clenching tasks. Moreover, the EMG activities of the superficial and deep parts were distinguished in the masseter muscles during maximal-effort intercuspal, incisal static clenches and open/close excursions by Blanksma et al. [60]. Gibbs et al [61] and Wood et al [62] revealed that the inferior and superior heads of lateral pterygoid muscles have different functional roles during jaw closing and jaw opening. However, Hannam and McMillan [63] and Ruangsri et al [64] have suggested that the two heads of lateral pterygoid muscle should be regarded as a single muscle. In addition, Ahlgren [65] found that the posterior part of the temporal muscle is activated in intercuspal, protruded and retruded positions of the mandible; there was no significant difference in EMG activity between the three temporal divisions in the intercuspal position; and the posterior temporal muscle predominated in retruded biting whereas the temporal muscle was mainly inactivated in protruded biting.

Based on such EMG studies, muscle functional activities under different mandibular movements have been validated. Furthermore the validated results were used to explain the basic functions of masticatory muscles. For example, masseter muscles, medial pterygoid muscles and temporal muscles have been considered to

be the same group to elevate the mandible for jaw closing, and lateral pterygoid muscles are responsible for depressing the mandible for jaw opening. In addition, the EMG activity is also considered as a ground truth for evaluating medical abnormalities in clinical diagnosis.

5.2.3 Measurement of Muscle Size Change

The measurements of muscle size changes mainly focused on investigating the morphological heterogeneity of masticatory muscles during the mandibular movements using medical imaging, such as CT, MRI and ultrasound imaging. The key idea of these studies is that the morphological heterogeneity of masticatory muscle during mandibular movements may reflect their functional roles.

Recently, Goto et al. [66] investigated the length changes of the deep and superficial compartments of the masseter muscles with various mandibular positions using MRI. The non-uniform changes in cross-sectional areas were observed by [67] when the mandible moved from the intercuspal position to the maximum jaw opened position. The lateral pterygoid muscles significantly decreased their volumes during the jaw opening, but the masseter muscles and medial pterygoid muscles only slightly changed the volumes during the jaw closing [68]. The thicknesses of the masseter muscles were measured as the medio-lateral distances of the masseter muscle from ultrasound images by Kubo et al. [69]. The results showed that the muscle thicknesses increased during the tooth clenching efforts. These reported changes in the thickness and the cross-sectional areas may be explained by the contractions of muscle fibers as well as increase in volume of the circulating blood into the muscle [70, 71].

To summarize, these studies generally reveal how the anatomical dimensions of the muscles changed with the various mandibular positions, and relate the assessed muscle size changes to explain the muscle functional roles.

5.2.4 Biomechanical Modeling

The biomechanical modeling approach has been mainly used to study the biomechanical properties of the muscles and the relationship between the muscles and surrounding hard tissues, such as mandible and condyle. Clarifying the biomechanical properties of masticatory muscle is one of the most important research aims in the studies of masticatory muscle. Unlike the studies in the first three approaches, the biomechanical properties of masticatory muscle may be directly used to explain the muscle functions and diagnose the abnormalities in masticatory system. There is a large body of literature describing the studies of masticatory muscles, but the studies in biomechanical modeling of human mastication only occupies a small place. One of the reasons for this underexposure is probably its complexity.

To model the biomechanics of human mastication, over thirty-five mixed non-linear differential and algebraic equations which describe the masticatory dynamics have been defined and solved with numerical integration by [72]. The relevant morphologies such as TMJ, muscle attachment sites and the mandible were obtained from biomedical images and digitised dental casts [73]. In many cases, the inertial properties of the jaw were estimated from simple linear jaw dimensions alone [74], and the muscles were modeled as Hill-type phenomenological models which decompose a muscle into length and velocity-dependent active and passive

force components [75]. A dynamic jaw model incorporating the structural and functional variables has been performed in customized and generic engineering software packages by [76].

Such biomechanical models provide an overview for the general masticatory system, and are expected to be applied in specific clinical scenarios, such as surgical reconstructions, joint replacements and sleep bruxism. Furthermore the development of subject-specific models would assist treatment planning and perhaps improve clinical outcomes.

5.3 Limitations of Current Studies

The limitations of existing approaches in studying masticatory muscles are listed as follows:

- i. In the EMG approach, the intramuscular EMG may only partially record muscle activities since it may not be permissible to insert many electrodes into a target muscle. However, it is usually required to simultaneously investigate the functional activities on different locations of a target muscle or on different muscles. Moreover, it is very difficult to verify whether the EMG electrode is correctly inserted into a target muscle or a specified region of the muscle since masticatory muscles have complex anatomical structures and locations.
- ii. Measurement of muscle size change may not be always correctly related to muscle functional activities. For example, based on the previous EMG studies, we know that masseter muscles play the most important role in the max-

imum intercuspation. However, volume and length changes of the masseter muscles were not found to be significant in maximum intercuspation [66, 68]. Moreover, the changes of cross-sectional area and the thickness of the muscles are location-dependent features and very sensitive to selected locations. In addition, the non-uniform changes observed in [67] are not easily explained by muscle functional roles.

- iii. Biomechanical modeling studies provide an overview for general masticatory system, but are difficult to apply for individual analysis since the parameters in those biomechanical models could not be accurately set for each subject. In particular, the muscle property parameters, such as the force-length properties [77] and tension properties (e.g. contraction direction).

5.4 A New Focus: Muscle Deformation

Muscle is a soft tissue in which the cells contain protein filaments that slide past one another, producing a contraction that changes the form of the cell, such as length, volume, cross-sectional area and shape. Muscle tissue may be classified according to a morphological classification or a functional classification. Such as the striated and smooth muscles by morphological classification, and the voluntary and involuntary muscles by functional classification. There are generally considered to be three types of muscles in human body [78].

- Skeletal muscle: It is a striated and voluntary muscle that is anchored by tendons to bone and is used to effect skeletal movement such as locomotion and in maintaining posture.

-
- Cardiac muscle: It is a striated and involuntary muscle that connects at branching and intercalated discs, and is controlled by nerve impulses.
 - Smooth muscle: It is non striated and involuntary muscle that is found within the walls of organs and structures such as esophagus, stomach and blood vessels. Unlike skeletal muscle, is not under conscious control.

Masticatory muscles belong to the skeletal muscle, and they changes their morphologies during contracting or being stretched. In the aforementioned current studies, the changes in the muscle length, volume and cross-sectional area have been investigated by Goto et al. [66, 67, 68] and Kubo et al. [69]. However, these anatomical dimensional parameters such as length, volume, cross-sectional area and thickness may not always reflect the functional activities of masticatory muscles well. Moreover, these parameters are the physical quantities (scalars), and do not indicate the direction of the change which is significantly correlated with the muscle functional role. Based on these considerations, we focus on a new feature: 3D muscle deformation that may reflect the muscle functional activities along the entire body (global) as well as at specific anatomical part (local), and may also indicate the directions of the muscle morphological changes in global and local. Such information may be considered to be more helpful to clarify the functional roles and diagnose the medical abnormalities in human masticatory system.

5.5 A New Framework

We reviewed the four major approaches (anatomical study, EMG activity recording, measurement of muscle size change and biomechanical modeling) for studying masticatory muscles in section 5.1, and discussed their limitations in section 5.2.

In this section, we introduce a new framework (Fig. 5.2) for assessing human masticatory muscle deformation, which is a useful first-cut approximation approach and consists of four step: (i) muscle deformation capture, (ii) muscle model quantization, (iii) muscle deformation assessment and (iv) muscle deformation visualization. We first design a protocol for capturing the internal structures of masticatory muscles during mandibular movements. The target muscle morphologies before and after mandibular position changed are then reconstructed from the captured structural information and represented by point cloud. Muscle deformation is assessed by recovering region correspondences between the two sets of point cloud by the proposed GLMDTPS method. Finally, the muscle deformation field is visualized by the recovered correspondences.

5.5.1 Muscle Deformation Capture

We used a 1.5 Tesla MR scanner, Signa HDx 1.5T, General Electric, Harvey, IL, USA (T1 pulse sequence; echo time (TE): 5 ms; repetition time (TR): 11.1 ms; slice thickness: 0.7 mm; spatial resolution: 0.7 mm, 1 mm, 1 mm) to capture internal structures of masticatory muscles.

To capture the muscle deformation under a specified mandibular movement, four anatomical mandibular positions were selected to simulate jaw opening and clenching cases: (1) mandibular rest position (M0); (2) maximum intercuspation

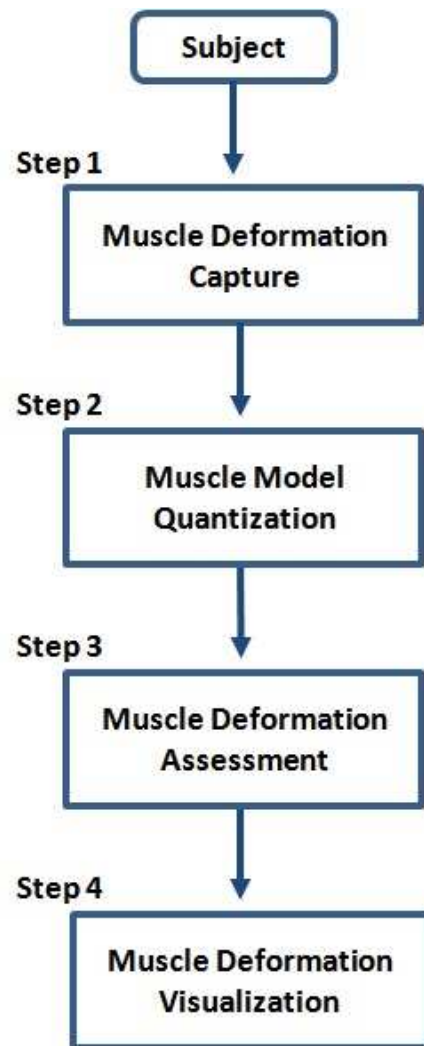


Figure 5.2: A new framework for assessing human masticatory muscle deformation.

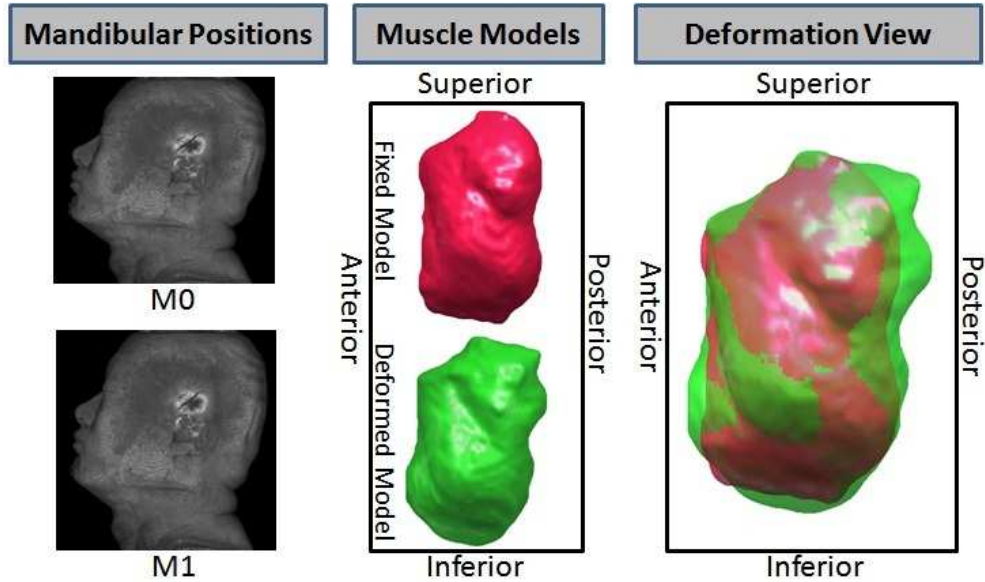


Figure 5.3: Muscle deformation capture (left side masseter muscle). The fixed and deformed models indicate the muscle morphologies before and after the mandibular position changed.

position (maximum clenching position) ; (3) medium jaw-opened position (M2) defined as the mid-position between the M0 and the maximum jaw-opened position (M3); and (4) M3 achieved by each subject's effort as the maximal vertical mouth opening without pain or discomfort. To ensure a stable posture of the mandible at M0, M2 and M3 during the MR scans, three acrylic bite props were customized for each subject. The three acrylic bite props play the role of position references for making each subject preserve the mandibular positions, but does not serve to hold the mandible for relaxing the muscles. In addition, the head position of each subject is also fixed on the scanning bed during MR scans.

After the MR scans, the three sets (M1, M2 and M3) of the whole-head MR images are registered to the set M0 as a rigid registration using MedINRIA-ImageFusion software (INRIA, France). The targeting muscles are then carefully

segmented from the four sets of MR images using a semi-automatcal segmentation technique (ITK-SNAP software). After muscle segmentations, the 3D muscle models are automatically reconstructed from these segmented MR images using MATLAB (MathWorks, U.S.A). An example of masseter muscle is shown in Fig. 5.3.

5.5.2 Muscle Model Quantization

In order to numerically describe the 3D morphology of each muscle model and recover region correspondences between the two 3D muscle models before and after the change in mandibular position (e.g., the fixed model and the deformed model as shown in Fig. 5.3), the large set of voxels in each model is partitioned into specified K groups having approximately the same number of voxels nearest to them. Each group is represented by its centroid point, and these centroid points are used to represent the 3D morphology of muscle model.

To achieve a uniform and adaptive muscle model quantization, a down-sampling method is essential. Lloyd algorithm [79] is one of the most popular methods for grouping data points into a given number of categories, used for k-means clustering. It starts by partitioning the input points into k initial sets, either at random or using some heuristic. It then calculates the average point, or centroid, of each set via some metric (usually averaging dimensions in Euclidean space). It constructs a new partition by associating each point with the closest centroid, usually using the Euclidean distance function. Then the centroids are recalculated for the new clusters, and algorithm repeated by alternate application of these two steps until convergence, which is obtained when the points no longer switch clusters

(or alternatively centroids are no longer changed).

Algorithm 3 Muscle Model Quantization Algorithm

Input: Points $P_i = (P_1, P_2, \dots, P_n)$, Number of cluster: K .

Begin I: Randomly choose the initial clusters C_K from P_n

Step1: To assign each point P_i to its corresponding cluster C_j by Lloyd algorithm.

Step2: To calculate the numbers of points in each cluster, and find the C_{max} and C_{min} clusters which have the maximum and minimum numbers of points, respectively.

Step3: Update the locations of clusters C_i where $i \neq max, min$ by the traditional Lloyd algorithm.

Step4: Update the locations of clusters C_i where $i = max, min$ by randomly picking two points within C_{max} point group, and assigning to C_{max} and C_{min} , respectively. At the last iteration, the locations of C_{max} and C_{min} are updated by the classical Lloyd algorithm.

End I: Repeat the four steps until the standard deviation of the numbers of points belong to the clusters no longer changes.

Output: Clusters C_K

However, the algorithm converges slowly (or often does not converge) and sometimes poor clusterings. To avoid these issues, we proposed an optimized Lloyd method as described in Algorithm 3 for the muscle model quantization. To test the performance of our proposed method, we down-sampled eight masseter muscle models by 2000 points. The mean performances of the proposed method and the standard Lloyd algorithm are shown in Fig. 5.4. The error denotes the standard deviation of the numbers of voxels in the voxel groups. Algorithm 3 shows accurate results and provides a uniform quantization (± 2.4 voxels in Fig. 5.4) for the muscle models.

After sampling each paired muscle models, two sets of K centroid points are obtained from the fixed model and the deformed model, respectively, and then used to recover the region correspondences between the two muscle models in

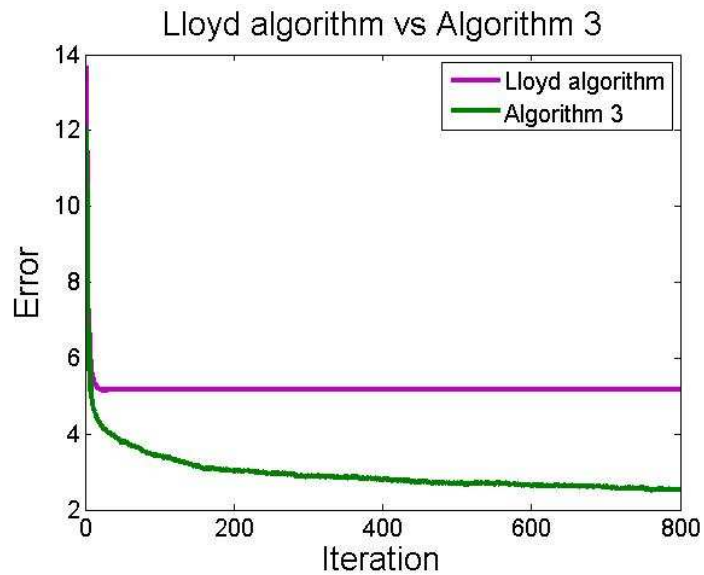


Figure 5.4: The experimental comparison between the Lloyd algorithm and Algorithm 3.

the next step. Each set of the points represents the 3D morphology of the entire muscle body. An example is given in Fig. 5.5.

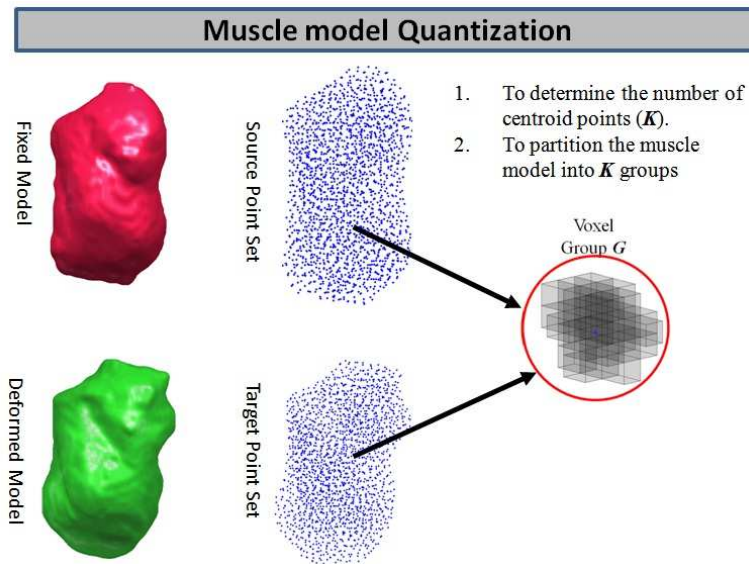


Figure 5.5: Muscle model quantization (left masseter muscle).

5.5.3 Muscle Deformation Assessment

The muscle deformation is measured by the Euclidean distances between paired corresponding points. To estimate correspondences between the two point sets, there are typically two types (iterative or non-iterative methods described in section 1.2) of non-rigid point set registration methods which can be used. Such as the aforementioned shape context method [5], TPS-RPM [16], CPD [24], GMM-REG [14] as well as our proposed GLMDTPS and GLMDGRBF methods.

Compared such methods, the shape context method is easily implemented in different programming languages, and has been applied to brain mapping [28], recovering breathing motion [32] and stomach deformation [31]. However, it is relatively difficult to achieve a good match result with a single iteration (discussed in section 1.2). In practice, the shape context method easily produces cross-mismatches [13] of neighbors (i.e. it is unable to preserve local structures during matching) when neighboring points are close to each other, and long geodesic distance mismatches [13] by minimizing the total cost using a linear assignment solution. Therefore, an extra correction step [13] is required to remove these mismatches when it is chosen for muscle deformation assessment. Moreover, TPS-RPM and GMMREG may take relatively long times to register two point sets as discussed in Section 3.4.1. In addition, although CPD may employ fast Gauss transform and low-rank matrix approximation to provide a fast solution, a tradeoff between the computational time and the matching accuracy exists must be adequately considered.

Thus, we selected the proposed GLMDTPS, which gives the best performance in the former experiments, to assess the muscle deformations in the next Chapter

6 and 7. The details of the method implementation and the parameter setting are given in section 2.3.

5.5.4 Muscle Deformation Visualization

After recovered the region correspondences between the fixed and deformed models, a set of Euclidean vectors denoting the displacements between paired corresponding points is obtained. The directions and magnitudes of the Euclidean vectors are used to describe the muscle deformation field from the fixed model to the deformed model, while the resultant direction of the set of Euclidean vectors could be used to indicate the direction of the muscle contraction (or stretching). Two examples are shown in Fig. 5.6.

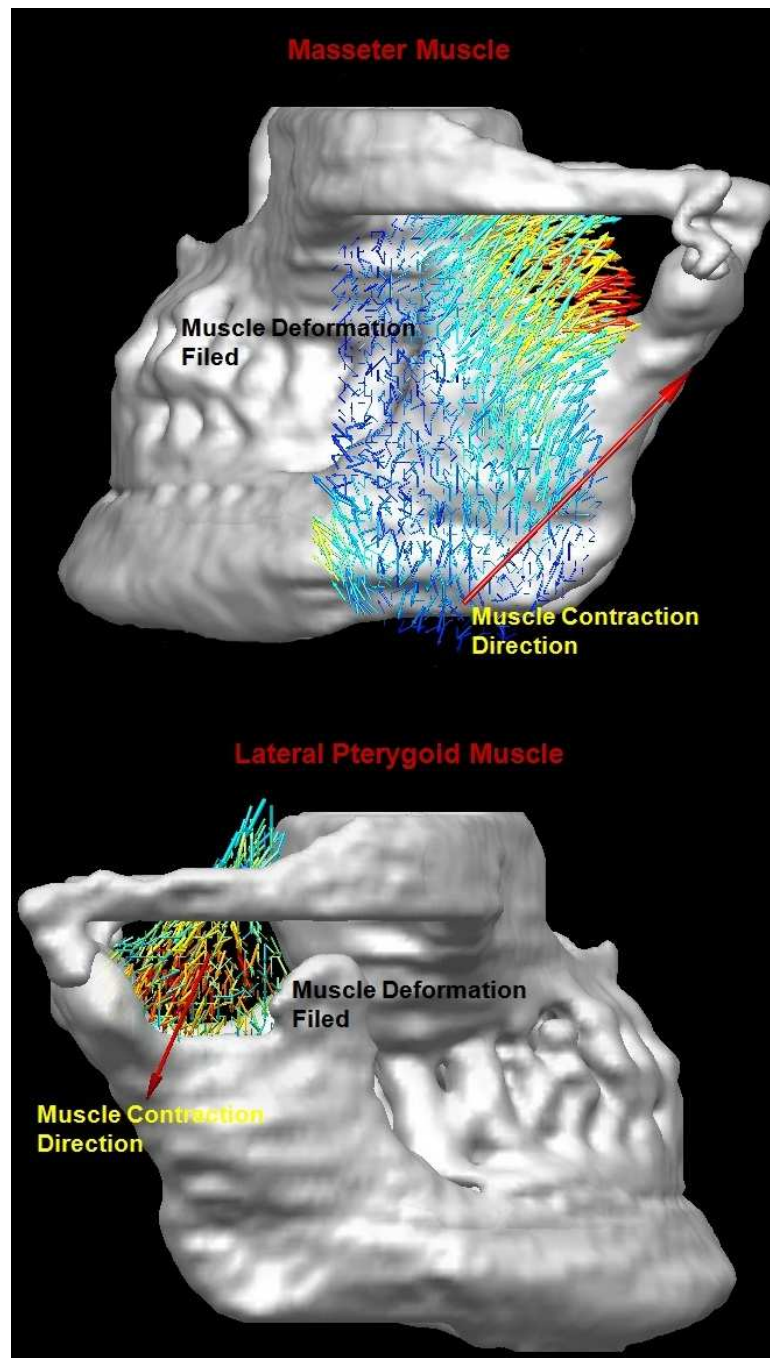


Figure 5.6: Muscle deformation visualization in a maximum intercuspation case. The top and bottom indicate the deformation fields of the masseter muscle and the lateral pterygoid muscle, respectively. The small arrows in each deformation field indicate the directions of point displacements and their colors from blue to red represent the magnitudes of point displacements from small to large. The big red arrows indicate the resultant directions of the muscle deformation fields.

Chapter 6

Application I: Masticatory Muscle Functional Activity Investigation

In this chapter, we seek to assess the deformations of the subject-specific masseter muscles and lateral pterygoid muscles during jaw opening and closing through the proposed framework, and relate the assessed muscle deformations to the muscle functional roles. The muscle deformation captures are acquired from a normal adult male subject (31 years of age, without any dental problems in clenching and jaw-opened movements) who underwent MR scans of the whole head with the mandible at the aforementioned four mandibular positions (M0, M1, M2 and M3).

6.1 Masseter Muscle

6.1.1 Research Background

The masseter muscles (MM) are known to elevate the mandible and clench the teeth. These functions are regulated by the trigeminal motor output, but are also modified by their anatomic architecture characteristics, i.e. the form. Anatomically, the masseter muscle comprises three compartments (superficial, intermediate and deep) with each compartment having one or more musculoaponeurotic layers [47, 80, 81].

McDonald and Hannam [59] showed the activities of the MM to be sensitive to the location, size, and direction of the contact point during maximal clenching tasks by EMG. The EMG activities of the superficial and deep parts were distinguished in the MM during maximal-effort intercuspal, incisal static clenches and open/close excursions by Blanksma et al. [60]. In attempts to explain the functional roles of MM, a series of recent studies employing medical imaging could only reveal how the anatomic dimensions of the MM changed with various mandibular positions. Using MRI, Goto et al. [66, 67, 68] observed quantifiable differences in muscle length change between the deep and superficial parts and the non-uniform changes in cross-sectional areas (CSAs) when the mandible moved from the intercuspal position to the maximum jaw-opened position, but found no substantive changes in muscle volume. The thicknesses of the MM, measured by the medio-lateral distances of the MM from the ultrasound images, were observed by Kubo et al. [69] to increase during tooth clenching efforts. These reported changes in the thickness and the CSAs may be explained by the contractions of muscle fibers as well as increase in volume of the circulating blood into the muscle

[70, 71].

However, as explained in section 5.3, EMG can only partially record the muscle activity and those dimensional parameters may not be able to fully reflect the functional roles of the MM when the mandible is moved from one position to another. Hence, the aims of this study are to employ the proposed new framework (in section 5.5) to assess the deformations of subject-specific MM during simulated mandibular movements, and relate the muscle deformations to their functional roles.

6.1.2 3D Reconstruction of Masseter Muscle

A total of the eight 3D muscle models (the left and right muscles at the four mandibular positions) under the four mandibular positions were reconstructed. The two muscle models before and after mandibular position changed in each case were demonstrated in the same coordinate system using different colors as Fig. 6.1 shows. The inter-rater reliability and the intra-rater reliability of the eight muscle segmentations were assessed by the comparisons of the muscle volumes between the occasions as well as the raters using the intraclass correlation coefficient (ICC) [82]. Both intra-rater reliability and inter-rater reliability of the segmentations were very high, with ICC of 0.992 and 0.987, respectively. The deformations of the MM accompanied by the changes of mandibular position were clearly seen from these reconstructed muscle models. Moreover, the differences of muscle deformations between the left and right muscles were also observed.

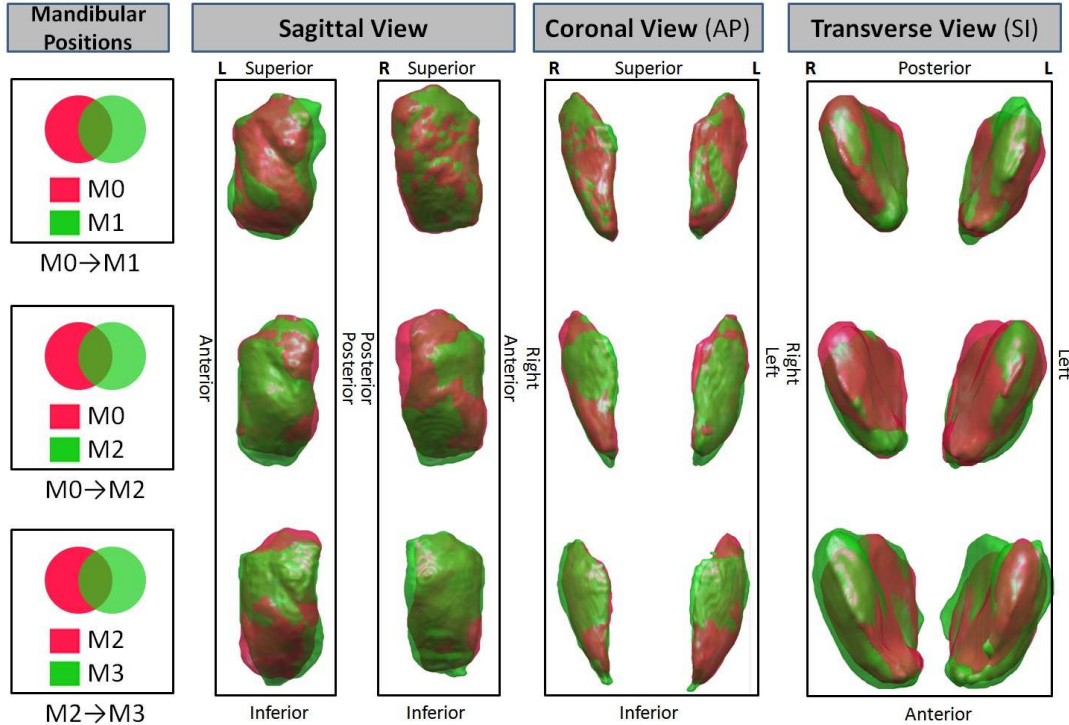


Figure 6.1: 3D reconstruction of masseter muscles. AP: from anterior to posterior; SI: from superior to inferior; L and R indicate the left and right sides, respectively

6.1.3 Validation of Registration Results

After reconstructed the eight muscle models, each muscle model was sampled by the three level point sets (800, 1400 and 2000 points) using Algorithm 3, respectively. The correspondences between the paired point sets (i.e. the fixed and deformed point sets) in each level from M0 to M1, from M0 to M2 and from M2 to M3 were then recovered using GLMDTPS.

Validating the recovered correspondences in masticatory muscle deformation is not straightforward. The lack of a ground truth complicates matters and prevents to directly assess the registration accuracy. Moreover, only few non-rigid registration validation methods were found in literature review, such as using

anatomical landmark [83], biomechanical model [84], physical phantom [85] and quantitative metrics approach [13, 28, 32]. The first three methods would not be appropriate here as there is no easily identified landmarks, applicable biomechanical modeling and physical phantom for masticatory muscles. The quantitative metrics approach employs spatial overlap (Dice coefficient [86]) or distance-based measures (symmetric mean absolute distance (SMAD) [86] and Hausdorff distance (HD) [86]) to evaluate the similarity between the registered fixed model (i.e., register whole voxels in the original fixed model onto the deformed model using a non-rigid transformation built by the recovered spatial correspondences) and the deformed model since incorrect correspondences may misguide the non-rigid transformation leading to an unacceptable transformed fixed model.

In quantitative metrics approach, SMAD and HD attempt to estimate non-rigid registration errors using the mean distance and the maximum distance between the registered fixed model and the deformed model, respectively. Dice coefficient evaluates registration error using spatial overlap between the two models. In this study, we follow the same quantitative metrics approach in [13, 28, 32], where SMAD and HD were used to validate the cortical surface, lung and animal skeleton registration results.

The validation results in the three mandibular movements ($M0 \rightarrow M1$, $M0 \rightarrow M2$ and $M2 \rightarrow M3$) are shown in Table 6.1. The SMAD and HD show accurate registration results under all the three level point sets, while the SMAD and HD are improved (i.e., the errors are reduced) by increasing the numbers of sample points from 800 to 2000. The point set registrations between the fixed model and the deformed model using 2000 points show the best results.

Table 6.1: Validation of registration results

Npnts	Parameters	1	2	3	4	5	6	Mean(STD)
800	SMAD [mm]	0.43	0.41	0.43	0.42	0.41	0.43	0.42(0.01)
	HD [mm]	3.53	3.13	4.77	2.90	2.31	3.04	3.28(0.83)
1400	SMAD [mm]	0.41	0.41	0.41	0.41	0.41	0.42	0.41(0.00)
	HD [mm]	3.01	2.24	4.10	2.39	2.05	2.86	2.78(0.74)
2000	SMAD [mm]	0.40	0.39	0.39	0.40	0.40	0.40	0.40(0.00)
	HD [mm]	2.73	2.04	3.78	2.16	1.92	2.53	2.53(0.68)

Number of points (Npnts), Symmetric mean absolute distance (SMAD), Hausdorff distance (HD). Mean (STD) are computed from the six cases of muscle deformations. 1: the left muscle $M0 \rightarrow M1$; 2: the left muscle $M0 \rightarrow M2$; 3: the left muscle $M2 \rightarrow M3$; 4: the right muscle $M0 \rightarrow M1$; 5: the right muscle $M0 \rightarrow M2$; 6: the right muscle $M2 \rightarrow M3$.

6.1.4 Muscle Deformation Fields

According to the validation results shown in Table 6.1, the assessed muscle deformations using 2000 sample points are selected to demonstrate our approach. The muscle deformation fields under the three mandibular movements are visualized in the three anatomic planes as Fig. 6.2 shows.

In the first case ($M0 \rightarrow M1$): the MM on both sides contracted superiorly (Fig. 6.2-1,2,3 and 4), but contracted in opposite directions in antero-posterior axis, i.e., the left muscle contracted posteriorly and the right muscle contracted anteriorly (Fig. 6.2-1,2,5 and 6). The deep compartment in the left muscle had the relatively larger deformation (see the color of 3D arrows in Fig. 6.2-1 and 6).

In the second case ($M0 \rightarrow M2$): the MM on both sides were stretched to inferior and anterior (Fig. 6.2-7 and 8). Meanwhile the MM were stretched to left slightly (Fig. 6.2-9 and 10). The superficial compartment in the left muscle and the deep compartment in the right muscle had the relatively larger deformations

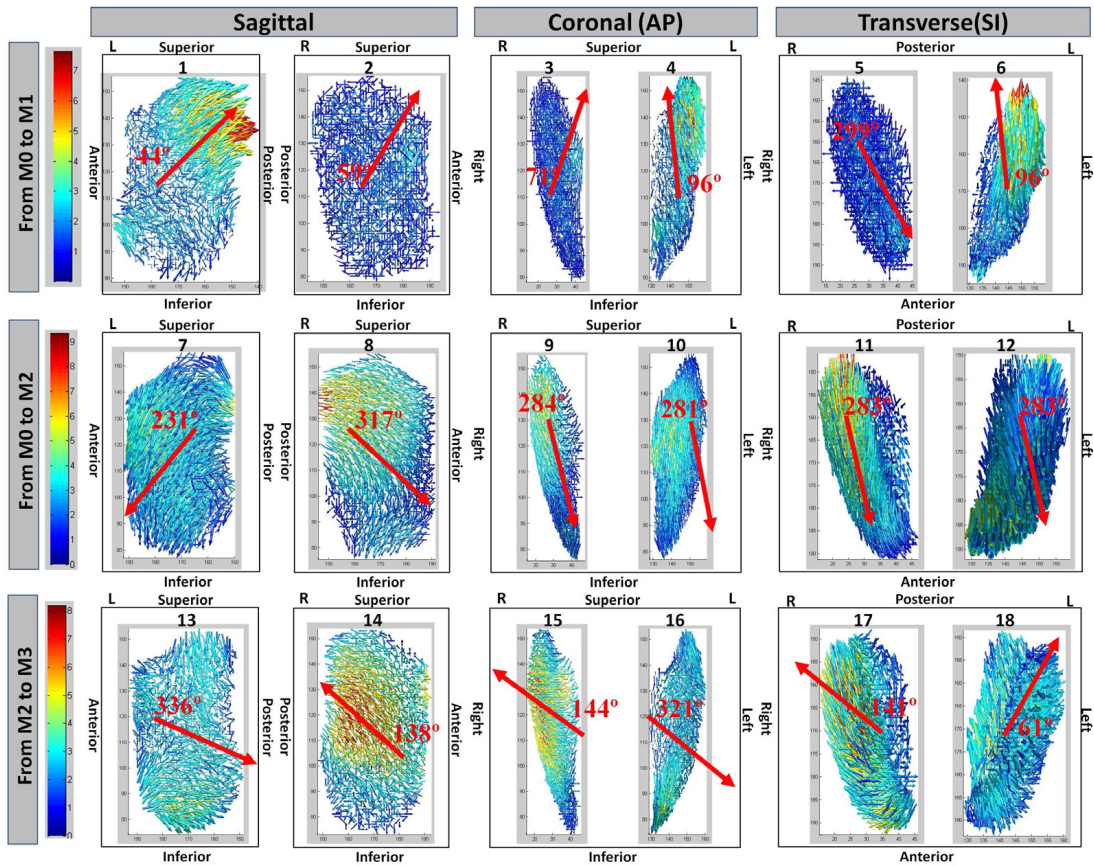


Figure 6.2: Muscle deformation fields. The direction of each point displacement is indicated by a 3D arrow (small) and shown in the three anatomic planes, respectively. The color of each 3D arrow represents the magnitude of each centroid point displacement. The 2D arrows (red) indicate the resultant directions of displacements of all points in the three planes, respectively. L: left side; R: right side; AP: from anterior to posterior; SI: from superior to inferior. These results were computed by 2000 centroid points and demonstrated using MATLAB (MathWorks, U.S.A)

(Fig. 6.2-7,8,11 and 12).

In the third case ($M2 \rightarrow M3$): the left muscle was continuously stretched to inferior and left (Fig. 6.2-13 and 16), but in antero-posterior axis, the left muscle was stretched to posterior (Fig. 6.2-13 and 18). In addition, the right muscle generated the opposite directions (Fig. 6.2-14,15 and 17) in the three planes

compared to the second case. The superficial compartments in the left and right muscles shows the relatively larger deformations (Fig. 6.2-13,14,15,16,17 and 18).

These assessed muscle deformation fields are also consistent with the observations in Fig. 6.1.

6.1.5 Discussion and Conclusion

Based on the proposed new framework, this study evaluated the functional activities of subject-specific MM under the three simulated mandibular movements through the assessed deformation fields. The significant contributions of this study include the following:

6.1.5.1 Muscle Architecture

The internal arrangements of muscle fibers have been considered to be the primary determinant of muscle function. Therefore, clarifying the internal architecture of the muscle may help to understand its functions. According to the aforementioned MRI protocol, the three compartments of the MM were distinguished in the MR images (Fig. 6.3 and 6.4). These observations are consistent with the findings by Schumacher [47] and Gaudy et al. [81], who described the three internal planes. In addition, the differences between the deformations on the deep and superficial parts of the MM caused by the different arrangements of the muscle fibers were also observed. Consequently, these assessed deformation fields effectively reflect the anatomic architectural and functional heterogeneity of the muscle compartments.

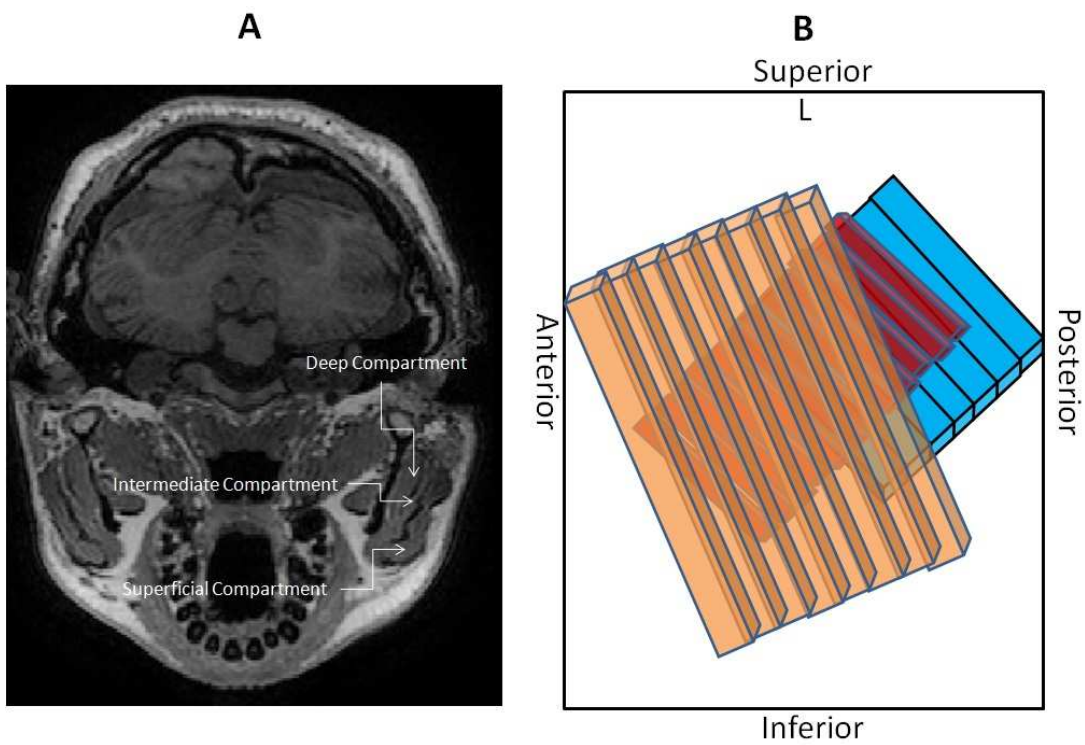


Figure 6.3: Internal architecture of masseter muscle. The left masseter muscle of the subject was used to demonstrate the internal architecture of the masseter muscle. (A) shows the internal architecture of the masseter muscle in the MR image. (B) shows the generalized model of the muscle internal architecture in the sagittal plane: the superficial compartment (yellow), the intermediate compartment (red) and the deep compartment (blue).

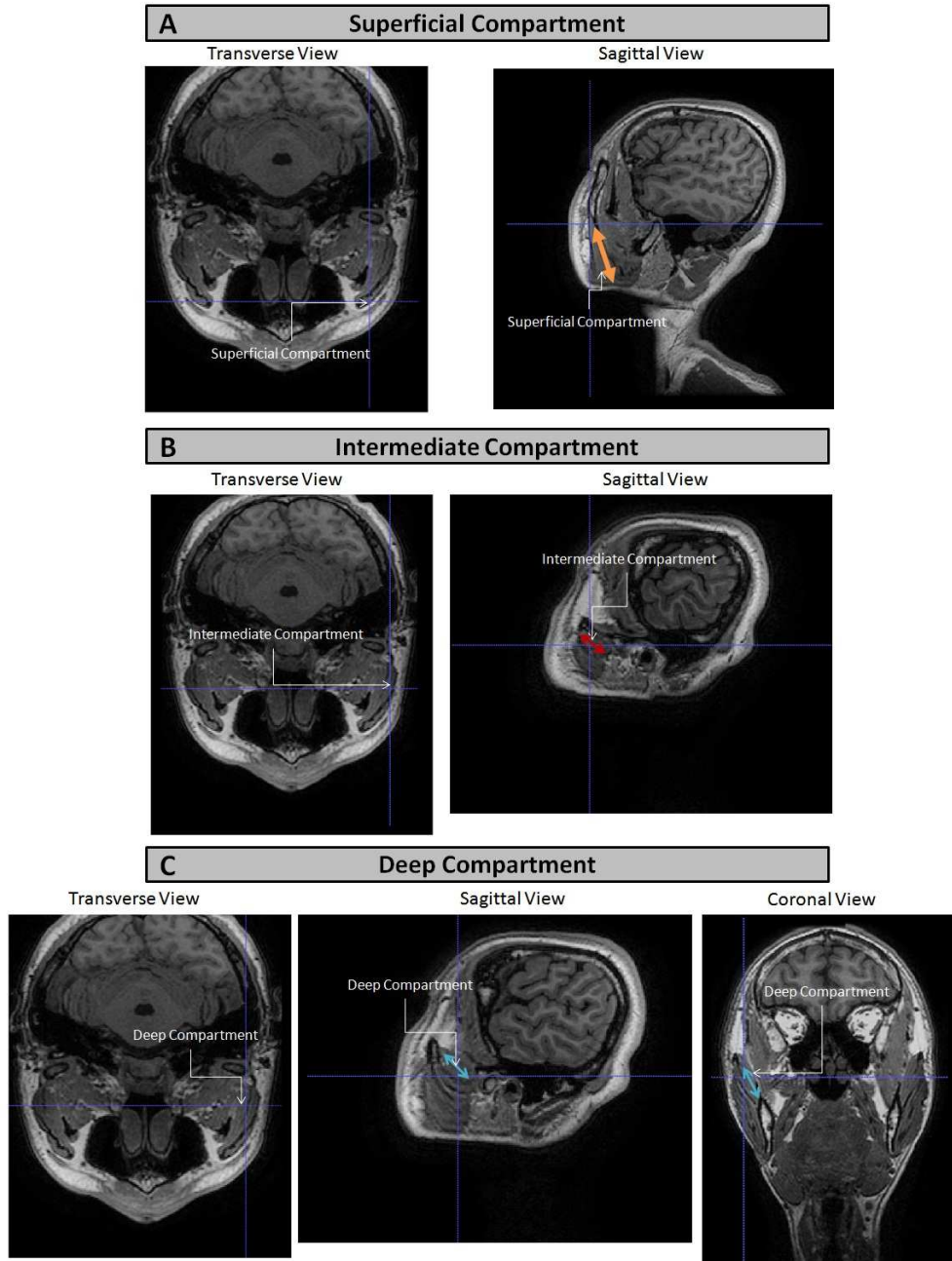


Figure 6.4: Internal architecture of masseter compartments. (A) shows the region of the superficial compartment in the transverse and sagittal view, respectively. (B) shows the region of the intermediate compartment in the transverse and sagittal view, respectively. (C) shows the region of the deep compartment in the transverse, sagittal and coronal view, respectively. The yellow, red and blue arrows in (A), (B) and (C) indicate the major arrangements of musculoaponeurotic layers, respectively.

6.1.5.2 Muscle Function

- **Muscle Functional Activity:** This study reveals that the resultant directions of the muscle deformations in the three planes meaningfully indicated the muscle contractions in the maximum intercuspation. Moreover, it also assessed and visualized the functional activities along the entire body and at specific compartments of the MM using the measured deformation fields. In addition, the functional roles of the muscle compartments may be evaluated using the assessed deformations. For example, the deep part of the left muscle showed the large deformation (Fig. 6.2-1), and the resultant direction in antero-posterior axis towards posterior (Fig. 6.2-1 and 6). Thereby the deep compartment of the subject could be considered to be the primary determinant of the muscle posterior contraction during the maximum intercuspation. Our study strongly suggests that the contractions of the left and right muscles in the opposite directions in antero-posterior axis (Fig. 6.2-1,2,5 and 6), were a result of differentials in the magnitudes of the deformations in the superficial and deep compartments of the MM as well as in the internal muscle fiber arrangements (Fig. 6.3-B). On these bases, we hypothesized that the superficial and deep compartments may directly control the movements of mandible in the anterior and posterior directions, respectively. A simple palpation trial was designed to test, and confirmed this hypothesis (Fig. 6.5). This confirmation is also corroborated by previous studies which described the interactions between musculoaponeurotic layers may affect the contraction direction in the maximum intercuspation [87, 88].

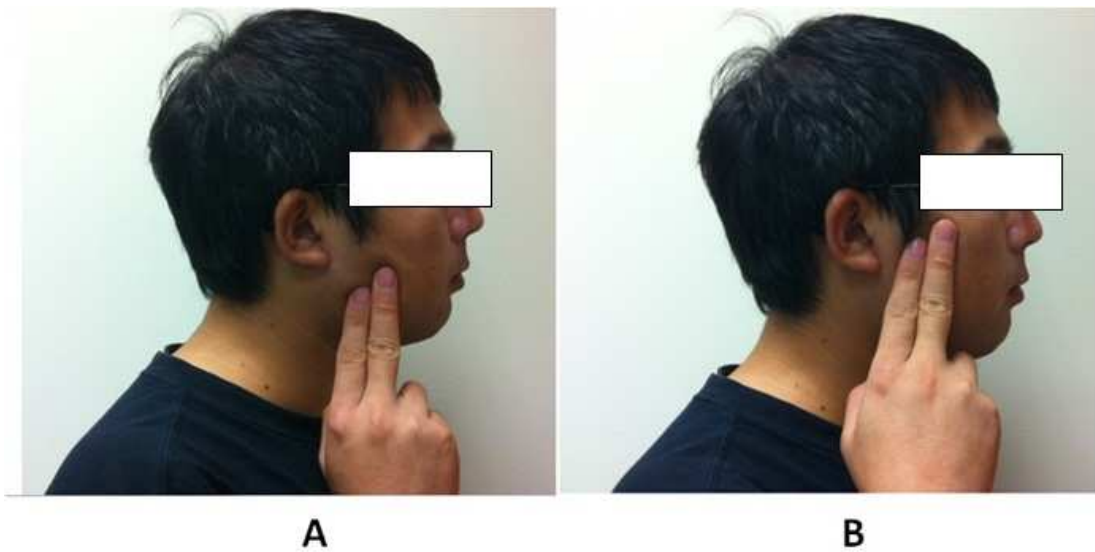


Figure 6.5: A simple palpation test. The palpation test is designed to explain the different functional roles of deep and superficial compartments. At first, slightly clench your jaw and gently touch the lower surface region of your face as shown in A. If you try to move the mandible to anterior slightly, you may detect only around the touched region bulging out. However, if you try to move the mandible to posterior slightly, only the upper and posterior region of the masseter muscle can be detected to bulge out. These palpation trials confirm that the superficial and deep compartments can directly control the mandibular movement in the anterior and posterior directions, respectively.

-
- **Muscle Contraction Direction:** The muscle components in biomechanical models of the human masticatory system [89, 90] were designed with a single-line, and positioned according to published attachment coordinates previously described by Baron and Debussy [91]. These models provide the insight into physical relationships between the mandible and the muscles. To apply these biomechanical models to a subject-specific study, the individual parameters, which are difficult to be directly measured, such as the contraction directions of the MM, have to be determined. This study relates the the muscle deformation to the muscle contraction. The direction of the muscle active contraction (during the maximum intercuspation) can be considered to be the resultant direction of the muscle deformation field, and the passive tension (during the simulated jaw-opened movements) can be indicated by its opposite direction.

This study appropriately and meaningfully describes the functional activities of the MM using the assessed deformation of the subject-specific MM. The exact functional roles of the entire muscle and the specific compartments can also be effectively evaluated by this study. This present study assessed and visualized the nature and site-specific morphologic changes of the MM at various mandibular positions, which could not be identified by the techniques described in previously published works. We believe that future studies with larger samples would help to further relate muscle deformation to the muscle contraction and the metabolic activities for evaluating masticatory muscle efficiency before and after orthodontic treatment, thereby facilitating diagnosis and management of masticatory muscle dysfunction. Meanwhile the calculated contraction directions of the patient-specific MM would assist in making proper diagnoses and treatment

plans including designing of the appliances to reconstruct the optimum occlusion of teeth by orthodontic as well as restorative means.

6.2 Lateral Pterygoid Muscle

6.2.1 Research Background

Studies of functional activities of lateral pterygoid muscles (LPM) have an important bearing on two clinical situations which are (i) to clarify the functional roles of LPM in mastication and (ii) to explain the problems associated with temporomandibular joint (TMJ) [92, 93]. The electromyographic approach (EMG) for the studies of LPM has been widely accepted. For example, Gibbs et al [61] and Wood et al [62] revealed that the inferior head and superior head of LPM have different functional roles during jaw-closing and jaw-opening. However Hannam and McMillan [63] and Ruangsri et al [64] have suggested that the two heads of LPM should be regarded as a single muscle. The major reason for the differing conclusions was the inability of previous studies to verify whether the EMG recording electrodes were correctly located within the muscle, as suggested by Murray et al [94]. Moreover, Hiraba et al [95] suggested that the superior head controlled the angular relationship between the articular disk and the condyle. On the other hand, a series of recent studies employing medical imaging [67, 68] attempted to explain the functional roles of the LPM using the dimensional parameters such as the changes in muscle volume, length and cross-sectional areas (CSAs) when the mandible is moved from the intercuspal position to the maximum jaw-opened position. Although the EMG approach promoted a large number of investiga-

tions in the functional roles of the LPM as used often in mastication and in TMJ function studies, the normal functional roles of LPM in mastication remain unclear. Presently, the recorded EMG activities may only be used to partially describe the relationship between the EMG activities of LPM and the TMJ movements. Studies using the dimensional parameters of muscle may not fully reflect the functional roles of the LPM. Hence, the aims of this study are to employ the proposed new framework (in section 5.5) to assess and visualize the deformations of subject-specific LPM in simulated jaw-opening movements, and to relate the assessed deformations of the LPM to their functional roles for the studies in mastication and TMJ function.

6.2.2 3D Reconstruction of Lateral Pterygoid Muscle

A total of six 3D muscle models (the left and right muscles at M0, M2 and M3) under the three mandibular positions were reconstructed. The two muscle models before and after mandibular position changed in each case were demonstrated in the same coordinate system by different colors as Fig. 6.6 shows. The intra-rater reliability and inter-rater reliability of the segmentations of the six muscles were very high, with ICC of 0.990 and 0.982, respectively. The deformations of the LPM accompanied by the changes of mandibular position were clearly seen from these reconstructed muscle models. Moreover, the differences of the deformations between the left and right muscles were also observed.

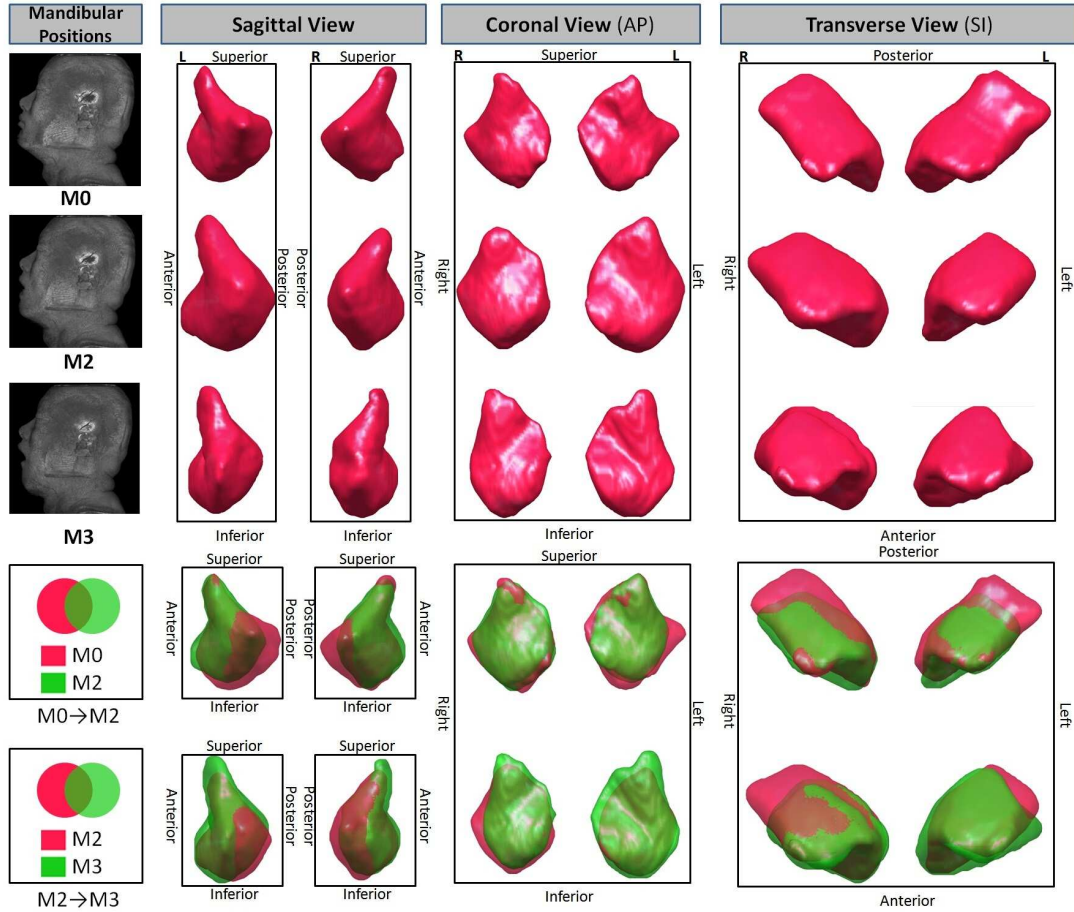


Figure 6.6: 3D reconstruction of lateral pterygoid muscles. M0: mandibular rest position; M2: medium jaw-opened position; M3: maximum jaw-opened position; AP: from anterior to posterior; SI: from superior to inferior; 'L' and 'R' indicate the left and right sides, respectively.

6.2.3 Validation of Registration Results

The same validation approach as used in section 6.1.3 was employed in this study. The validation results in the two mandibular movements ($M0 \rightarrow M2$ and $M2 \rightarrow M3$) are shown in Table 6.1. The SMAD and HD show accurate registration results under all the three level point sets, while the error are reduced by increasing the numbers of sample points from 800 to 2000. The point

set registrations between the fixed model and the deformed model show the best results in 2000 points.

Table 6.2: Validation of the proposed method

Npnts	Parameters	1	2	3	4	Mean(STD)
800	SMAD [mm]	0.42	0.41	0.42	0.39	0.40(0.01)
	HD [mm]	1.78	2.30	2.96	2.64	2.27(0.46)
1400	SMAD [mm]	0.41	0.40	0.40	0.37	0.39(0.01)
	HD [mm]	1.66	1.61	2.22	1.89	1.79(0.23)
2000	SMAD [mm]	0.39	0.39	0.38	0.36	0.37(0.01)
	HD [mm]	1.42	1.49	2.11	1.88	1.76(0.37)

Number of points (Npnts), Hausdorff distance (HD), Symmetric mean absolute distance (SMAD), Mean (standard deviation) as computed from the six cases of muscle deformations. 1: the left muscle $M0 \rightarrow M2$; 2: the left muscle $M0 \rightarrow M2$; 3: the left muscle $M2 \rightarrow M3$; 4: the right muscle $M2 \rightarrow M3$.

6.2.4 Muscle Deformation Fields

According to the validation results in Table 6.2, 2000 sample points were employed to assess the deformations of the LPM in this study. The assessed 3D deformation fields of the LPM are shown in the three anatomic planes in Fig. 6.7.

In the first case ($M0 \rightarrow M2$): the LPM on both sides contracted anteriorly and superiorly (Fig. 6.7-1 and 2) in the sagittal plane; in the coronal plane, the LPM on both sides contracted to superior and medial (Fig. 6.7-3 and 4); in the transverse plane, the LPM on both sides contracted to anterior and medial (Fig. 6.7-5 and 6). Compared with the superior heads and the origin parts, the inferior heads and the insertion parts on both sides show relatively large deformations.

In the second case ($M1 \rightarrow M2$): in the sagittal plane, the LPM kept con-

tracting anteriorly and superiorly (Fig. 6.7-7 and 8); in the coronal plane, the LPM kept contracting to superior and medial (Fig. 6.7-9 and 10); in the transverse plane, the LPM kept contracting to anterior and medial (Fig. 6.7-11 and 12). The insertion parts shows relatively large deformations on both sides, and the right muscle generally shows relatively large deformation than the left muscle. Compared with the deformations of the superior heads in the first case, the superior heads on both sides in the second case show larger deformations.

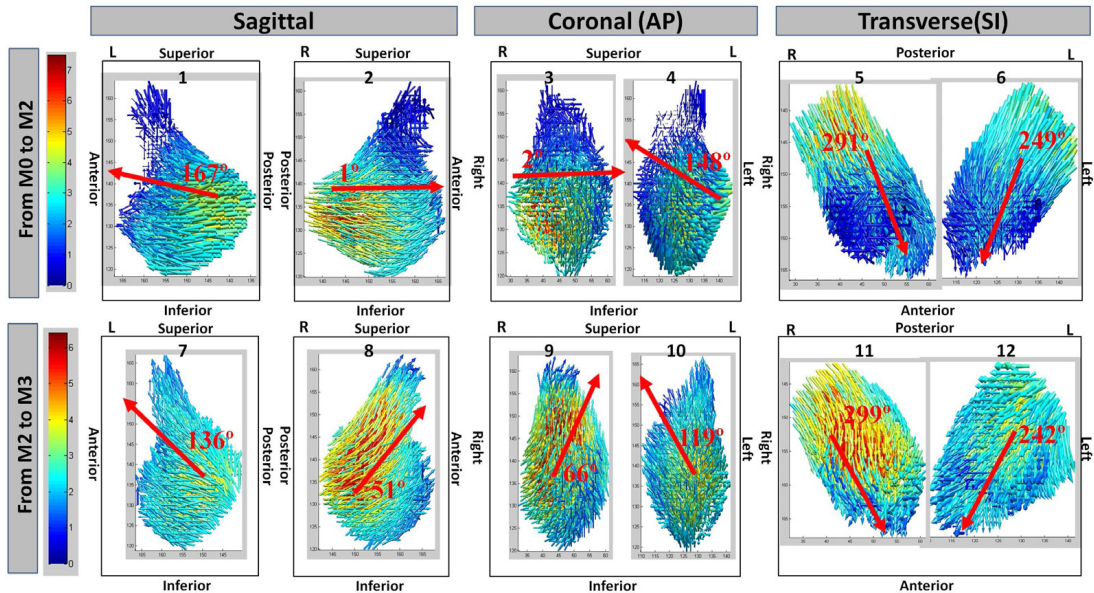


Figure 6.7: Muscle deformation fields. The direction of each point displacement is indicated by a 3D arrow (small) and shown in the three anatomic planes, respectively. The color of each 3D arrow represents the magnitude of each centroid point displacement. The 2D arrows (red) indicate the resultant directions of displacements of all points in the three planes, respectively. L: left side; R: right side; AP: from anterior to posterior; SI: from superior to inferior. These results were computed by 2000 centroid points and demonstrated using MATLAB (MathWorks, U.S.A)

6.2.5 Discussion and Conclusion

Based on our proposed new approach, this study evaluated the functional activities of subject-specific LPM under the two simulated mandibular movements using the assessed deformation fields. The significant contributions of this study include the following

6.2.5.1 Muscle Functional Activity

This study assessed and visualized the subject-specific muscle activities along the entire body as well as at specific anatomical compartments (e.g. the small 3D arrows in the superior heads and the inferior heads) of the muscles in the simulated mandibular movements using the assessed deformation fields of the LPM. Furthermore, the resultant direction of the deformation field for each muscle may indicate the direction of the muscle active tension that determined the mandibular movement and the TMJ movement during jaw opening.

6.2.5.2 Functional Roles in Mastication

Most published studies employed EMG activity to identify whether the LPM functionally work during a specific mandibular movement. The present study attempts to explain how the muscles control the mandibular movements in mastication by investigating the biomechanical relationship between LPM and mandibular movements as a clinically relevant approach to understanding the functional role of specific muscles. According to the assessed deformations of the LPM (Fig. 6.7), it was found that the LPM on both sides contracted anteriorly and superiorly during the jaw opening. In other words, a pair of active muscle tensions

was produced bilaterally and applied at the insertions of the left and right muscles, respectively, as shown in Fig. 6.7. Moreover, the directions of the muscle tensions at the insertions may be indicated by the resultant directions of the deformation fields. Such as the calculated 167° on the left side and the 1° on the right side in the sagittal plane (Fig. 6.7-1 and 2); the 148° on the left side and the 2° on the right side in the coronal plane (Fig. 6.7-3 and 4); the 249° on the left side and the 291° on the right side in the transverse plane (Fig. 6.7-5 and 6). Consequently, the mandible of the subject was passively depressed by such biomechanical relationships. In addition, the LPM were observed to change their contraction directions in the second case (i.e. contracted more superiorly in Fig. 6.7). These changes may reflect the functional role of the LPM in the controlling of muscle contraction direction for the various mandibular positions.

6.2.5.3 Functional Roles in Temporomandibular Joint Function

Anatomically, the superior head and the inferior head of LPM insert onto the articular disk and the condylar neck, respectively. Moreover Hiraba et al [95] found that the superior head functioned to stabilize the condyle against the biting force that pulls the condyle posteriorly, and controlled the angular relationship between the articular disk and the condyle. In this study, the insertions of the LPM may be clearly identified in the MR images as Fig. 6.8 shows, and the condylar movements and the positional changes of the articular disk may also be seen in Fig. 6.8. These observations provide the basis of biomechanical analysis for the subject-specific TMJ movements. Furthermore, the active tensions of the LPM which were indicated by the assessed deformations of the LPM, can be used to further explain the condylar movements and the positional change of the

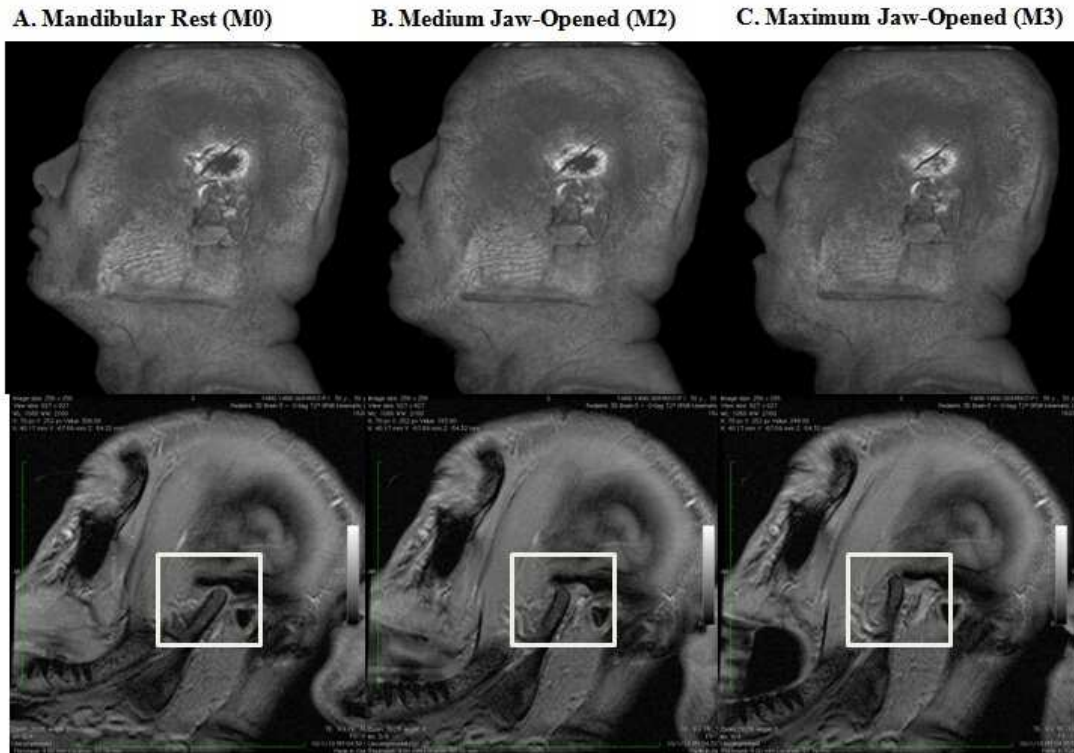


Figure 6.8: Temporomandibular joint movement. (A) (B) and (C) show the left temporomandibular joint and the insertion of the left lateral pterygoid muscle under the mandibular rest position, the medium jaw-opened position and the maximum jaw-opened position, respectively.)

articular disk.

This study appropriately and meaningfully describes the anatomic architectural and biomechanical characteristics of the subject-specific LPM using the assessed deformation fields of the subject-specific LPM. We believe that future studies with larger samples would be helpful to clarify the functional roles of the superior and inferior heads of LPM, and further explain the functional roles of LPM in mastication and TMJ functions. Furthermore this study could possibly be used to identify the aetiology of temporomandibular joint disorder (TMJD) for different individuals.

Chapter 7

Application II: Biomechanical Relationship between Muscle Activities and Mandibular Movements

In this chapter, we seek to explain the biomechanical relationship between masticatory muscle activities and mandibular movements through assessing the muscle deformations and measuring the mandibular movements by MR images.

7.1 Research Background

As described in Chapter 5, masticatory muscles are classified into four groups: masseter muscles (MM), medial pterygoid muscles (MPM), lateral pterygoid muscles (LPM) and temporal muscles (TM). The four muscle groups work together

to control the elevation and depression of the mandible for our daily mastication, i.e., the mandibular functions. The electromyographic approach (EMG) [59] and biomechanical modelling [90] have been used for studying the relationship between the mandibular functions and the masticatory muscle activities. Muscle activities during the mandibular movements were recorded to correlate with the mandibular functions. Although the physiological activities recorded by EMG reflect the muscle functional activities, how the muscles work together to achieve the mandibular functions, i.e. the biomechanical relationship, could not be explained by the EMG activities. In addition, the biomechanical relationship has been suggested to be more important for clinical practice, such as the diagnosis and treatment of masticatory muscle dysfunction and temporomandibular joint disorder (TMJD). However, the biomechanical modellings in previous studies have been difficult to be employed for the subject-specific case due to the problem of directly measuring parameters, such as muscle tension direction and magnitude in vivo. The aims of this study are to assess subject-specific mandibular movement and muscle deformations in maximum intercuspation, and to explain the mandibular functions in maximum intercuspation using the assessed muscle deformations for a subject.

7.2 Image Data Acquisition

The data acquisition technique (described in section 5.5.1) was used to capture the internal structures of masticatory muscles at the mandibular rest position (M0) and the maximum intercuspation position (M1) for a normal adult male subject (31 years of age, without any dental problems in clenching and jaw opening

movements).

7.3 Estimation of Masticatory Muscle Tensions

Each masticatory muscle tension (active or passive tension), when the mandible was moved from the M0 to the M1, was estimated as follows

7.3.1 3D Reconstruction of Masticatory Muscles

At first, each muscle of the subject was semi-automatically segmented from the two sets of the original MR images by ITK-SNAP software [96]. After the segmentations, a radiologist analyzed and adjusted the anatomic boundaries of the muscle for the anatomic accuracy, and the 3D muscle models of the M0 and M1 positions were reconstructed from these anatomically revised MR images. The inter-rater reliability and the intra-rater reliability of the sixteen muscle segmentations (the left and right muscles at the two mandibular positions) were assessed by the comparisons of the muscle volumes between occasions and between raters using the intraclass correlation coefficient (ICC) as described in [82].

7.3.2 Muscle Model Quantization

To numerically describe the 3D morphology of each muscle model and compute region correspondences between the two 3D muscle models (i.e., the M0 model and the M1 model) before and after mandibular position changed, the large set of voxels in each model was partitioned into specific K groups having approximately the same number of voxels nearest to them, and each group was represented by its centroid point using the Algorithm 3 introduced in section 5.5.2.

7.3.3 Recovering Region Correspondences

The proposed GLMDTPS method was used to estimate the region correspondences between the M0 and M1 models. After finding the correspondences, each muscle deformation was measured by the directions and magnitudes of the set of Euclidean vectors, which denote the displacements between pairs of corresponding points.

7.3.4 Muscle Tension Estimation

- **Direction:** In this study, the direction of muscle active tension is estimated as the resultant direction of displacements of all sample points within each muscle model, and is calculated by $\sum_{n=1}^K \vec{d}_n / |\sum_{n=1}^K \vec{d}_n|$ for each muscle. K is the number of sample points and \vec{d}_n is the displacement of n^{th} sample point.
- **Magnitude:** The magnitude of each muscle tension may not be able to be directly measured by current techniques. However, the degree of the muscle deformation and its elastic properties may be used to estimate the muscle tension. In this study, the magnitude of each muscle tension is estimated by

$$M = \left\| \sum_{n=1}^K \vec{d}_n \right\| \times PFI \quad (7.1)$$

where the term $\left\| \sum_{n=1}^K \vec{d}_n \right\|$ is the resultant displacement of all sample points for each muscle, and it can describe the degree of muscle deformation since its origin is fixed during mandibular movements. PFI [97] (Priority for Force Index) is an index expressing the maximal force of muscle per unit

volume under the same amount of maximal work. It is defined by

$$PFI = PCS/V^{\frac{2}{3}} \quad (7.2)$$

where PCS is the physiological cross-sectional area which was defined as V/FL (FL: average fiber bundle length), and V is the muscle volume. The PFI for human masticatory muscles have been investigated by van Eijden et al., [98, 99, 100] as Table 7.1 shows. In order to estimate the magnitudes of

Table 7.1: Priority for force index of the jaw-closing and jaw-opening muscles

Point Set	MM	MPM	LPM	TM
PFI	1.39	1.53	0.91	1.24

muscle tensions for the four group muscles by (7.1), the sample points in the four muscle groups (MM, MPM, LPM and TM) in the initial condition M0 were assumed to represent the volumes with approximately the same size. i.e., when we sampling the muscle models, the number of sample points in the four group muscles should be based on the following constraint

$$\frac{V_{MM}}{K_{MM}} \approx \frac{V_{MPM}}{K_{MPM}} \approx \frac{V_{LPM}}{K_{LPM}} \approx \frac{V_{TM}}{K_{TM}} \quad (7.3)$$

where V is the muscle volume and K is the number of sample points.

7.3.5 Measurement of Subject-specific Mandibular Movement

The mental protuberance of the mandible was suggested to be a landmark for measuring the mandibular movement since it could be clearly identified in the MR images from the coronal plane as shown in Fig. 7.1 a. Thereby, the mental protuberance was segmented from the two sets of MR images using the same approach with the muscle segmentation (Fig. 7.1 b).

a. Mental protuberance region b. Position change of mental protuberance

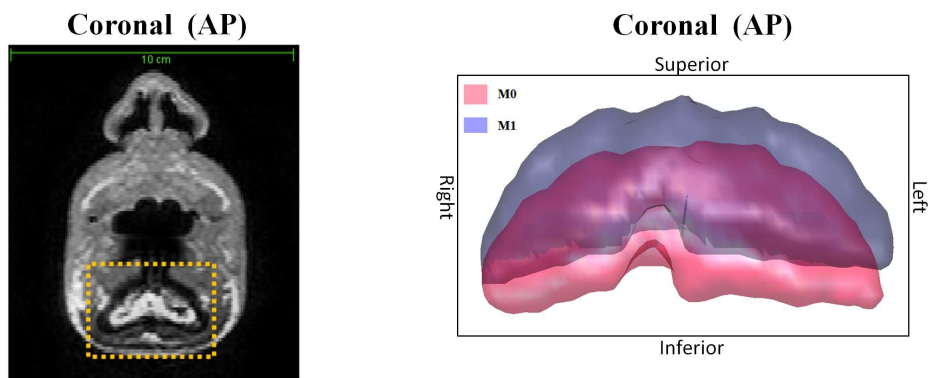


Figure 7.1: Measurement of subject-specific mandibular movement

7.4 Experimental Results

7.4.1 3D Reconstruction of masticatory muscles

A total of sixteen 3D muscle models under the two mandibular positions were reconstructed and shown in Fig. 7.2. The intra-rater reliability and inter-rater reliability of the segmentations of the sixteen muscles were high, with ICC of 0.980 and 0.960, respectively. For each muscle, the two models before and after

mandibular position changed were demonstrated in the same coordinate system by different colors for observing the morphologic changes. The deformations of the masticatory muscles accompanied by the changes of mandibular position were clearly seen from these reconstructed muscle models, moreover the differentials of the morphologic changes between the left and right muscles were also observed.

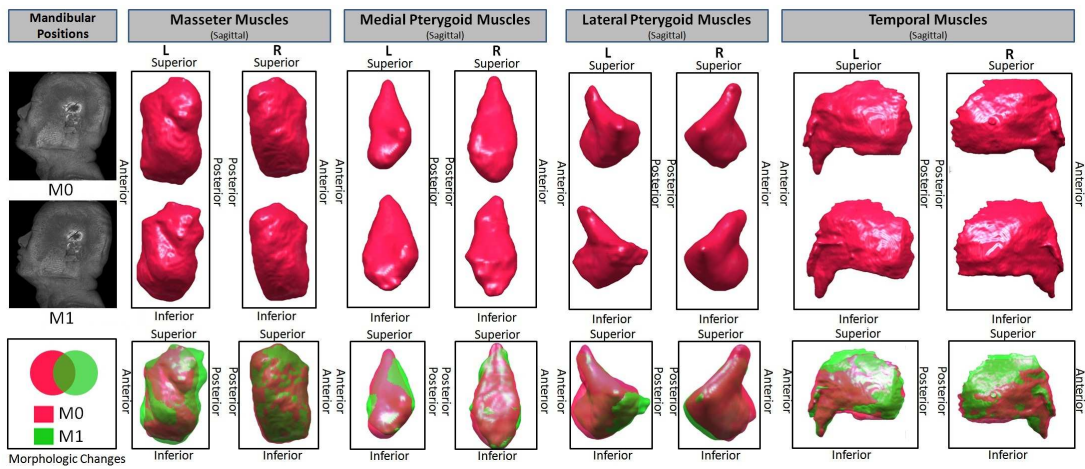


Figure 7.2: 3D reconstruction of masticatory muscles

7.4.2 Validation of Registration Results

The same quantitative metrics approach used in section 6.1.3 was employed in this study, while the determined numbers of sample points for the four group muscles were followed the constraint (7.3). Table 7.2 shows the determined numbers of sample points under different unit volumes. Table 7.3 shows the validation results using different numbers of sample points. By reducing the unit volume size for the four group muscles, the global errors in terms of SMAD and HD were reduced, respectively. Moreover, the local error between the locations of its recovered corresponding point and its physically exact corresponding point could also be

reduced by increasing the numbers of sample points for the four group muscles. The point set registrations using K3 points show the best results.

Table 7.2: Number of sample points. V: volume. K1 K2 and K3 indicate the required numbers of sample points for each muscle at M0 under the unit volumes 5 mm^3 , 4 mm^3 and 3 mm^3 .

	Volume (cm^3)		K1 (5 mm^3)		K2 (4 mm^3)		K3 (3 mm^3)	
	L	R	L	R	L	R	L	R
MM	53.15	55.24	425	442	830	863	1969	2047
MPM	15.78	15.10	126	121	247	236	584	559
LPM	17.29	15.79	138	126	270	247	640	584
TM	98.09	100.31	785	802	1533	1567	3633	3715

Table 7.3: Validation results under different numbers of sample points.

		K1		K2		K3	
		SMAD	HD	SMAD	HD	SMAD	HD
MM	L	0.50	3.86	0.43	3.34	0.40	2.54
	R	0.49	3.72	0.42	3.21	0.39	2.36
MPM	L	0.55	3.35	0.40	2.68	0.39	2.04
	R	0.56	3.34	0.42	2.73	0.41	2.15
LPM	L	0.54	3.36	0.41	2.40	0.39	1.88
	R	0.55	3.92	0.41	3.02	0.38	2.05
TM	L	0.64	4.28	0.62	4.03	0.57	3.54
	R	0.65	4.32	0.63	4.07	0.58	3.66

7.4.3 Relationship between Mandibular Movement and Masticatory Muscle Tensions

The measured mandibular movement and the estimated muscle tensions by K3 (Table 7.3) were decomposed into the three anatomic planes and shown in Fig. 7.3.

Compared with the MPM, the TM and MM generated larger muscle tensions for clenching the jaw. In Fig. 7.3 a and b, the mandible was moved superiorly and slightly anteriorly (e.g., Left: D: 94°, M: 3.30 mm). According to the estimated values of muscle tensions, this movement was caused by the three closing muscle groups (MM(L and R), MPM(L and R) and TM(L and R)), which produced the upward tensions to make the mandible rotate about the horizontal axis as a hinge movement. The LPM (LPM(L) and LPM(R)) during the maximum intercuspation were passively stretched by the condyle heads, and hence the LPM were considered to produce a pair of the passive muscle tensions, which only played a role in maintaining the mandibular posture.

In Fig. 7.3 c, the mandible was moved superiorly and slightly to the left side (D: 82°, M: 3.32 mm). The upward movement of the mandible could be explained as the aforementioned hinge movement, whereas the slight left movement was due to the unbalanced forces on the left and right sides of the mandible. i.e., the horizontal resultant force on the left side mandible was bigger than the horizontal resultant force on the right side. Moreover, although the muscle tensions on both sides pulled the mandible superiorly, the vertical resultant force on the right side was bigger than the vertical resultant force on the left side. Thus, the mandible was slightly rotated to the left side about the antero-posterior axis.

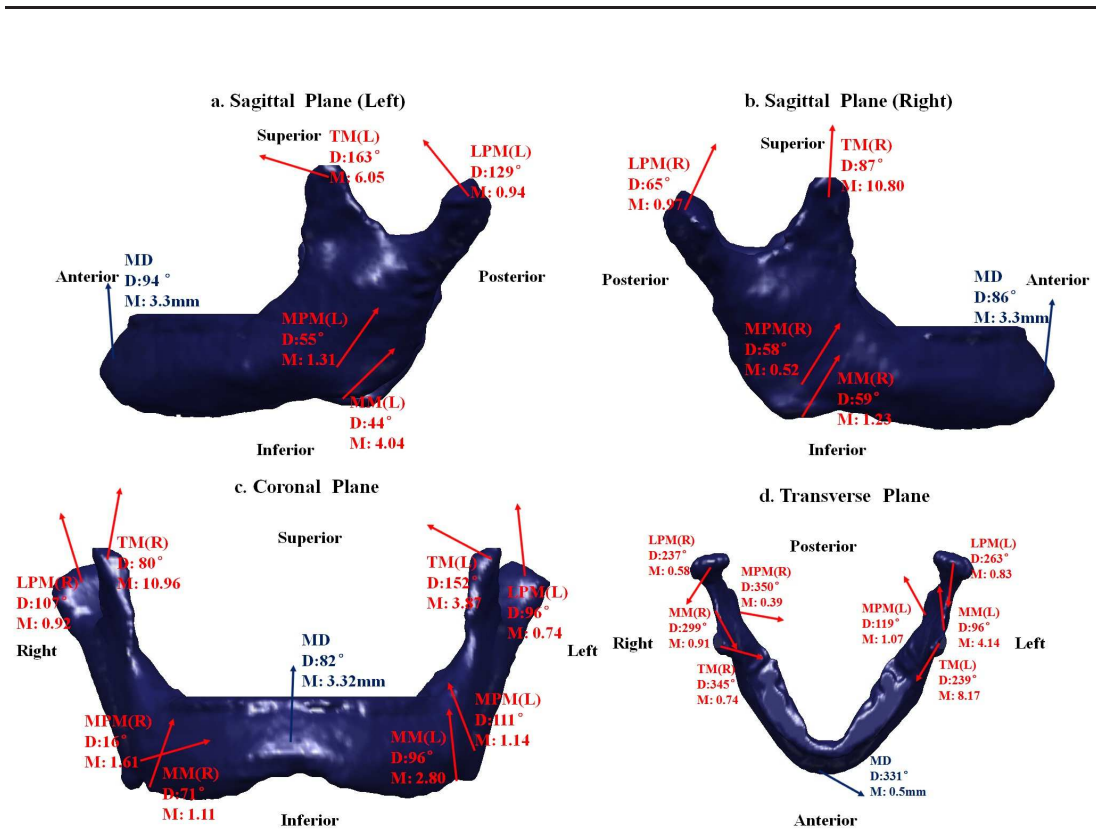


Figure 7.3: Biomechanical relationship between mandibular movement and masticatory muscle activities. MD: mandible, MM (L or R): the left or right masseter muscles. MPM (L or R): the left or right medial pterygoid muscle. LPM (L or R): the left or right lateral pterygoid muscle. TM (L or R): the left or right temporal muscle. D: the estimated direction of muscle tension (0° - 360°), M: the estimated magnitude of muscle tension ($\times 10^3$). For MD, D is the direction of the displacement (0° - 360°) and M is the magnitude of the displacement (mm). The locations of the muscle tensions were anatomically determined by their insertions from the MR images. In order to clearly see the muscle tensions of the MPM(L) and MPM(R), the arrows were positioned on the lateral surface of the mandible in a, b and c (in fact, the MPM were inserted into the medial surface of the mandible). These results were calculated according to the numbers of sample points in K3.

In Fig. 7.3 d, the mandible was slightly moved to the anterior and the left side. The anterior movement was caused by the hinge movement, and the leftward movement was mainly related to the aforementioned rotation about the antero-posterior axis.

7.5 Discussion and Conclusion

The mandibular movement and the masticatory muscles tensions of the subject were accurately assessed, and the subject-specific biomechanical relationship between the mandibular movement and the muscle tensions were explained. The present approach helps to explain the biomechanics of the anatomically and functionally complex masticatory system, and would assist in making proper diagnosis and treatment for masticatory muscle dysfunction. Furthermore, as the demonstrated results, the mandibular movement of the subject was not perfect vertical due to the unbalanced force relations (shown in Fig. 7.3 c and d), thereby such findings would be helpful to study the mastication efficiency [101], the development of the dental occlusion [102] and the reconstruction of the optimum occlusion of the subject.

Chapter 8

Conclusion and Future Work

We have introduced a new non-rigid point set registration method and its applications in the studies of the human masticatory system. In this chapter, we summarize the proposed non-rigid point set registration methods and its applications to the human masticatory system, highlight the technical contributions, discuss the limitations of our work and suggest directions of future work.

8.1 Conclusion

8.1.1 Non-rigid Point Set Registration

We have demonstrated in this thesis that the issues with the current methods are solved by the proposed GLMDTPS and GLMDGRBF methods. Moreover, our methods are able to deal with the registration in the presence of noise, outliers, rotation and missing points. In the experimental comparisons, our methods show the best alignments in most scenarios and outperform state-of-the-art methods.

Robustness and stability of our methods are achieved through two techniques: mixture distance feature based correspondence estimation and a novel anneal-

ing scheme. By minimizing the GLMD based cost matrix, our methods allow multi-features to be employed to estimate the correspondences during registration. Moreover, the annealing scheme combined with GLMD based cost matrix improves the correspondence estimation process compared with the other three methods as well as enhances the interaction between correspondence estimation and transformation updating. In addition, the number of closest points, K , combines greater flexibility in dealing with deformation, noise, outliers and rotation with accurate performance. The above are empirical facts confirmed by the large number of experiments demonstrated in this thesis.

8.1.2 Applications in Human Masticatory System

Firstly, we have introduced a new framework for assessing human masticatory muscle deformation, which consists of four steps: (i) muscle deformation capture, (ii) muscle model quantization, (iii) muscle deformation assessment and (iv) muscle deformation visualization. Unlike the current techniques, the proposed framework allows visualization of muscle functional activities along the entire body as well as at specific compartments through the assessment of muscle deformation. Moreover, the important biomechanical characteristic of muscle contraction direction may also be indicated by the resultant direction of the assessed deformation field.

Secondly, we sought to investigate the functional activities of masseter muscles and lateral pterygoid muscles by the proposed framework. The nature and subject-specific deformations of the masseter muscles and the lateral pterygoid muscles at various mandibular positions were assessed and visualized. These

could not be identified by current approaches. This study would help to further relate muscle deformation to muscle contraction and the metabolic activities for evaluating masticatory muscle efficiency before and after orthodontic treatment, and facilitate the diagnosis and management of masticatory muscle dysfunction.

Finally, we sought to explain the biomechanical relationship between the mandibular movement and the muscle functional activities under a maximum intercuspation case. The mandibular movement and the masticatory muscle tensions of a specific subject are assessed, and the biomechanical relationship between the mandibular movement and the muscle functional activities are clarified. This study would be very helpful to explain the biomechanics of the anatomically and functionally complex masticatory system and assist in making proper diagnosis and treatment for masticatory muscle dysfunction or temporomandibular joint disorder.

8.2 Limitations and Future Work

8.2.1 Non-rigid Point Set Registration

At first, we improved the correspondence estimation using a mixture distance feature (GLMD) and minimizing the GLMD based cost. However, the proposed methods may not be able to cope well with missing points on both the source and target point sets since we force one-to-one correspondence using a linear assignment solution even if corresponding points (in the target point set) do not exist. In addition, unlike CPD and GMMREG, our methods are currently unable to deal with rigid point set registration problems. Extending GLMDTPS

and GLMDGRBF to rigid registration problems would be desirable.

Secondly, although our methods outperform the other methods in most scenarios, the mixed local and global distances may not be the best combination and there is still plenty of scope for further improvement. Since we created a new approach "Global feature + $\alpha \times$ Local feature" that allows a multi-feature use, better feature representations on global and local can be explored.

Thirdly, the iterative methods such as our methods, TPS-RPM, CPD and GMMREG typically contain higher computational cost which limit the applicability on the large dataset non-rigid registration. Therefore, using such matrix approximation or automatically optimizing the free parameter setting for reducing the computational time may be considered as a part of future work.

Finally, we list the three directions of future work and possible approaches:

- Multi-feature based correspondence estimation
 - Global distance + $\alpha \times$ Shape Context
 - Global distance + $\alpha \times$ Graph Relation
 - Global distance + $\alpha \times$ Shape Histogram
 - Global distance + $\alpha \times$ Curve Feature
- Development of a method for large dataset registration
 - Low-rank matrix approximation
 - Fast Gauss transform
 - Optimizing the annealing parameters (T_{init} , T_{final} and r) and the number of closest points K

-
- Rigid point set registration
 - Changing non-rigid transformation to rigid transformation

8.2.2 Applications in Human Masticatory System

Firstly, although we investigated the muscle functional activities and explained the biomechanical relationship between the muscles and the mandible using the proposed framework, there are some limitations which could be the subject of future work.

- i. The four stepwise mandibular positions were used to simulate successive jaw opening and closing movements. Future work may apply a real time MR imaging technique, which has been already used experimentally [103], for capturing the internal structures of masticatory muscles under real successive mandibular movements.
- ii. The proposed framework is a first-cut approximation approach, and not a real muscle modelling approach since the deformation of muscle layers (or fibers) was modeled by the TPS transformation which is a physically-based model for modelling the stretching and bending of thin metal sheet.
- iii. The cumulative errors due to the muscle segmentation, quantization and registration should be reduced in future work. One possible approach is to first improve the segmentation technique, and then only sampling the source muscle model into discrete points and map the source points to the point sets of the whole muscle. This is equivalent to having a target set with infinite

resolution, which removes quantization error of the target set, thus improving the registration accuracy.

- iv. The PFI [97] (Priority for Force Index) values used in section 7.3.4 for expressing the elastic characteristics of human masticatory muscles are statistical values, not for specific subjects.

Secondly, the muscle deformations under side-to-side mandibular movements as well as chewing are still unknown, and the biomechanical relationship in jaw opening as well as that between condyle movements and lateral pterygoid muscles may also be investigated in the same way since the condyle movements can be assessed from MR images using our proposed MRI protocol.

Thirdly, the validation method (in section 6.1.3 and 6.2.3) for the muscle model registration could be improved by adding additional criteria for assessing neighboring cross mismatches and long geodesic distance mismatches [13] as well as motion coherence in muscle layers. In addition, only using a single method is difficult to provide an optimal result since no method can be guaranteed to give the best results in any case. Therefore a multi-method based deformation assessment approach is essential for individual diagnosis.

Finally, we list the discussed future work:

- Investigating the deformations of medial pterygoid muscle and temporal muscle
- Investigating the muscle deformations under lateral mandibular movements
- Investigating the muscle deformations under chewing

-
- Biomechanical relationship between masticatory muscle functional activity and jaw opening
 - Biomechanical relationship between condyle movement and lateral pterygoid muscle functional activity
 - Improving validation method of muscle deformation assessment
 - Multi-method based muscle deformation assessment

Appendix A: Useful Tools

.1 GLMD Demo Package

We provide a Matlab demo package free for academic research. You may see many matching examples in 2D and 3D, and check the performance of our methods by this demo application where the deformation, noise, outlier and rotation are fully randomly set at each program launch. This demo can also be considered as a good evidence and supporting material for discussing our works. If you need this demo application, please email me by y.yang.tony@gmail.com.

.2 3D Thin Plate Spline Transformation

```
%=====
% 3D Thin Plate Spline Warping Function :
%=====
% Copyright (C) 2012 Yang Yang,
%
% Contact Information: y.yang.tony@gmail.com
%
% [wobject] = TPS3D(points , ctrlpoints , object)
%
% Input :
% points: the old positions of control points
```

```

% ctrlpoints: the new positions of control points
% object: the source template
%
% Output:
% wobject: the warped source template
%=====
function [wobject] = TPS3D(points , ctrlpoints ,object)

    npnts = size(points ,1);
    K = zeros(npnts , npnts);
    % Calculate r
    for rr = 1:npnts
        for cc = 1:npnts
            K(rr ,cc) = sum((points(rr ,:) - points(cc ,:)).^2);
            K(cc ,rr) = K(rr ,cc);
        end;
    end;
    % Calculate kernel matrix
    K = max(K,1e-320);
    %K = K.* log(sqrt(K)); % For 2D
    K = sqrt(K); % For 3D

    % Calculate P matrix
    P = [ones(npnts,1) , points];

    % Calculate L matrix
    L = [[K,P];[P', zeros(4,4)]];
    param = pinv(L)*[ctrlpoints; zeros(4,3)];

    % Calculate new coordinates
    pntsNum=size(object ,1);
    K = zeros(pntsNum, npnts);
    gx=object(:,1);
    gy=object(:,2);
    gz=object(:,3);
    for nn = 1:npnts
        K(:,nn) = (gx-points(nn,1)).^2
                + (gy-points(nn,2)).^2
                + (gz-points(nn,3)).^2;
    end;

```



```
K = max(K, 1e-320);
K = sqrt(K);

P = [ones(pntsNum, 1), gx, gy, gz];
L = [K, P];
wobject = L * param;
wobject(:, 1) = round(wobject(:, 1) * 10^3) * 10^-3;
wobject(:, 2) = round(wobject(:, 2) * 10^3) * 10^-3;
wobject(:, 3) = round(wobject(:, 3) * 10^3) * 10^-3;

end
```

.3 Jonker-Volgenant Algorithm Matlab Code

The Jonker-Volgenant algorithm is much faster than the famous Hungarian algorithm for the Linear Assignment Problem (LAP). This Matlab implementation is modified from the original C++ code made by Roy Jonker, one of the inventors of the algorithm. It can solve a 1000 x 1000 problem in about 3 seconds in a normal Intel Centrino processor. Click [here](#) to download Matlab source code, or refer to the link: <http://www.mathworks.com/matlabcentral/fileexchange/26836-lapjv-jonker-volgenant-algorithm-for-linear-assignment-problem-v2-5>

.4 ITK-SNAP

ITK-SNAP is a very useful software used to semi-automatically segment anatomical structures in 3D medical images. Click [here](#) to download ITK-SNAP software, or refer to the link: <http://www.itksnap.org/pmwiki/pmwiki.php> for official website.

.5 Osirix

Osirix is a free software used to measure anatomical structures such as measuring volume, length and cross-sectional area. Click [here](#) to download Osirix software, or refer to the link: <http://www.osirix-viewer.com/> for official website.

.6 iso2mesh

iso2mesh is a free matlab/octave-based mesh generation and processing toolbox. It may facilitate the coding on medical image visualization and further processing on mesh as well as point cloud. Click [here](#) to download iso2mesh package, or refer to the link: <http://iso2mesh.sourceforge.net/cgi-bin/index.cgi> for official website.

References

- [1] B. Liebgott, *The Anatomical Basis of Dentistry*. MOSBY ELSEVIER, 2011. [xiii](#), [63](#)
- [2] S. Park and K. Lee, “A line feature matching technique based on an eigenvector approach,” *Computer Vision and Image Understanding*, vol. 77, pp. 263–283, 2000. [3](#)
- [3] W. Kong and B. Kimia, “On solving 2d and 3d puzzles using curve matching,” *Proc. IEEE CS Conf. Computer Vision and Pattern Recognition*, vol. 2, pp. 583–590, 2001. [3](#)
- [4] S. Cochran and G. Medioni, “3d surface description from binocular stereo,” *IEEE Transactions on Pattern Analysis and Machine Intelligence*, vol. 14, pp. 981–994, 1992. [3](#)
- [5] S. Belongie, J. Malik, and J. Puzicha, “Shape matching and object recognition using shape contexts,” *IEEE Transactions on Pattern Analysis and Machine Intelligence*, vol. 24, pp. 509–521, 2002. [3](#), [78](#)
- [6] M. Kortgen, G. Park, M. Novotni, and R. Klein, “3d shape matching with

- shape context,” *Proc. The 7th Central European Seminar on Computer Graphics*, pp. 22–24, 2003. [3](#)
- [7] V. Balakrishnan, *Graph Theory 1st ed.* McGraw-Hill, 1997. [3](#)
- [8] H. Sundar, D. Silver, N. Gagvani, and S. Dickinson, “Skeleton based shape matching and retrieval,” *Proc. the Shape Modeling International(SMI’03)*, pp. 130–139, 2003. [3](#)
- [9] Y. Zheng and D. Doermann, “Robust point matching for nonrigid shapes by preserving local neighborhood structures,” *IEEE Transactions on Pattern Analysis and Machine Intelligence*, vol. 28, pp. 643–649, 2006. [3](#)
- [10] T. Caetano, L. Cheng, Q. Le, and A. Smola, “Learning graph matching,” *IEEE 11th International Conference on Computer Vision*, pp. 1–8, 2007. [3](#), [23](#), [41](#)
- [11] F. Zhou and F. De la Torre, “Factorized graph matching,” *IEEE Conference on Computer Vision and Pattern Recognition*, pp. 127–134, 2012. [3](#), [22](#), [41](#)
- [12] M. Leordeanu, R. Sukthankar, and M. Hebert, “Unsupervised learning for graph matching,” *International Journal of Computer Vision*, vol. 96, pp. 28–45, 2012. [3](#), [23](#), [41](#)
- [13] D. Xiao, D. Zahra, P. Bourgeat, P. Berghofer, O. Tamayo, C. Wimberley, M. Gregoire, and O. Salvado, “An improved 3d shape context based non-rigid registration method and its application to small animal skeletons registration,” *Computerized Medical Imaging and Graphics*, vol. 34, pp. 321–332, 2009. [3](#), [78](#), [85](#), [118](#)

-
- [14] B. Jian and B. Vemuri, “Robust point set registration using gaussian mixture models,” *IEEE Transactions on Pattern Analysis and Machine Intelligence*, vol. 33, pp. 1633–1645, 2011. [3](#), [4](#), [22](#), [27](#), [47](#), [52](#), [78](#)
- [15] P. Besl and N. McKay, “A method for registration of 3d shapes,” *IEEE Transactions on Pattern Analysis and Machine Intelligence*, vol. 14, pp. 239–256, 1992. [4](#)
- [16] H. Chui and A. Rangarajan, “A new algorithm for non-rigid point matching,” *Computer Vision and Image Understanding*, vol. 89, pp. 114–141, 2003. [4](#), [6](#), [22](#), [24](#), [25](#), [27](#), [32](#), [47](#), [52](#), [59](#), [78](#)
- [17] A. Rangarajan, H. Chui, and F. Bookstein, “The softassign procrustes matching algorithm,” in *Information Processing in Medical Imaging (IPMI’97)*, pp. 29–42, 1997. [4](#)
- [18] H. Chui, J. Rambo, R. Duncan, and A. Rangarajan, “Registration of cortical anatomical structures via robust 3dpoint matching,” in *Information Processing in Medical Imaging (IPMI’99)*, pp. 168–181, 1999. [4](#)
- [19] S. Gold, A. Rangarajan, C. Lu, S. Pappu, and E. Mjolsness, “New algorithms for 2-d and 3-d point matching: pose estimation and correspondence,” *Pattern Recognition*, vol. 31, pp. 1019–1031, 1998. [4](#), [19](#)
- [20] A. Yuille, “Generalized deformable models statistical physics and matching problems,” *Neural Computation*, vol. 2, pp. 1–24, 1990. [4](#), [19](#)
- [21] F. Bookstein, “Principal warps: thin-plate splines and the decomposition

- of deformations,” *IEEE Transactions on Pattern Analysis and Machine Intelligence*, vol. 11, pp. 567–585, 1989. 4
- [22] A. Myronenko, X. Song, and M. Carreira-Perpinan, “Non rigid point set registration: Coherent point drift,” *Advances in Neural Information Processing Systems*, pp. 1009–1016, 2006. 4
- [23] A. Yuille and N. Grzywacz, “A mathematical analysis of the motion coherence theory,” *International Journal of Computer Vision*, vol. 3, pp. 155–175, 1989. 4
- [24] A. Myronenko and X. Song, “Point set registration: Coherent point drift,” *IEEE Transactions on Pattern Analysis and Machine Intelligence*, vol. 32, pp. 2262–2275, 2010. 4, 22, 24, 25, 27, 35, 47, 52, 56, 78
- [25] L. Greengard and J. Strain, “The fast gauss transform,” *Journal of Scientific and Statistical Computing*, vol. 12, pp. 79–94, 1991. 4
- [26] I. Markovsky, “Structured low-rank approximation and its applications,” *Automatica*, vol. 44, pp. 891–909, 2008. 4
- [27] L. Ruschendorf and S. Rachev, “A characterization of random variables with minimum l_2 distance,” *Journal of Multivariate Analysis*, vol. 32, pp. 48–54, 1990. 4
- [28] O. Acosta, J. Fripp, V. Dore, P. Bourgeat, J. Favreau, G. Chetelat, A. Rueda, V. Villemagne, C. Szoek, D. Ames, K. Ellis, R. Martins, C. Masters, C. Rowe, E. Bonner, F. Gris, D. Xiao, P. Raniga, V. Barra, and O. Salvado, “Cortical surface mapping using topology correction, partial flatten-

- ing and 3d shape context-based non-rigid registration for use in quantifying atrophy in alzheimer’s disease,” *Journal of Neuroscience Methods*, vol. 205, pp. 96–109, 2012. [6](#), [36](#), [78](#), [85](#)
- [29] M. Lorenzo Valdes, G. Sanchez Ortiz, R. Mohiaddin, and D. Rueckert, “Atlas-based segmentation and tracking of 3d cardiac mr images using non-rigid registration,” *Proceedings of the 5th International Conference on Medical Image Computing and Computer-Assisted Intervention-Part I*, pp. 642–650, 2002. [6](#)
- [30] M. Ledesma Carbayo, J. Kybic, M. Desco, A. Santos, M. Suhling, P. Hunziker, and M. Unser, “Spatio-temporal nonrigid registration for ultrasound cardiac motion estimation,” *IEEE Transactions on Medical Imaging*, vol. 24, pp. 1113–1126, 2005. [6](#)
- [31] D. Liao, J. Zhao, and H. Gregersen, “A novel 3d shape context method based strain analysis on a rat stomach model,” *Journal of Biomechanics*, vol. 45, pp. 1566–1573, 2012. [6](#), [36](#), [78](#)
- [32] M. Urschler and H. Bischof, “Assessing breathing motion by shape matching of lung and diaphragm surfaces,” in *Proc.SPIE Conf on Medical Imaging: Physiology and Function from Multidimensional Images*, vol. 5746, pp. 440–452, 2005. [6](#), [36](#), [78](#), [85](#)
- [33] F. Al Osaimi, M. Bennamoun, and A. Mian, “An expression deformation approach to non-rigid 3d face recognition,” *Journal International Journal of Computer Vision*, vol. 81, pp. 302–316, 2009. [6](#)

- [34] R. Jonker and A. Volgenant, “A shortest augmenting path algorithm for dense and sparse linear assignment problems,” *Computing*, vol. 38, pp. 325–340, 1987. [15](#), [46](#)
- [35] M. Miller, H. Stone, and I. Cox, “Optimizing murty’s ranked assignment method,” *IEEE Transactions on Aerospace and Electronic Systems*, vol. 33, pp. 851–862, 1997. [15](#)
- [36] G. Wahba, *Spline Models for Observational Data*. SIAM, Philadelphia, 1990. [17](#), [59](#)
- [37] TPS-RPM, “This is the URL of TPS-RPM source codes,” 2003. [27](#)
- [38] CPD, “This is the URL of CPD source codes,” 2010. [27](#)
- [39] GMMREG, “This is the URL of GMMREG source codes,” 2011. [27](#)
- [40] Y. Yang, K. Foong, S. Ong, M. Yagi, and K. Takada, “A new methodology for studying the functional activity of lateral pterygoid muscle,” in *62nd American Academy of Oral and Maxillofacial Radiology Annual Meeting*, p. 67, 2011. [36](#)
- [41] Y. Yang, K. Foong, S. Ong, M. Yagi, and K. Takada, “An image-based method for quantification of masseter muscle deformation,” in *The 5th International Conference on Biomedical Engineering and Informatics*, pp. 148–152, 2012. [36](#)
- [42] Y. Yang, K. Foong, S. Ong, M. Yagi, and K. Takada, “Image-based estimation of biomechanical relationship between masticatory muscle activities

- and mandibular movement,” in *The IEEE 12th International Conference on Bioinformatics and Bioengineering*, pp. 683–688, 2012. 36
- [43] Y. Yang, K. Foong, S. Ong, M. Yagi, and K. Takada, “An image-based method for quantification of lateral pterygoid muscle deformation,” in *The IEEE 12th International Conference on Bioinformatics and Bioengineering*, pp. 698–702, 2012. 36
- [44] D. Xiao, D. Zahra, P. Bourgeat, P. Berghofer, A. Tamayo, C. Wimberley, M. Gregoire, and O. Salvado, “An improved 3d shape context based non-rigid registration method and its application to small animal skeletons registration,” *Computerized Medical Imaging and Graphics*, vol. 34, pp. 321–332, 2009. 36
- [45] P. Mahalanobis, “On the generalised distance in statistics,” *Proc Indian Natl Sci Acad Phys Sci*, vol. 2, pp. 49–55, 2012. 55, 58
- [46] J. Cruveilhier, *Trait d’Anatomie Descriptive*. Paris, Lab, 1851. 64
- [47] G. Schumacher, *Funcktionnelle Morphologie der Kaumuskulatur*. G. Fischer, 1961. 64, 82, 88
- [48] P. Eisler, *Die Muskeln des Stammes. In Handbuch des Anatomie des Menschen (ed. von Bardeleben K)*. Gustav Fischer, 1912. 64
- [49] P. Williams, L. Bannister, M. Berry, P. Collins, M. Dyson, J. Dussek, and M. Ferguson, *DGray’s Anatomy (38th edn)*. Churchill Livingstone, 1995. 64

REFERENCES

- [50] S. Terada and T. Sato, “Nerve supply of the medial and lateral pterygoid muscles and its morphological significance,” *OkajimasFolia Anatomica Japonica*, vol. 59, pp. 251–264, 1982. [65](#)
- [51] S. Tomo, “Morphological classification of the masticatory muscles based on their innervation,” *Ochanomizu Medical Journal*, vol. 38, pp. 57–71, 1990. [65](#)
- [52] T. Yoshikawa and T. Suzuki, “The lamination of the human masseter. the new identification of m. temporalis superficialis, m. maxillomandibularis and m. zygomaticomandibularis in human anatomy,” *Acta Anatomica Nipponica*, vol. 37, pp. 260–267, 1962. [65](#)
- [53] J. Merida Velasco, J. Rodriguez Vasquez, and J. Collad Jimenez, “The relationships between the temporomandibular joint disc and related masticatory muscles in humans,” *Journal of Oral and Maxillofacial Surgery*, vol. 51, pp. 390–395, 1993. [65](#)
- [54] Wikipedia, “Muscle of mastication.” http://en.wikipedia.org/wiki/Muscles_of_mastication. [65](#)
- [55] J. Foucart, J. Girin, and P. Carpentier, “Innervation of the human lateral pterygoid muscle,” *Surgical and Radiologic Anatomy*, vol. 20, pp. 185–189, 1998. [65](#)
- [56] C. Schmolke, “The relationships between the temporomandibular joint capsule, articular disk and jaw muscles,” *Journal of Anatomy*, vol. 184, pp. 335–345, 1994. [65](#)

REFERENCES

- [57] K. Matsunaga, A. Usui, K. Yamaguchi, and K. Akita, “An anatomical study of the muscles that attach to the articular disc of the temporomandibular joint,” *Clinical Anatomy*, vol. 22, pp. 932–940, 2009. [65](#)
- [58] K. Akita, T. Shimokawa, and T. Sato, “Positional relationships between the masticatory muscles and their innervating nerves with special reference to the lateral pterygoid and the midmedial and discotemporal muscle bundles of temporalis,” *Journal of Anatomy*, vol. 197, pp. 291–302, 2000. [65](#)
- [59] J. MacDonald and A. Hannam, “Relationship between occlusal contacts and jaw-closing muscle activity during tooth clenching: Part i,” *Journal of Prosthetic Dentistry*, vol. 52, pp. 718–728, 1984. [66](#), [82](#), [103](#)
- [60] N. Blanksma and T. van Eijden, “Electromyographic heterogeneity in the human temporalis and masseter muscles during static biting, open/close excursions, and chewing,” *Journal of Dental Research*, vol. 74, pp. 1318–1327, 1995. [66](#), [82](#)
- [61] C. Gibbs, P. Mahan, T. Wilkinson, and A. Mauderli, “Emg activity of the superior belly of the lateral pterygoid muscle in relation to other jaw muscles,” *Journal of Prosthetic Dentistry*, vol. 51, pp. 691–702, 1984. [66](#), [94](#)
- [62] W. Wood, K. Takada, and A. Hannam, “The electromyographic activity of the inferior part of the human lateral pterygoid muscle during clenching and chewing,” *Archives of Oral Biology*, vol. 31, pp. 245–253, 1986. [66](#), [94](#)
- [63] A. Hannam and A. McMillan, “Internal organization in the human jaw

REFERENCES

- muscles,” *Critical Reviews in Oral Biology and Medicine*, vol. 5, pp. 55–89, 1994. [66](#), [94](#)
- [64] S. Ruangsri, T. Whittle, K. Wanigaratne, and G. Murray, “Functional activity of superior head of human lateral pterygoid muscle during isometric force,” *Journal of Dental Research*, vol. 84, pp. 548–553, 2005. [66](#), [94](#)
- [65] J. Ahlgren, “Emg pattern of temporalis in normal occlusion,” *European Journal of Orthodontics*, vol. 8, pp. 185–191, 1986. [66](#)
- [66] T. Goto, G. Langenbach, and A. Hannam, “Length changes in the human masseter muscle after jaw movement,” *The Anatomical Record*, vol. 262, pp. 293–300, 2001. [67](#), [70](#), [71](#), [82](#)
- [67] T. Goto, M. Yahagi, Y. Nakamura, K. Tokumori, G. Langenbach, and K. Yoshiura, “In vivo cross-sectional area of human jaw muscles varies with section location and jaw position,” *Journal of Dental Research*, vol. 84, pp. 570–576, 2005. [67](#), [70](#), [71](#), [82](#), [94](#)
- [68] T. Goto, K. Tokumori, Y. Nakamura, M. Yahagi, K. Yuasa, K. Okamura, and S. Kanda, “Volume changes in human masticatory muscles between jaw closing and opening,” *Journal of Dental Research*, vol. 81, pp. 428–432, 2002. [67](#), [70](#), [71](#), [82](#), [94](#)
- [69] K. Kubo, T. Kawata, T. Ogawa, M. Watanabe, and K. Sasaki, “Outer shape changes of human masseter with contraction by ultrasound morphometry,” *Archives of Oral Biology*, vol. 51, pp. 146–153, 2006. [67](#), [71](#), [82](#)

REFERENCES

- [70] O. Hidaka, M. Yanagi, and K. Takada, “Changes in masseteric hemodynamics time-related to mental stress,” *Journal of Dental Research*, vol. 83, pp. 185–190, 2004. [67](#), [83](#)
- [71] N. Abe, K. Yashiro, O. Hidaka, and K. Takada, “Influence of gum-chewing on the hemodynamics in female masseter muscle,” *Journal of Oral Rehabilitation*, vol. 36, pp. 240–249, 1986. [67](#), [83](#)
- [72] C. Peck, G. Murray, C. Johnson, and I. Klineberg, “The variability of condylar point pathways in open-close jaw movements,” *Journal of Prosthetic Dentistry*, vol. 77, pp. 394–404, 1996. [68](#)
- [73] I. Stavness, A. Hannam, J. Lloyd, and S. Fels, “An integrated dynamic jaw and laryngeal model constructed from ct data,” *Proceedings of ISBMS 06*, pp. 169–177, 2006. [68](#)
- [74] F. Zhang, C. Peck, and A. Hannam, “Mass properties of the human mandible,” *Journal of Biomechanics*, vol. 35. [68](#)
- [75] A. Hill, “Mechanics of active muscle,” *Proceedings of the Royal Society of London*, vol. 141. [69](#)
- [76] C. Peck, G. Langenbach, and A. Hannam, “Dynamic simulation of muscle and articular properties during wide jaw opening,” *Archives of Oral Biology*, vol. 45. [69](#)
- [77] A. van den Bogert, K. Gerritsen, and G. Cole, “Human muscle modelling from a user’s perspective,” *Journal of Electromyography and Kinesiology*, vol. 8. [70](#)

-
- [78] Wikipedia, “Muscle.” <http://en.wikipedia.org/wiki/Muscle>. 70
- [79] S. Lloyd, “Least squares quantization in pcm,” *IEEE Transactions on Information Theory*, vol. 28, pp. 129–137, 1982. 75
- [80] E. Lam, A. Hannam, and E. Christiansen, “Estimation of tendonplane orientation within human masseter muscle from reconstructed magnetic resonance images,” *Archives of Oral Biology*, vol. 36, pp. 845–853, 1991. 82
- [81] J. Gaudy, A. Zouaoui, P. Bravetti, J. Charrier, and A. Guettaf, “Functional organization of the human masseter muscle,” *Surgical and Radiologic Anatomy*, vol. 22, pp. 181–190, 2000. 82, 88
- [82] D. Maret, F. Molinier, J. Braga, O. Peters, N. Telmon, J. Treil, J. Inglese, A. Cossie, J. Kahn, and M. Sixou, “Accuracy of 3d reconstructions based on cone beam computed tomography,” *Journal of Dental Research*, vol. 89, pp. 1465–1470, 2010. 83, 104
- [83] I. Reinertsen, M. Descoteaux, K. Siddiqi, and D. Collins, “Clinical validation of vessel-based registration for correction of brain shift,” *Medical Image Analysis*, vol. 11, pp. 673–684, 2007. 85
- [84] J. Schnabel, C. Tanner, A. Castellano-Smith, A. Degenhard, M. Leach, D. Hose, D. Hill, and D. Hawkes, “Validation of nonrigid image registration using finite-element methods: application to breast mr images,” *IEEE Transactions on Medical Imaging*, vol. 22, pp. 238–247, 2003. 85
- [85] I. Reinertsen, M. Descoteaux, K. Siddiqi, and D. Collins, “Validation of

- vessel-based registration for correction of brain shift,” *Medical Image Analysis*, vol. 11, pp. 374–388, 2007. [85](#)
- [86] K. Babalola, B. Patenaude, P. Aljabar, J. Schnabel, D. Kennedy, W. Crum, S. Smith, T. Cootes, M. Jenkinson, and D. Rueckert, “An evaluation of four automatic methods of segmenting the subcortical structures in the brain,” *Neuroimage*, vol. 47, pp. 1435–1447, 2009. [85](#)
- [87] J. Osbom and F. Baragar, “Predicted pattern of human muscle activity during clenching derived from a computer assisted model: Symmetric vertical bite forces,” *Journal of Biomechanics*, vol. 18, pp. 599–612, 1985. [91](#)
- [88] T. van Eijden, E. Klok, W. Weijs, and J. Koolstra, “Mechanical capabilities of the human jaw muscles studied with a mathematical model,” *Archives of Oral Biology*, vol. 33, pp. 819–826, 1988. [91](#)
- [89] G. Langenbach and A. Hannam, “The role of passive muscle tensions in a three-dimensional dynamic model of the human jaw,” *Archives of Oral Biology*, vol. 44, pp. 557–573, 1999. [93](#)
- [90] C. Peck and A. Hannam, “Human jaw and muscle modeling,” *Archives of Oral Biology*, vol. 52, pp. 300–304, 2007. [93](#), [103](#)
- [91] P. Baron and T. Debussy, “A biomechanical functional analysis of the masticatory muscles in man,” *Archives of Oral Biology*, vol. 24, pp. 547–553, 1979. [93](#)
- [92] Okeson1998, *Management of temporomandibular disorders and occlusion. 4 edn.* St Louis: Mosby, 1998. [94](#)

REFERENCES

- [93] J. Lund, G. Lavigne, R. Dubner, and B. Sessle, *Orofacial pain; from basic science to clinical management*. Quintessence Publ. Co, 2001. 94
- [94] G. Murray, I. Phanachet, S. Uchida, and T. Whittle, “The human lateral pterygoid muscle: A review of some experimental aspects and possible clinical relevance,” *Australian Dental Journal*, vol. 49, pp. 2–8, 2004. 94
- [95] K. Hiraba, K. Hibino, K. Hiranuma, and T. Negoro, “Emg activities of two heads of the human lateral pterygoid muscle in relation to mandibular condyle movement and biting force,” *Journal of Neurophysiology*, vol. 83, pp. 2120–2137, 2000. 94, 100
- [96] ITKSNAP, “Itk-snap software.” <http://www.itksnap.org/pmwiki/pmwiki.php>. 104
- [97] R. Woittiez, Y. Heerkens, P. Huijing, W. Rijnsburger, and R. Rozendal, “Functional morphology of the m. gastrocnemius medialis of the rat during growth,” *Journal of Morphology*, vol. 187, pp. 247–258, 1986. 105, 118
- [98] T. van Eijden and M. Raadsheer, “Heterogeneity of fibre and sarcomere length in the human masseter muscle,” *The Anatomical Record*, vol. 232, pp. 78–84, 1992. 106
- [99] T. van Eijden, J. Koolstra, and P. Brugman, “Architecture of the human pterygoid muscles,” *Journal of Dental Research*, vol. 74, pp. 1489–1495, 1995. 106
- [100] T. van Eijden, J. Koolstra, and P. Brugman, “Three-dimensional structure

REFERENCES

- of human temporalis muscle,” *The Anatomical Record*, vol. 246, pp. 565–572, 1996. [106](#)
- [101] P. Garcia-Morales, P. Buschang, G. Throckmorton, and J. English, “Maximum bite force, muscle efficiency and mechanical advantage in children with vertical growth patterns,” *Eur J Orthod*, vol. 25, pp. 265–272, 2003. [112](#)
- [102] M. Kubota, H. Nakano, I. Sanjo, K. Sato, T. Sanjo, T. Kamegai, and F. Ishikawa, “Maxillofacial morphology and masseter muscle thickness in adults,” *Eur J Orthod*, vol. 20, pp. 535–542, 1998. [112](#)
- [103] S. Zhang, K. Block, and J. Frahm, “Magnetic resonance imaging in real time: advances using radial flash,” *Journal of Magnetic Resonance Imaging*, vol. 31, pp. 101–109, 2010. [117](#)